DESIGN AND OPTIMIZATION OF A MORPHING SLAT GAP FILLER FOR AIRCRAFT NOISE REDUCTION INCLUDING AERODYNAMIC VISUALIZATION APPROACHES

A Thesis

by

JACOB A. SCHRASS

Submitted to the Graduate and Professional School of
Texas A&M University
in partial fulfillment of the requirements for the degree of

MASTER OF SCIENCE

Chair of Committee,	Darren Hartl
Committee Members,	Moble Benedict
	Douglas Allaire
Head of Department,	Ivett Leyva

August 2022

Major Subject: Aerospace Engineering

ABSTRACT

A slat gap filler (SGF) is a structure that spans the gap between the leading edge of the wing and slat on a transportation category aircraft. This structure has potential to reduce airframe noise on approach to landing when aircraft are often flying over densely populated areas. Previous experimental aerodynamic studies showed a variety of SGF geometries can cause noise reduction. This design study expands on previous work to determine an optimal noise reducing SGF structure.

Nonlinear structural analysis of three morphing SGF design concepts explores the potential design space. The structure requires the facilitation of geometry changes between the deployed and retracted slat states, and the practical capability to stow the structure from flow for an emergency, high angle-of-attack maneuver. Because of these operational necessities, shape memory alloys (SMAs) are chosen as the SGF material. For all concepts, the structure is modeled using a superelastic SMA material exhibiting hysteretic behavior. Each concept is defined by its external or internal wing attachment location, and by its stowing method: automatic via a stress-bias or mechanical via connector actuators. The suitability of the three concepts is tested within an experimental design framework against four separate design variables per concept.

Results from the exploration are utilized to select a single SGF concept. Fluid dynamics simulations are used as inputs to an aeroacoustic formulation to determine overall noise for an SGF configuration. An efficient global optimization (EGO) strategy is implemented with the structural and aeroacoustic solvers. The structural side of the optimization considers the objectives of mass and actuation force along with structural constraints. The acoustic side of the optimization considers an objective to minimize noise. Together, these objectives are used to determine an optimal SGF configuration.

This SGF was designed to facilitate an experimental testing campaign. However, it was difficult to demonstrate the features and identify the flaws of a 3-dimensional design using conventional 2-dimensional graphic displays. A novel mixed reality toolkit was developed to visualize complex results in the experimental facility to assist in research and educational discussions.

DEDICATION

To all those who supported me through this journey, especially my family and friends.

ACKNOWLEDGMENTS

This work was done in collaboration with the Structural Acoustics Branch of the NASA Langley Research Center. Computational structural analysis was performed with a SIMULIA Abaqus research license. Computational fluid analysis was performed with a Simcenter Star-CCM+ license.

CONTRIBUTORS AND FUNDING SOURCES

Contributors

This work was supported by a thesis committee consisting of Dr. Darren Hartl and Dr. Moble Benedict of the Department of Aerospace Engineering and Dr. Douglas Allaire of the Department of Mechanical Engineering.

The wind tunnel related work cited and presented was supported by Kevin Lieb, Mitchell Mu, and Sarah Kinney. The mixed reality work was enabled by the work of Jesse Cate and James Dean.

All other work conducted for the thesis was completed by the student independently.

Funding Sources

Graduate study was supported by a fellowship from Texas A&M University funded by the Structural Aeroacoustics Branch of the NASA Langley Research center under sponser award number C16-2B00-TAMU / 201074-TAMU.

NOMENCLATURE

SMA	Shape Memory Alloy
SPL	Sound Pressure Level
OASPL	Overall Sound Pressure Level
SGF	Slat Gap Filler
SCF	Slat Cove Filler
FEA	Finite Element Analysis
CFD	Computational Fluid Dynamics
CAA	Computational Aeroacoustics
VR	Virtual Reality
AR	Augmented Reality
MR	Mixed Reality

TABLE OF CONTENTS

Page

LIST OF FIGURES

FIGURE Page

LIST OF TABLES

TABLE Page

1. Introduction and Literature Review

1.1 The Need for Airframe Noise Reduction

As air traffic volumes increase and restrictions on maximum noise are updated , reducing noise generated by aircraft continues to be a goal of modern aerospace research. Takeoff and landing are especially important phases of flight for urban development as low flying, noisy aircraft disrupt residential areas and impact health [1]. During these flight conditions, aircraft deploy high lift devices such as slats and flaps, which expose gaps, cavities, and edges that affect the flow field on a wing. Noise generated by aerodynamic effects like these is defined as airframe noise. Engine noise, the other main source of aircraft noise, has been a major focus of work in reducing aircraft noise [2]. Since noise is interpreted on a decibel scale, it is necessary to simultaneously reduce noise coming from all sources to significantly change aggregated noise. A reduction in airframe noise is required in combination with engine noise reductions to reduce overall noise below current levels.

A representative final approach path for a transportation category aircraft with the main noise generating devices highlighted is shown in Fig. 1.1. In the figure, the engine turbines are red, the trailing edge flaps are orange, the landing gear are green, and the leading edge slats are blue. As the aircraft transitions from a low-drag cruise flight condition (1) into descent towards an airport (2), the high lift devices (the flaps, orange, and the slats, blue) are deployed to a first level, increasing drag, lift, and airframe noise. Simultaneously, the engine power and associated noise is reduced, resulting in overall noise coming from the high lift devices becoming the largest contributor to noise. Once the aircraft nears the runway (3), the high lift devices are deployed fully to a second level and the landing gear are deployed, both of which further increase the noise of the aircraft as it is flying at relatively low altitudes. Finally, the aircraft touches down on the runway (4), at which point the engines are often used to provide noisy reverse thrust, but the aircraft is now in an airport and further away from populated communities.

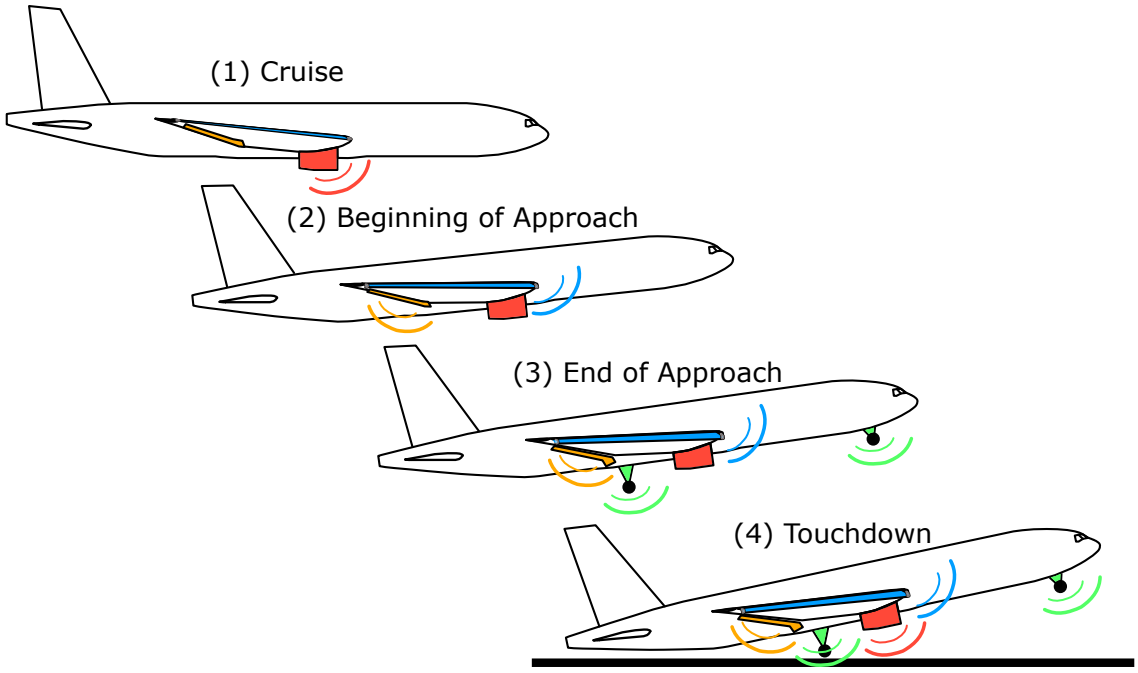

Figure 1.1: Depiction of final approach starting with the aircraft in the cruise configuration (1), beginning final approach (2), nearing the runway (3), and landing (4).

1.2 Aerostructures for Leading Edge Airframe Noise Reduction

Strategies for reducing airframe noise are the focus of this work, and scope is limited specifically to reducing noise generated by the gap between the wing leading edge and slat. A large component of airframe noise is generated by the interaction between recirculating flow behind the deployed slat and a shear layer formed at the edge of this recirculation. Noise generated by flow around the leading edge slat is of particular importance on approach to landing, when other noise generating flows, such as engines and landing gear, are not as influential. The recirculating flow field between the leading edge of the main wing surface and the under-side of the deployed slat is shown in Fig. 1.2. The shear layer bounding this recirculating flow is shed off the bottom trailing edge of the slat, curves around the recirculation, and flows through the gap between the slat and main wing. Preventing either one of these two flows with structural modifications has the potential to also inhibit the formation of the other flow, resulting in a large noise reduction.

Historically, several devices have been proposed and examined to modify flow in the region

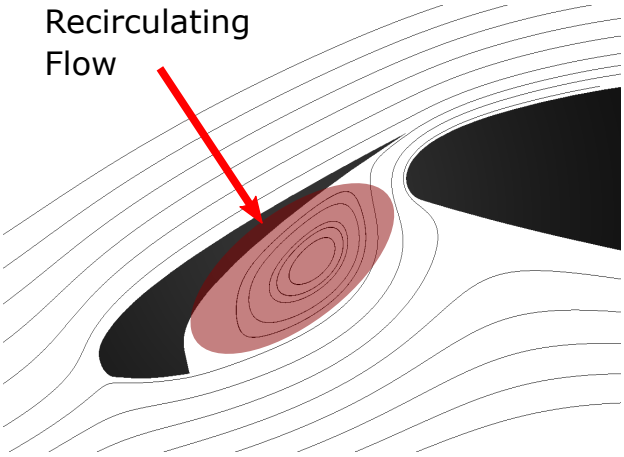

Figure 1.2: Recirculation vortices between the slat and the leading edge of the main wing surface.

behind the under-side of the slat. Khorrami and Lockard investigated utilizing bulb or blade seals to modify flow behind the slat. These authors found that a blade seal causes the shear boundary layer coming off of the bottom edge of the slat to unify, reducing the speed of the recirculating flow above this layer [3]. Flexible brushes, as proposed by [4], were designed and positioned to reduce the size of flow recirculation behind the slat such that it no longer interfered with the high speed flow through the slat gap. A slat cove filler (SCF), a flexible structure that blocks the area of recirculating flow behind the slat, was first proposed by [5] and studied by several others. The SCF profile was designed to matches the shape of the recirculation-bounding shear layer to minimally disturb wing-scale aerodynamic effects.

A morphing slat cove filler implementation using SMAs was investigated in this group at Texas A&M, first in simulations by [6] and later experimentally by [7] and [8]. These investigations of an SCF provided an extensive written framework for aerodynamic, structural, and acoustic studies of a morphing leading edge structure. These studies were modified and expanded.

1.3 A Morphing Slat Gap Filler

The proposed method to reduce airframe noise utilizes a slat gap filler (SGF), a device that closes the channel between the deployed slat and the leading edge of the main wing [9]. A simple representation of an example SGF concept is shown in Fig. 1.3. In general, a SGF is attached to the

main wing at a point on the upper surface near the leading edge. A SGF is a morphing structure that deploys and retracts in conjunction with deployment or retraction of high lift devices, as is shown in Fig. 1.4. When it is deployed, the SGF extends out to contact the bottom surface of the slat such that no there is no airflow through the gap between the deployed slat and the main wing. Closing this gap has the effect of stagnating the flow behind the slat and inhibiting the formation of noise generating recirculation vortices. In this work, SGF assembly and deployment followed by retraction is termed the deploy-retract cycle.

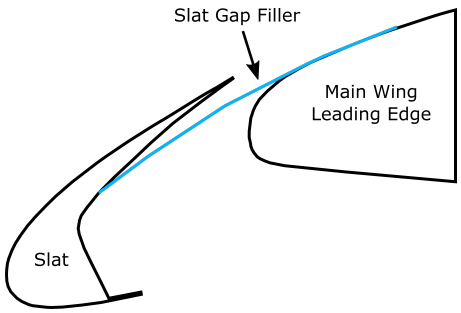

Figure 1.3: Graphical slat gap filler design example.

Compared to previously studied concepts to modify flow behind the slat, SGFs have multiple advantages. First, while all mentioned concepts attempt to modify flow through the slat gap, a SGF completely prevents this flow, which results in greater noise reduction. Additionally, the simplicity inherent in closing off the gap generally results in a structure requiring less material than other solutions. Reducing structural material minimizes the weight added to existing structures and can also reduce the additional slat actuator force required to deploy and retract an additional structure. Furthermore, similar to other noise reduction methods, a SGF does not require substantial modification to existing aircraft structures (e.g., slat actuators, wing leading edge surfaces, or internal wing structure).

However, there are some problems presented by a SGF implementation. The primary purpose of the gap between the deployed slat and main wing is to keep flow attached to the upper surface of

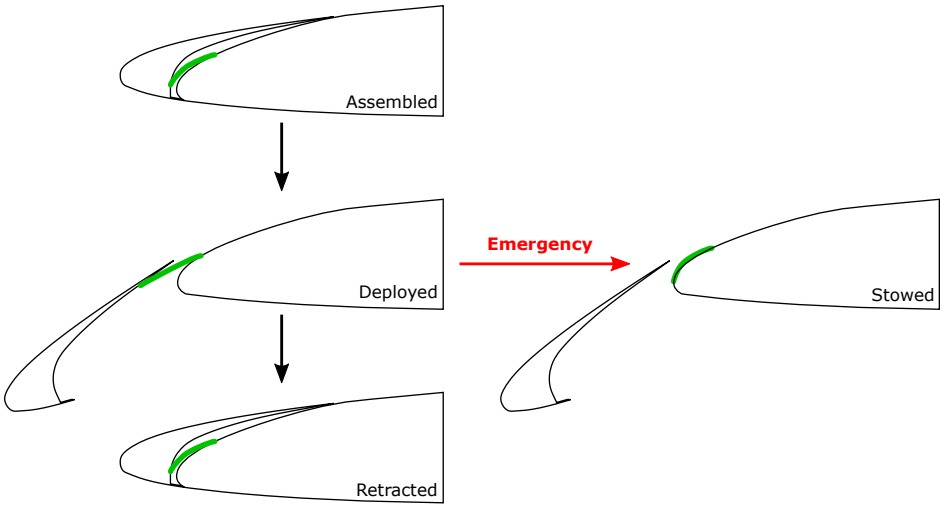

Figure 1.4: Stages of a landing cycle for a slat and main wing modified with a slat gap filler. The process begins in the assembled stage, representing a wing in the cruise condition. Following this is the deployed stage, usually occurring during approach to landing when the slat is fully deployed. Finally, the slat is either retracted with the SGF to the retracted stage for storage when the aircraft is on the ground or the SGF is stowed while the slat remains deployed for an emergency maneuver in the stowed stage.

the main wing if an emergency high angle of attack maneuver is required, like an aborted landing. Therefore, a SGF must be able to be stowed directly from its deployed state without retracting the slat. This stowing would then reopen the gap on the leading edge of the wing, restoring flow to the upper surface, and enabling emergency maneuvers. The assembly, deployment, and stowing process is termed the deploy-stow cycle. Additionally, additional force from existing actuators is required to deploy this new aerodynamic structure, even though the SGF concept seeks to minimize this force. Furthermore, deploying and stowing a SGF necessitates a morphing structure that can undergo large strains repeatedly for a large number of cycles. The geometry of the retracted slat and leading edge of the wing does not leave much space for a new structure or for any supporting mechanisms required to attach and/or actuate this structure. These geometric constraints add difficulties to both commercial implementations and experimental scale design. Altogether, a SGF design must include features that mitigate these design concerns without limiting the noise reducing effect.

A variety of potential SGF geometries have been explored in attempts to meet the described

constraints, such as the designs explored experimentally by [10] and [11]. In the total design space, potential geometries include short abrupt flow stopping devices that protrude from the wing and also long geometries that attempt to create a smooth flow transition between the trailing edge of the slat and a point on the main wing. Therefore, it is not possible to identify a single SGF geometry that can be optimized; rather several SGF design concepts, each with their own geometric features must be studied to attempt to design an optimal SGF. Such preliminary study across a range of concepts is a major achievement of this thesis.

1.3.1 Morphing Aerostructures

Shape memory alloys (SMAs) have been utilized in aerospace research for more than three decades [12]. SMAs are often used as actuators [13, 14] that deform under an applied temperature, usually via electrical current, to achieve a desired aerodynamic effect. In other applications, SMAs do not function as actuators; rather they transform between martensite and austenite due to applied loads. SMAs of this type are called superelastic SMAs because of their ability to deform large amounts and remain an elastic material.

Superelastic SMAs have been used as morphing materials in a number of related applications including [6] and [8]. Superelastic SMAs were chosen as the material for this work because they provide a desirable combination of strain recovery over many transformation cycles and stability under high loads. A hysteresis loop for an example superelastic SMA in the stress-strain space is shown in Fig. 1.5.

Starting from the austenite material phase in Fig. 1.5, (1), the SMA is unloaded and at a high temperature. The SMA is loaded to σ_{Ms}, (2), as it is assembled to the slat. As the slat deploys, the SMA transforms until regions of it reach the σ_{Mf} stress level at which point they are fully transformed into the martensite material phase. The SMA can continue to deform elastically past this point to reach (3), the point at which the SGF is fully deployed and maximally loaded. To repeat the deploy-retract loop (for standard operation on an aircraft), the slat is retracted, transforming the SMA partially back into austenite (4a). Alternatively, the SMA may be released from the slat and stowed in the deploy-stow condition, unloading and transforming the material from (3) to σ_{As},

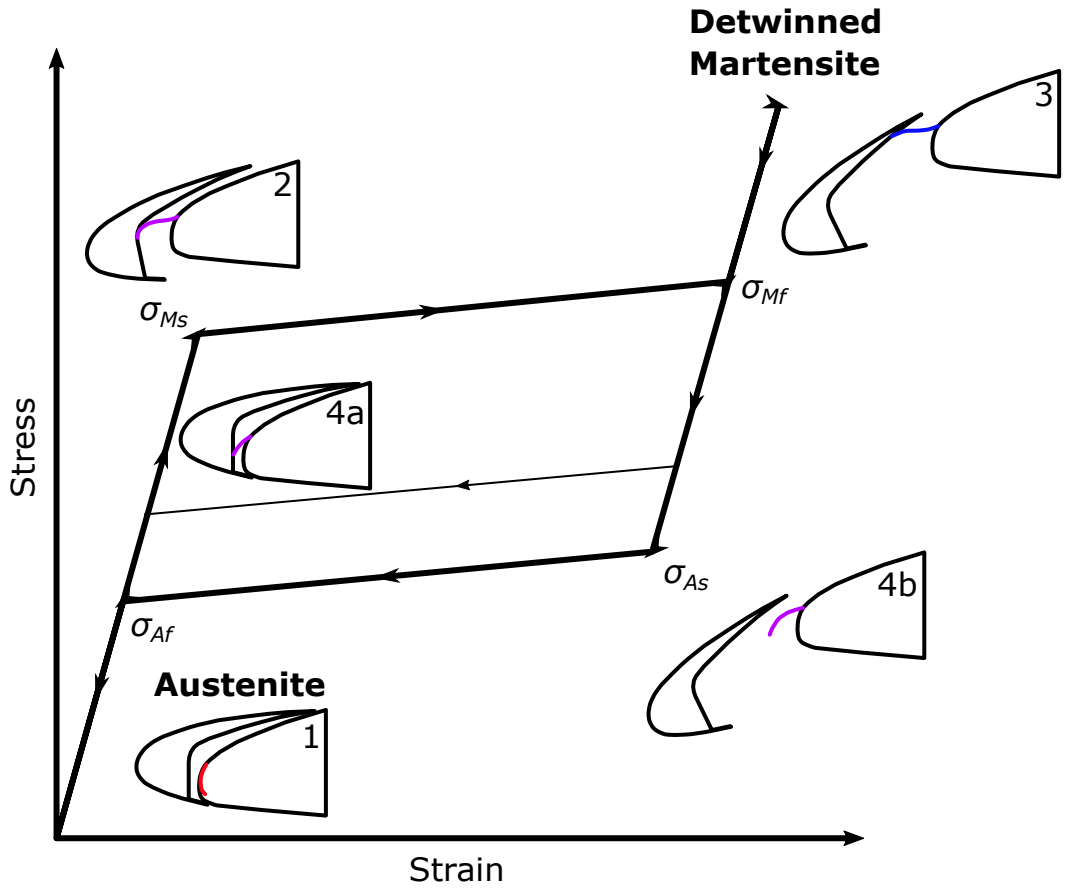

Figure 1.5: A hysteresis loop for a theoretical superelastic SMA with stages denoted by the representative point in the deploy-stow or deploy-retract cycle of a SGF.

(4b), and then to an almost completely unloaded condition, (1), at stresses below σ_{Af}.

1.4 Three Concepts

Three SGF concepts are compared to select one design for optimization. A description of each of the three concepts is presented in the following paragraphs. In Fig. 1.6, the concepts identified as A and B are both attached to the wing by fixing the wind side end of the SGF, while concept C is fixed at a position on the interior of the wing. Concept A is termed mechanism stowed because it requires actuation to move from its stress free to a stowed state flush against the wing, while concepts B and C return automatically to a position out of flow if they are released from a stressed position.

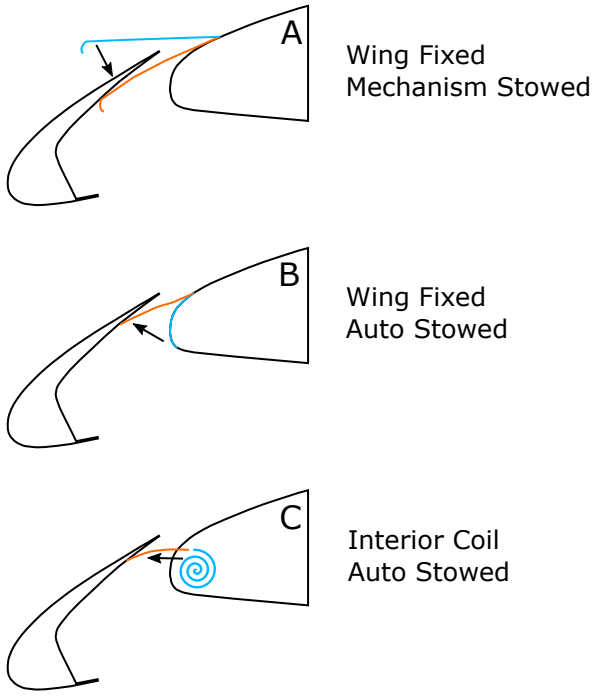

Figure 1.6: Graphical examples of the three slat gap filler concepts with the stress free configuration shown in blue and arrows indicating the direction of movement to a stressed, deployed configuration in red.

1.4.1 Wing Fixed Mechanism Stowed Slat Gap Filler

The Wing Fixed Mechanism Stowed (WFMS) SGF design is a mostly flat structure extending from the wing to contact the deployed slat. The WFMS SGF is fixed to the surface of the wing using a cusp continuous with the wing surface and a large radius curve into the flat extended portion of the SGF. In its unstressed state, the WFMS SGF is completely flat would extend above the bottom of the slat. Therefore, stowing actuators are required and the SGF is always under stress once it is assembled with the slat and wing. The stowing actuators could be retractable wires attached to a lower point on the wing determined such that the SGF lies flat against the wing when it is stowed. Since there is assembly stress present in this design that pushes upwards on the bottom surface of the slat, the WFMS SGF only requires a curved slat-side tip to smoothly contact the underside of the slat. This design is shown in Fig. 1.6A.

1.4.2 Wing Fixed Auto Stowed Slat Gap Filler

The Wing Fixed Auto Stowed (WFAS) SGF design is structurally defined to lie against the leading edge of the wing. The curved surface of the WFAS SGF lets a wing-end region of the SGF be used for a fixed connection, similar to the wing connection method of the WFMS SGF. The WFAS SGF is stress-free in a geometry that is slightly more curved that the surface of the wing. This unstressed structure results in a shape that is under a small amount of stress once it is assembled with the wing but generally lies flat along the surface of the wing. To hold the WFAS SGF design in a deployed configuration, it is connected to the slat using a sliding rail-like connection between the slat-side tip and the bottom surface of the slat. This connection would occur once when the SGF is installed and could be released to facilitate automatic stowing of the SGF using the force from the assembly stresses. The slider connection may require a complex release mechanism to stow the SGF. This type of SGF design is shown in Fig. 1.6B.

1.4.3 Interior Coil Auto Stowed Slat Gap Filler

The Interior Coil Auto Stowed (ICAS) SGF design is a structure that can both be coiled in a small volume inside the wing and uncoiled to connect to the slat. This structure would be placed in-

side the wing near the leading edge and therefore could require significant structural modifications to the wing. The wing connection method required is a fixed support that holds the un-deployed end of the slat inside the wing. Also, a smooth slot on the surface of the wing is required to extend the SGF and assemble it with the slat. To achieve this shape, the ICAS SGF is unstressed in an Archimedean coil geometry. This type of SGF design has the benefit of allowing relatively large lengths of material to be automatically retracted from the deployed configuration and stowed out of the flow. The ICAS SGF can therefore be attached to the slat at with a fixed connection in a small port cut into the bottom of the slat. A releasing mechanism like a small clamp could be used to make this connection and facilitate SGF stowing. The ICAS SGF design category is shown in Fig. 1.6C.

1.5 Mixed Reality Result Visualization

Computational fluid dynamics results are complex and often contain 3-dimensional flow structures, especially in the regime of turbulent flow. Therefore, these results are difficult to display using 2-dimensional screens. In addition, there can be a disconnect between visualizing wind tunnel experimental results and CFD simulation results even though these two engineering tools are often used in conjunction on an aerospace project. This is especially the case for wind tunnel facilities that only provide force balance results and lack flow visualization capabilities like particle image velocimetry (PIV) or smoke injection. The disconnect between CFD and wind tunnel tools can make it difficult to understand results, especially in the frequent case that wind tunnel results do not perfectly align with simulation results. Virtual reality wind tunnel applications have been explored since at least 1992 with the goal of providing enhanced understanding of both experimental and simulated results [15].

Initial attempts at utilizing virtual reality as a tool for collaborative design and flow visualization did not have the benefit of modern technology in the form of low-cost head mounted displays (HMDs) or advanced CFD software. HMD technology has advanced exponentially, meaning that even virtual reality wind tunnel implementations published in recent years are strictly confined to being only virtual interactive visualizations [16, 17, 18, 19]. Previous attempts at incorporating

views of both flow results and physical objects have been attempted with either mobile devices ([20] and [21]) or HMD devices ([22] and [23]), but these examples did not apply this technology to the unique challenges of the wind tunnel environment which requires detailed simulation results in conjunction with flexible display options. In addition, many of these examples can generally be classified as augmented reality visualizations which do not provide the interactivity and freedom of motion that can be enabled with a modern HMD device. While the terms augmented reality (AR) and mixed reality (MR) are sometimes used interchangeably, the distinction is made herein that AR refers to virtual displays overlaid on the surrounding environment while MR refers to the combination of interactive virtual reality experiences with live video of the surrounding environment. In this work, the video component of MR displays is referred to as a video pass-through. Based on an investigation of existing wind tunnel CFD visualizations, further improvements to the field of flow visualization can be provided by incorporating mixed reality capabilities.

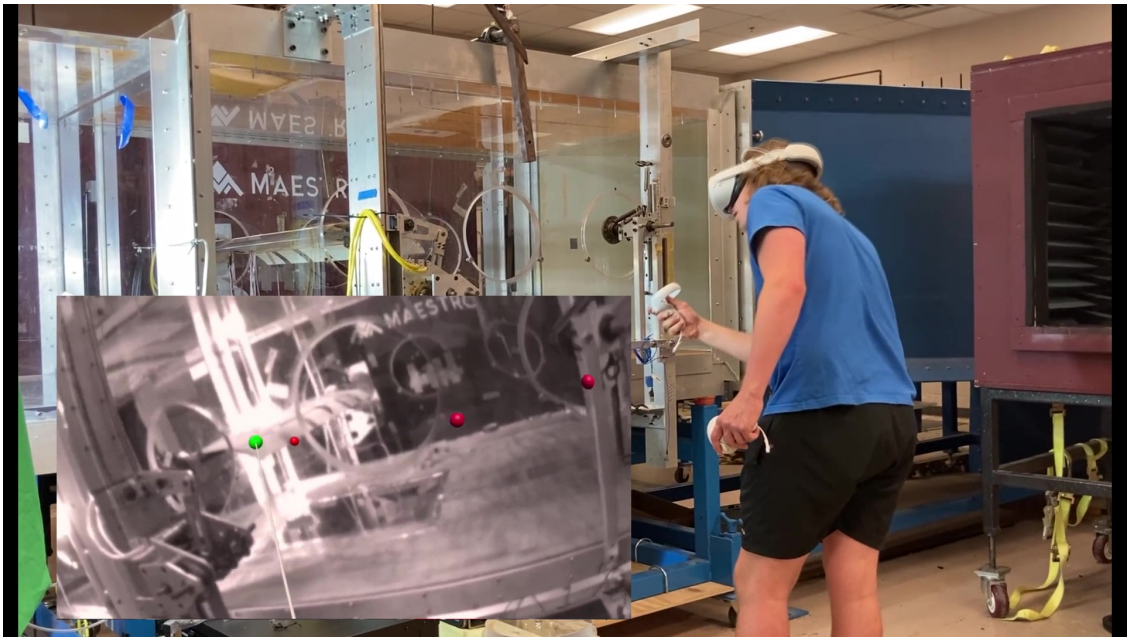

Figure 1.7: Example of a student utilizing the mixed reality toolkit to visualize flow particles while standing next to a low speed wind tunnel test section. The grayscale insert shows the view the student is seeing with the headset, with the flow particles highlighted in red.

A novel mixed reality visualization toolkit was developed to help researchers and students visualize CFD results. The toolkit was created such that 2-dimensional planar results, 3-dimensional streamline results, and elementwise flow data results could each be converted to virtual reality objects and displayed in mixed reality. Flow data results exported at each element provided the capability to generate imaginary particle objects that follow flow through the domain, similar to smoke or particle image velocimetry visualizations in wind tunnels. These virtual reality objects were defined such that they could be viewed on top of video pass-through of physical surroundings. Logic was implemented such that the virtual objects can be oriented and scaled such that they align with a physical wind tunnel section. This toolkit was created to be general in that any CFD results could be used to generate the virtual objects applied to any physical wind tunnel. An example of a student using the mixed reality toolkit is shown in Fig. 1.7.

1.6 Research Objectives

The goal of this design process was to find structural design trends that characterize an optimal SGF which minimizes airframe noise. The SGF was optimized to have minimal mass, required deployment force, and overall noise while meeting constraints on maximum deformation under aerodynamic loads. A detailed software study consisting of multiple potential SGF concepts and geometric variations within each concept was executed to achieve this goal. This study was achieved through the following steps:

- Identify three geometrically unique SMA SGF concepts that fulfill mechanical requirements.
- Examine each of the three concepts with a structurally-focused design of experiment process and identify the best concept for optimization.
- Optimize the selected concept using structural and aeroacoustic solvers in a surrogate model framework.
- Review the optimal configuration with novel visualization techniques and determine the feasibility to manufacture this configuration for experimental testing.

The three unique SMA SGF concepts were geometrically defined using computer aided design (CAD) as 2-dimensional structures with unit depth out-of-plane to represent the section spanning airfoil experimental setup. Additionally, each concept fulfilled the two mechanical requirements of cyclical deployments and retractions along with stowing from a deployed state in a different combination of methods.

The structural design of experiment (DOE) was executed using a structural solver and only considered structural objectives and constraints. The deployed pressure load on the SGF was be estimated from CFD results, and each configuration was tested in the deploy-retract load case and the deploy-stow load case. The results of this study both determined which SGF concept should be investigated further with optimization and informed the design bounds used in single-concept optimization.

The down-selected SGF concept was optimized with a surrogate model optimization tool to minimize the number of iterations required to find a near-optimal configuration. This tool was required since the optimization considered both structural and aeroacoustic simulations in determining the objective variables for each configuration, and both simulations have significant runtimes on the available computational hardware.

The simulation results of the optimal configuration found by the optimization procedure were converted to a three-dimensional format and placed in a mixed reality visualization scene. This three-dimensional representation of the configuration was oriented on top of the existing experimental test article to help future researchers determine the feasibility of manufacturing this configuration at experimental scale.

2. Methods

Five unique methodologies were investigated and incorporated into the design presented in this thesis. These are as follows:

- Structural analysis of superelastic SMAs using Abaqus Standard for Finite Element Analysis.
- Aerodynamic analysis of a NASA CRM airfoil and wing section using Star-CCM+ Computational Fluid Dynamics.
- Computational Aeroacoustic analysis of a computational domain representing a wing in a wind tunnel enclosed in anechoic chambers.
- Optimization of a complex design problem using the Efficient Global Optimization formulation.
- Visualization of complex results in a 3-dimensional environment using mixed reality hardware and custom software.

The distinct region for each of the fluid and structural analysis subdomains is shown in Fig. 2.1. Together, these five methods form the foundation for the results presented in later chapters, as well as providing a framework upon which future researchers can continue to improve.

2.1 SGF Geometry

The geometry of each SGF concept is unique to that concept. However, design variables with similar meanings were utilized to define geometric configurations within each concept. These variables are defined in Table 2.1. The indicated variable letters are used to refer to these design variables through the remainder of the document.

Thickness of the SGF configuration is always defined with the variable t. The variable c defines the connection point on the main wing for the Wing Fixed Mechanism Stowed (WFMS) and

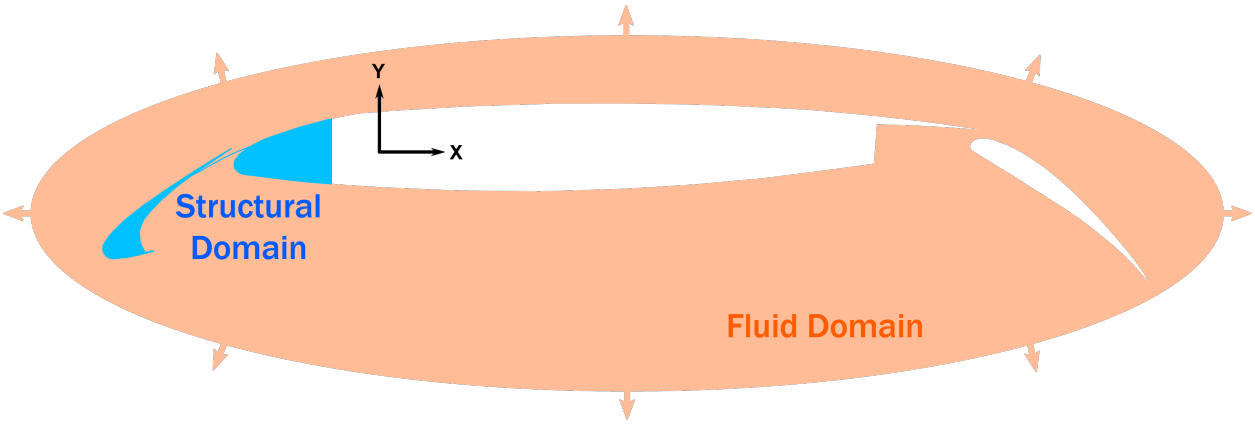

Figure 2.1: Comparison between the structural analysis domain, shown in blue, and the fluid analysis domain, shown in orange.

Table 2.1: Definitions for the four design variables for each of the three SGF concepts.

Variable	**Wing Fixed Mech. Stow**	**Wing Fixed Auto Stow**	**Interior Coil Auto Stow**
t	Thickness	Thickness	Thickness
c	Connection Point	Connection Point	Wing Point
e	End Point	End Point	Slat Point
a	Attachment Angle	Overwrap Coefficient	Pitch Coefficient

Wing Fixed Auto Stowed (WFAS) SGF concepts. For the Interior Coil Auto Stowed (ICAS) SGF concept, the variable c refers to the location on the main wing where a hole is cut from which the SGF configuration protrudes. For the WFMS and WFAS concepts, the variable e refers to the point on the main wing at which the configuration is designed to end if it were deformed to match the curvature of the wing between the defined connection point and this point. In the case of the ICAS concept, the variable e defines the location on the slat to which the SGF will be connected. Together, the design variables c and e determine the length of a SGF configuration for all three concepts, as well as the location of the configuration relative to the wing and slat.

The final design variable, a defines a different feature for each concept. For the WFMS concept, this variable refers to the angle from the negative x-axis at which the configuration is oriented. The variable a refers to the leading coefficient in the parabolic equation used to define the curvature of

a WFAS SGF. This function, which was chosen to approximate the curvature of the leading edge of the main wing, is

$$x = a \cdot (y + 1.5) \cdot (y + 41.5) + k$$
$$\text{where} \tag{2.1}$$
$$k = x_c - (a \cdot (y_c + 1.5) \cdot (y_c + 41.5)) .$$

In Eq. 2.1, x and y refer to the position in the domain, the subscript c indicates the coordinates represent the connection point, and the numeric values were chosen to approximate the wing curvature. Increasing the coefficient, a, results in a SGF configuration that has greater curvature relative to the main wing, which is why it is called the overwrap coefficient. For the ICAS concept, the variable a refers to the pitch of a spiral, which defines the distance between each loop of the spiral. This variable is shown as a coefficient in the equation for a spiral,

$$r = a \cdot \frac{\theta}{2\pi}. \tag{2.2}$$

The relative locations of the four design variables are shown in Figs. 2.2a, 2.2b, and 2.2c. In these figures, the SGF is indicated with a dotted black line in an approximately stress-free structural configuration. The variable t is indicated with blue arrows, the variable c is indicated with a green dot, the variable e is indicated with a red dot, and the variable a is indicated with purple arrows. The design variables c and e are both parameterized with a horizontal or vertical distance that is used to identify a point on the surface of the wing (or the slat in the case of the ICAS SGF).

2.2 Structural Analysis

A structurally feasible SGF can attach, stow, deploy, and retract without breaking or attaining undesirable shapes. The structural traits of a SGF design were simulated using Abaqus Standard FEA.

The SGF was simulated using continuum shell (SC8R) elements to facilitate simultaneous contact between the slat and wing on the top and bottom faces of the part. Continuum shell elements in Abaqus are eight node elements that function similarly to standard shell elements kinematically

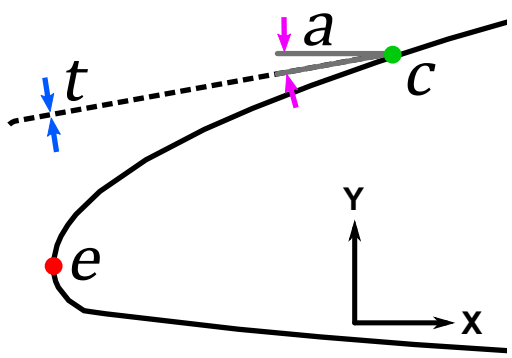

(a) Locations of the thickness, t, connection point, c, end point, e, and attachment angle, a, design variables for the WFMS SGF concept.

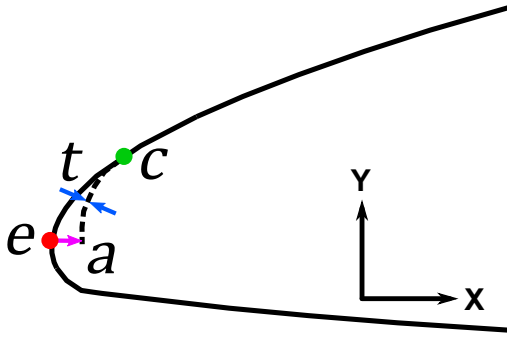

(b) Locations of the thickness, t, connection point, c, end point, e, and overwrap coefficient, a, design variables for the WFAS SGF concept.

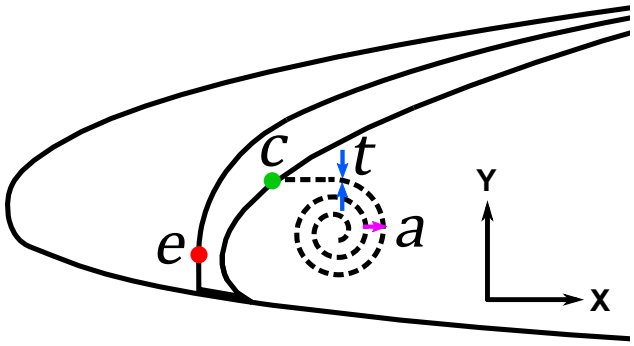

(c) Locations of the thickness, t, wing point, c, slat point, e, and pitch coefficient, a, design variables for the ICAS SGF concept.

Figure 2.2: Geometric definitions on the leading edge of the main wing for each design variable for all three SGF concepts. The SGF is indicated with a dotted line and the design variables are labeled.

Table 2.2: Material properties and their definitions for modeled SGF concepts used in conjunction with the Auricchio SMA model implementation in Abaqus [24]. Millimeters (mm) are used as the base unit for structural simulations in this thesis.

Constant	Value (Units)	Meaning
ρ	6.45E-9 ($\mathrm{tonnes/mm^3}$)	Density
E_A	48900 (MPa)	Austenite Elastic Modulus
ν_a	0.33	Austenite Poisson's Ratio
E_M	40000 (MPa)	Martensite Elastic Modulus
ν_A	0.33	Martensite Poisson's Ratio
H	0.044	Transformation Strain
C^M	10 (MPa/K)	Martensite Stress Influence Coefficient
σ^{Ms}	471 (MPa)	Initiation Stress for Forward Transformation
σ^{Mf}	518 (MPa)	Completion Stress for Forward Transformation
T_0	323 (K)	Reference Temperature
C^A	10 (MPa/K)	Austenite Stress Influence Coefficient
σ^{As}	197 (MPa)	Initiation Stress for Reverse Transformation
σ^{Af}	165 (MPa)	Completion Stress for Reverse Transformation
σ_c^{Ms}	471 (MPa)	Initiation Stress for Compressive Forward Transformation
H_V	0.044	Volumetric Transformation Strain
N_A	0	Number of Annealings

and constitutively, such that they are only accurate for structures where other dimensions are much larger than the thickness. However, unlike standard shell element nodes, continuum shell element nodes only have displacement degrees of freedom. Together, these properties make continuum shell elements accurate for a thin, sheet-like structure that requires two-sided contact interactions while making these elements much more computationally efficient compared to a standard continuum element.

The material applied to the SGF was a superelastic SMA defined using material characteristics from the Auricchio model [24]. A uniform temperature was applied to the SGF to begin the analysis with the material in the austenite phase. The Auricchio material was defined with 15 material properties that are presented in table 2.2. The properties for a thin SMA sheet were approximated from the properties used in [6].

SMAs are a heavy material that would increase both the weight and actuation force of an SGF

system, suggesting that other materials should be considered in this analysis. However, as can be seen in Fig. 2.3, only SMAs elastically recover the strain expected (>4%) in the proposed SGF concepts.

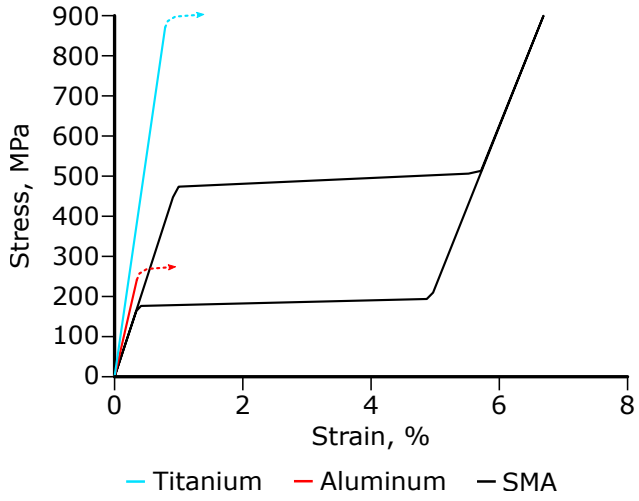

Figure 2.3: Stress-strain curve material comparison between SMA, Titanium, and Aluminium. The onset of plasticity is indicated by the dotted line arrows

The Auricchio SMA model is accurate for superelastic SMAs under the assumption that temperature is held constant throughout the analysis. This assumption is valid for this work because a SMA SGF is not designed for use as an actuator; rather it is designed to be a passive device that is actuated by pre-existing architecture (i.e., the slat actuators). While the ambient temperature will vary as the aircraft changes altitude, the SMA can be manufactured such that its transformation temperature is lower than the lowest temperature achieved during the course of a flight cycle.

For all SGF concepts, the structure must be simultaneously in contact with the leading edge of the main wing and the bottom side of the slat when the SGF is deployed. Wing-side contact interactions were simulated using frictionless contact in the tangential direction and a penalty stiffness formulation in the normal direction.[1] These settings assisted in solving as they allowed for com-

[1]Penalty stiffness refers to application of a penalty applied to this element in the stiffness matrix if a simulated node penetrates the defined contact surface. This penalty varies in accordance with a selected penalty function (e.g., linear) and with the normal distance that the node is interior to the contact surface.

pliance between contact forces and reaction forces from the fully fixed boundary condition at the wing-side end of the SGF. Contact interactions between the SGF and the slat were simulated with varying methods depending on the SGF concept. These interactions included frictionless contact, rough contact, and sliding friction contact. For the sliding friction contact, a friction coefficient of 0.2 was used to simulate a slat surface treated with low friction materials. The various slat-side contact interactions were necessary both to ensure completion of structural analysis simulations and to represent a realistic experimental interaction for calculation of analysis reaction forces.

As discussed, large strains, a superelastic material, and contact interactions are all features of structurally simulating an SGF. All of these features can cause a variable stiffness matrix during the analysis. Therefore, a nonlinear finite element analysis was required for all simulation steps.

For each SGF concept, the general structural simulation steps were: assemble the SGF with the wing and slat, deploy the slat, apply a representative pressure load, and retract the slat. Restart analyses were used to resume the analysis at the end of the pressure application step at which point the SGF is stowed, either mechanically or automatically depending on the SGF concept. These two load cycles are referred to as the deploy-retract cycle and the deploy-stow cycle, respectively. Static design steps were used when possible but for the auto stow concepts, the SGF is released from contact with the slat while under a pressure load, requiring an implicit dynamic analysis step.

In the deploy-retract cycle, retraction of the SGF was executed under a fully deployed pressure load to represent a "worst-case" analysis condition. The same method was used in the stowing step of the deploy-stow cycle. These analysis conditions add a margin of error that ensures an experimental SGF will retract and/or stow under a real pressure load.

The results of the simulations are checked to ensure that the yield stress of the selected material is not exceeded, that the SGF stays attached to the underside of the slat under the simulated pressure load, and that the SGF stows against the leading edge of the wing or inside of the wing. Additionally, the results are examined for large deflections which would change the assumed pressure field found from the initial CFD analysis.

The examined structural objectives were mass and actuation force required to deploy the slat.

Actuation force is an important structural result because, if a SGF is to be implemented on an existing aircraft, it should minimize the additional force required to deploy and retract the slat. This will allow for the continued use of preexisting actuators in a SGF implementation. The actuation force was measured by converting the moment required to analytically rotate the slat into a force using the distance from the moment application point to the centroid of the slat. This length is depicted in Fig. 2.4. The point depicted in this figure is also the point around which the slat is rotated in FEA.

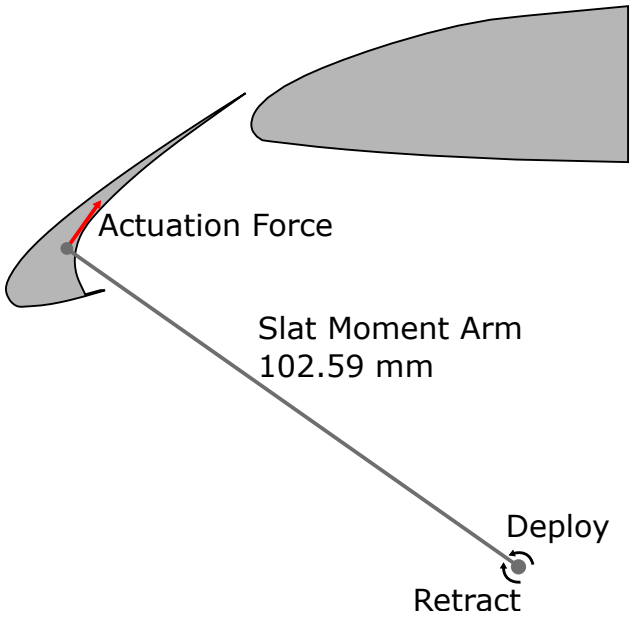

Figure 2.4: Depiction of the moment arm length used to determine the actuation force during slat deployment.

The structural analysis was scripted in Python and executed from the command line using structured text files as variable input/output to the FEA solver. This allowed for perfect repeatability and random inputs provided by the optimization code.

2.2.1 Wing Fixed Mechanism Stowed SGF

The wing Fixed Mechanism Stowed (WFMS) SGF was generally defined as a straight line fixed to the wing at one end and extending out from the wing. A parabolic function approximation

of the wing leading edge was utilized to determine the relationship between the length of a WFMS configuration and the point on the main wing at which the tip of a fully stowed SGF would contact. An image of a geometrically defined WFMS SGF configuration is shown in Fig. 2.5.

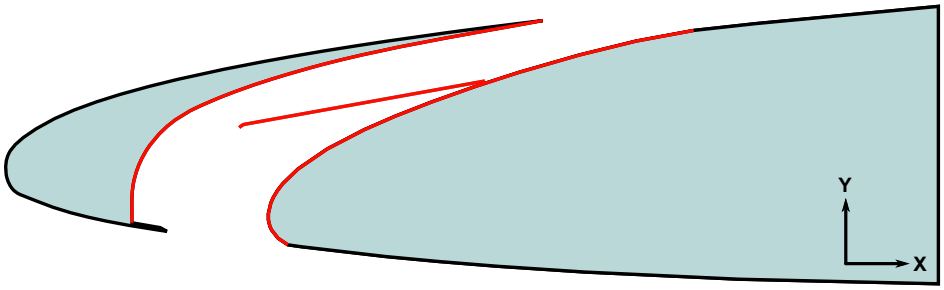

Figure 2.5: An example Wing Fixed Mechanism Stowed SGF design geometry. Regions where contact is simulated are highlighted in red. The slat is moved from the assembled position to provide visibility of all surfaces as the WFMS SGF is defined to extend beyond the surface of the slat prior to structural assembly.

This SGF was assembled by moving the slat such that a point near the tip of the SGF was in contact with the bottom surface of the slat. A curved tip, similar to a sled, was defined at the free end of the WFMS SGF so that it would slide smoothly along the bottom side of the slat. The slat-SGF contact interaction was defined such that the SGF could not penetrate the bottom surface of the slat in the normal direction and such that motion tangentially along this surface was inhibited by a penalty friction formulation.[2] This contact formulation allowed for separation from the slat surface such that the SGF could be mechanically stowed. A frictionless contact formulation was used for the tangential interaction between the SGF and the main wing and a no penetration definition was used for the normal direction. These contact interactions are implemented on the surfaces highlighted in red in Fig. 2.5

A mechanical connection in the form of wires placed periodically along the span of the SGF was simulated using displacement connector constraints in Abaqus. To manually retract the SGF,

[2]Penalty friction refers to use of a penalty formulation to limit motion of nodes to a set amount, penalizing the corresponding elements of the stiffness matrix that exceed this set motion.

the length of connectors was modified to pull the SGF down to the leading edge of the wing. The point on the wing at which the SGF is pulled to was identified using the parabolic approximation function. The axial connectors are highlighted in Fig. 2.6.

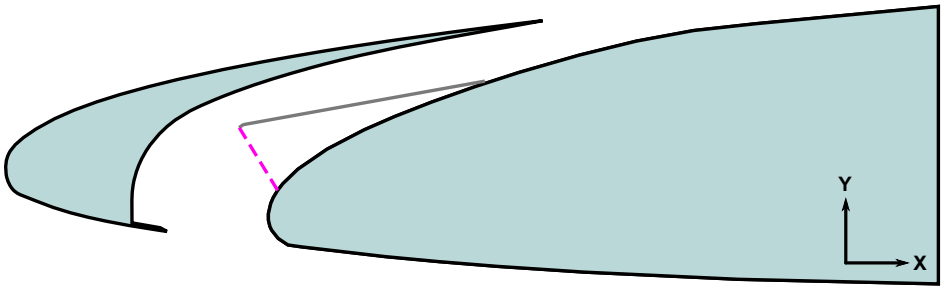

Figure 2.6: Stowing connectors simulating wires for the manual stowing mechanism in the WFMS SGF concept.

The WFMS SGF was loaded with a uniform pressure load applied to the bottom surface. The only boundary condition applied to this SGF concept is a fixed boundary condition specified at a unit length upper section of the SGF. This upper section is curved to match the curvature of the corresponding section of the main wing, as if the fixed end of the SGF were epoxied to the wing. The WFMS SGF was meshed using continuum shell elements to facilitate the multi-sided behaviors described. An image of the part mesh showing shell surface directionality and unit depth out of plane is presented in Fig. 2.7.

2.2.2 Wing Fixed Auto Stowed SGF

The Wing Fixed Auto Stowed (WFAS) SGF was structurally analyzed using the same general procedure outlined previously. Specific to this design was the requirement to define the initial shape of the SGF such that it lies flat on the leading edge of the wing while maintaining enough stress to not be perturbed by the aerodynamic forces present in the open gap flow configuration. To achieve this, the leading edge of the wing was again approximated using a parabolic curve. The apex of this curve was then offset slightly into the wing, creating a SGF that would curve from an upper point on the surface of the wing to an end point inside of the wing in its stress free state.

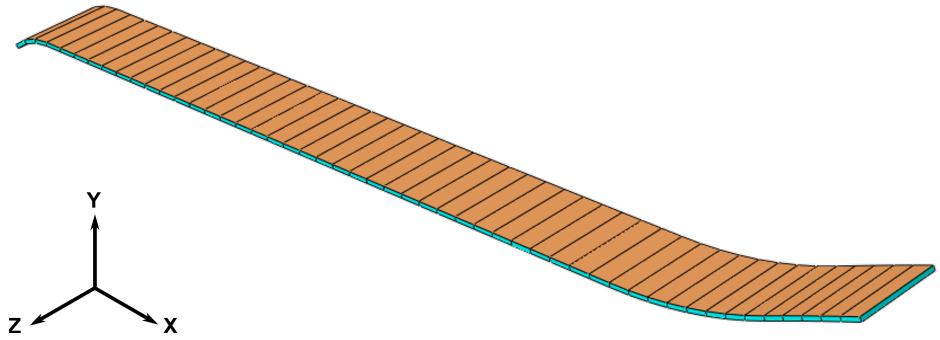

Figure 2.7: Example mesh of a WFMS SGF configuration where orange denotes the top surface of the element.

An image of the WFAS SGF geometry is shown in Fig. 2.8. A primary assembly step was utilized to move the SGF into a position lying on top of the leading edge of the wing. Then, a secondary assembly step was used to attach the SGF to the bottom surface of the slat.

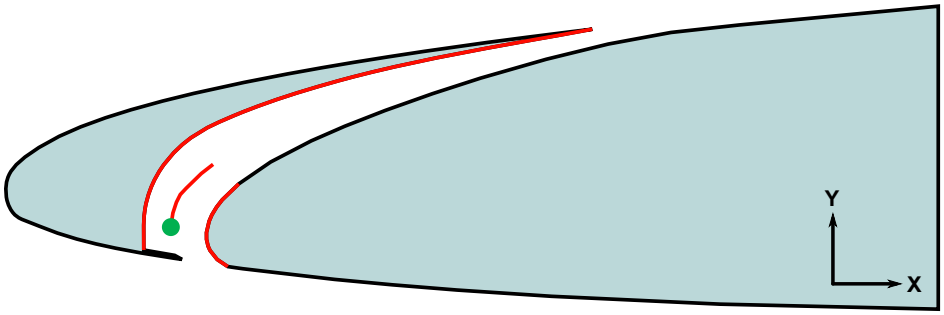

Figure 2.8: An example Wing Fixed Auto Stowed SGF design geometry with relevant contact interactions highlighted in red (frictionless surface contact) and green (no penetration and no separation contact). The wing is moved from the assembled position to provide visibility of all surfaces as the WFAS SGF is defined to intersect the wing prior to structural assembly.

A tangential frictionless sliding contact interaction was defined between the tip of the SGF and the slat bottom surface. This contact interaction functioned similar to a rail and roller system such that the SGF tip remained attached to the slat at all times but was allowed to translate along the bottom surface of the slat. This contact interaction is indicated at the tip of the SGF with a maroon circle in Fig. 2.8. Frictionless tangential interactions along with no penetration interactions

in the normal direction were used to define contact between the WFAS SGF surfaces, the slat, and the wing. The regions highlighted in red in Fig. 2.8 show the locations of these two contact interactions.

A pressure load was uniformly applied to the bottom surface of the WFAS SGF, and a fixed boundary condition was used at the junction of the SGF with the wing. Both of these conditions mirror the methods used for the WFMS SGF concept. An example of a continuum shell element mesh of a WFAS SGF configuration is shown in Fig. 2.9.

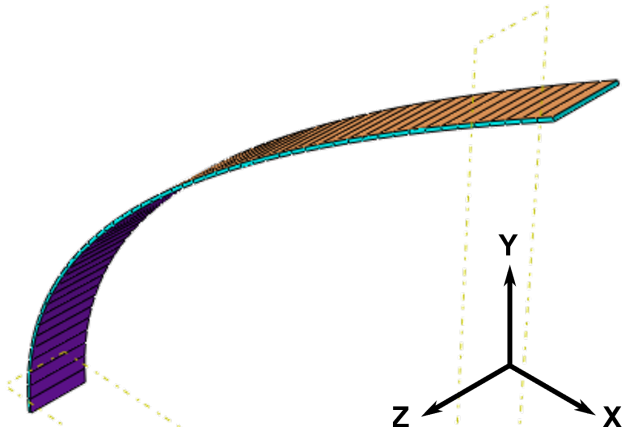

Figure 2.9: Example WFAS SGF mesh, where orange denotes the top surface of the element and purple denotes the bottom surface of the element.

2.2.3 Interior Coil Auto Stowed SGF

Unlike the other two SGF designs, the interior coil auto stowed (ICAS) SGF design was not defined by matching the curve of the leading edge of the wing. Rather, an Archimedean spiral was defined with parameters such that the extended length of the spiral spans the gap between the deployed slat and a slot on the leading edge of the wing.

Equation 2.2 represents the formula used to generate ICAS spiral configurations. In this equation, θ varies between a pre-set start angle, and an end angle determined such that the configuration length spans maximum the distance between the slat and main wing. The end angle is adjusted

such that a ICAS SGF configuration always ends at an even increment, n, of the equation $n \cdot \frac{\pi}{2}$, resulting in a SGF free end at the top of the spiral.

The coil SGF was placed inside of the wing with the assumption that there is not much interior structure near the tip of the leading edge of a wing to interfere with its placement. A 1.0 mm vertical slot was cut in the surface of the wing leading edge and the tips of this slot were rounded to enable smooth assembly and deployment of a SGF in contact with the exterior surface of the wing. Additionally, a 1.0 mm deep port was cut into the slat to realistically simulate a fixed connection between the end of the SGF and the bottom of the slat. The free end of the SGF was fixed to this port prior to structural assembly. An image of an ICAS SGF geometry is shown in Fig. 2.10.

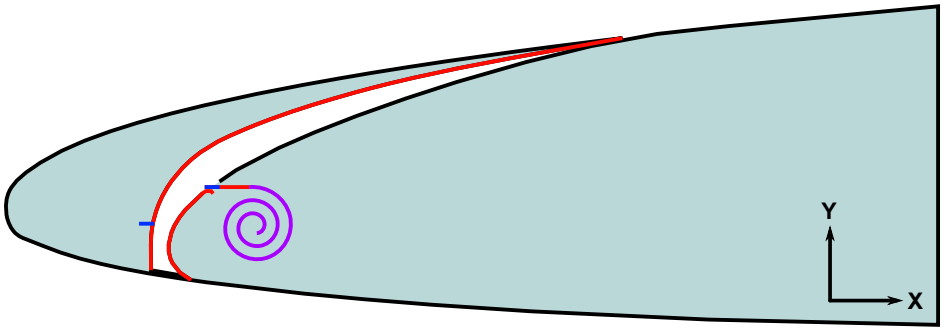

Figure 2.10: An example of an Interior Coil Auto Stowed SGF design geometry with surfaces on which contact interactions are applied highlighted in red (frictionless surface contact), blue (no slip contact), and purple (no penetration self contact).

The ICAS model was assembled by placing the tip of the SGF in the slat port with the slat in the retracted position. The contact interaction defined between the tip of the SGF and the slat port represented a fixed connection that could be released to stow the SGF. Also, a no penetration condition was applied as a self contact interaction such that a ICAS SGF would unspool, similar to a tape measure. These two contact interactions are shown in maroon and purple in Fig. 2.10, respectively.

The contact interactions between the upper surface of the SGF and the slat, and the bottom sur-

face of the SGF and the wing are frictionless, no penetration interactions similar to those described for the WFAS and WFMS SGF concepts. These contact interactions are shown in red in Fig. 2.10.

The ICAS SGF was loaded with a uniform pressure load applied to the outer half of the SGF to roughly approximate applying a pressure load to exclusively the deployed portion of the ICAS SGF. Also, the ICAS SGF was fixed with a boundary condition at the interior end of the spiral. This simulated a SGF attached to a mounting rod internal to the wing. An image of the ICAS SGF geometry mesh is shown in Fig. 2.11. The top and bottom surfaces of the elements are uniformly defined through the spiral such that the self contact interaction functions correctly.

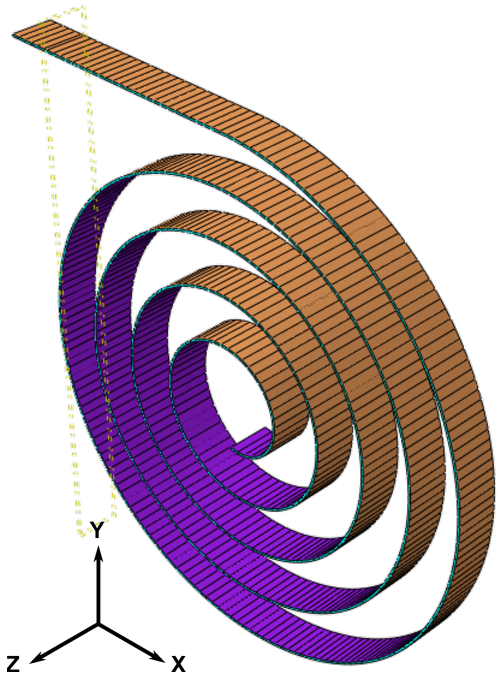

Figure 2.11: Example mesh of an ICAS SGF, where orange denotes the top surface of the element and purple denotes the bottom surface of the element.

An important note for the ICAS SGF concept is that extending the SGF into a fully deployed position required extremely large deformations. These deformations combined with the small mass of the SGF caused instabilities during the dynamic step simulating the stowing procedure. Any simulated ICAS SGF configuration moved in a manner similar to a whip or an elastic band

during this step. Attempts were made to resolve these instabilities by varying solver settings and constraining movement of the SGF. While some stowing simulations were completed, they required many hours to complete and often ended prior to finding a stabilized solution. Therefore, the stowing procedure was not considered in the design analysis of the ICAS SGF concept.

2.2.4 Finite Element Analysis Results

Important results from the structural FEA include contours of stress and martensite volume fraction on a studied SGF. (Martensite volume fraction represents the fraction of a structural node that is transforming from austenite to martensite with a number between 0 and 1). These contours were difficult to view because an SGF is a relatively small part compared to the size of the structural domain. Therefore, sections of the structural domain were magnified to highlight these results. An example of FEA results with the important sections highlighted in red are shown in Figs. 2.12a and 2.12b. Each SGF concept was simulated using only one cell in the out-of-plane (z-axis) direction facilitated by symmetry boundary conditions. However, presented FEA results are extruded to display a section that is about 10% of the span of the experimental wing model.

As in Fig. 2.12b, three views are shown for each structural result in the following chapters: a side view, a top view, and an isometric view. These correspond to subfigures A, B, and C, respectively, in this and all similar figures. Note that the slat is removed from the top view such that the full SGF can be viewed in all states. Additionally, three stages of the analysis are presented as FEA results: the SGF assembled with the wing and slat, the deployed SGF under an applied pressure load, and the SGF stowed after separation from the slat. The ICAS SGF is shown in its retracted state instead of the stowed state because stowing was not considered in generation of results for this concept.

2.3 Aerodynamic and Aeroacoustic Analysis

The aerodynamic forces applied to the SGF at every point in the deploy-retract or deploy-stow cycles are both dependent on and deterministic of the structurally realized deformations. Also, aeroacoustic performance of the deployed SGF is directly dependent on the aerodynamic

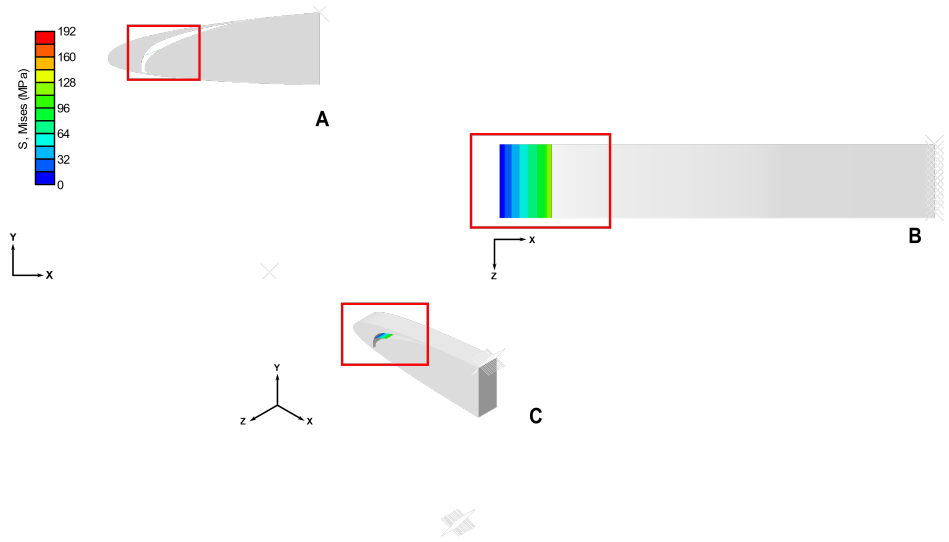

(a) Images of FEA results viewed with the whole structural domain. Any results in these images are nearly impossible to interpret. The regions boxed in red are magnified in subsequent figures

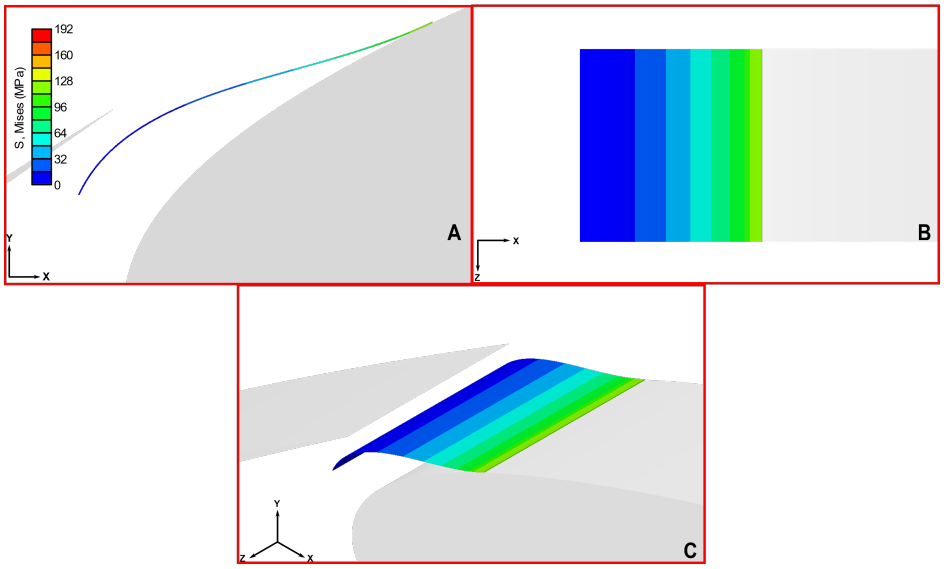

(b) Magnified regions of the FEA result domain. These images show the result contours and shape but do not show the entire structural domain.

Figure 2.12: An example of an FEA result that is difficult to view and how it can be magnified to clearly show the results. The magnified sections are boxed in red.

flow field. To completely examine this type of relationship, a computationally intensive coupled Fluid-Structure Interaction (FSI) scheme is necessary. However, to achieve an adequately accurate description of the design space for multiple SGF design concepts, as is the goal of this study, the fluid and structural interactions can be approximated and the analysis can be decoupled. The simulation was decoupled by using an approximated pressure force on the fully deployed SGF in the structural analysis. Aerodynamic and aeroacoustic analyses of an HL-CRM wing were executed using Star-CCM+ solvers. The baseline wing was oriented at 6° angle of attack in a representative wind tunnel domain.

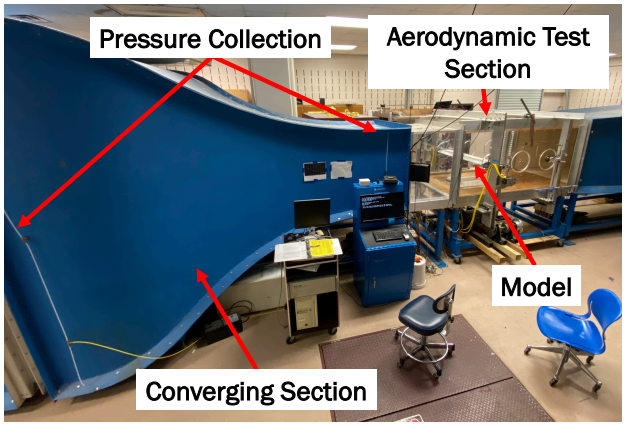

(a) Texas A&M 4 ft. by 3 ft. low speed wind tunnel with the aerodynamic test section labeled.

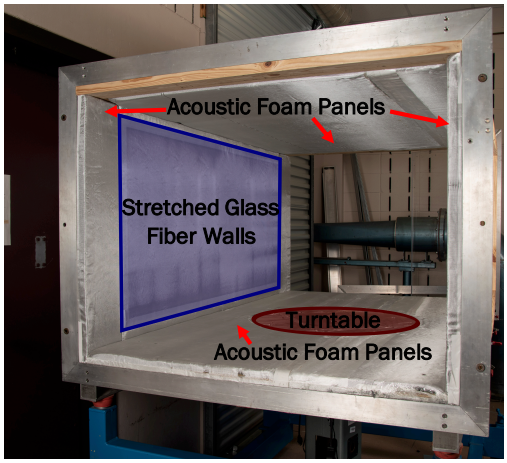

(b) Acoustic test section for use in the experimental wind tunnel setup. This section can be moved to replace the aerodynamic test section. The wing (not pictured) can be mounted vertically in this section.

Figure 2.13: Images of the aerodynamic (left) and acoustic (right) wind tunnel sections [25].

The dimensions of the experimental wind tunnel were used to define the computational domain used in CFD analysis. The wind tunnel and aerodynamic testing section are shown in Fig. 2.13a. The experimental test sections are designed to be switchable. The experimental acoustic test section, shown in Fig. 2.13b, influenced the domain for the computational aeroacoustic analysis presented herein. Acoustic experimental measurements are taken using a microphone array located

in a clamshell anechoic chamber next to the acoustic test section. The location of this microphone array was used to define the location of the microphone point receiver in aeroacoustic analysis.

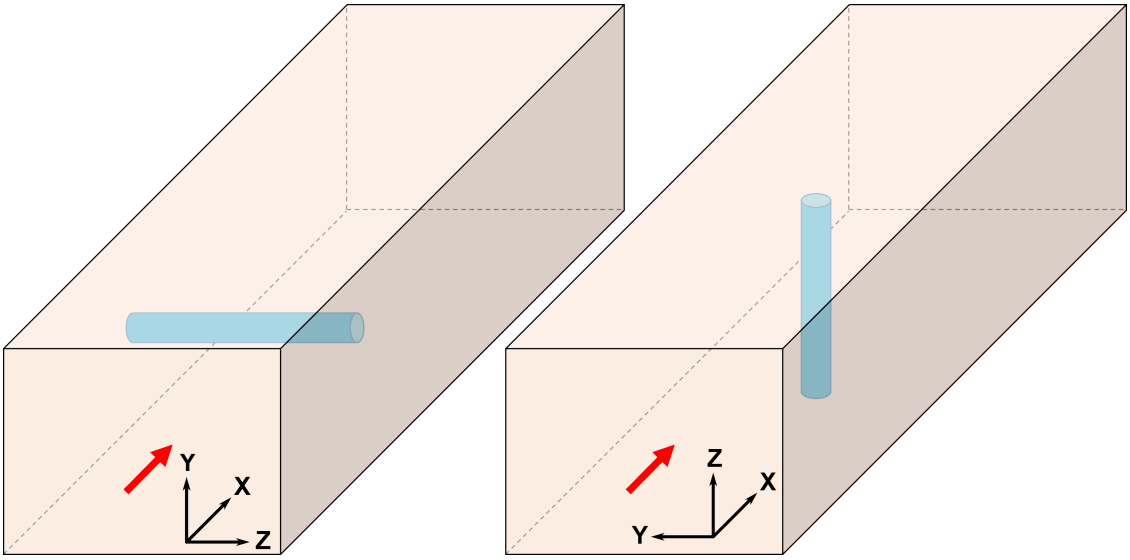

Figure 2.14: Comparison of the domain and wing fixed coordinate system for the simulated aerodynamic wind tunnel section (left) and simulated aeroacoustic wind tunnel section (right). The orange rectangles represent the tunnel sections and the blue cylinders represent the wing mounted in each section. The red arrow represents the flow direction through the section inlet.

Simulated domains for each wind tunnel section are shown in Fig. 2.14. The left domain represents the aerodynamic wind tunnel section with the wing, shown as a blue cylinder, mounted horizontally. The right domain represents the aeroacoustic wind tunnel section with the wing mounted vertically. The red arrows depict the direction of flow into the section domain. These graphics represent the extent to which the wind tunnel domains pictured in Figs. 2.13a and 2.13b are translated into aerodynamic simulations. Note that the coordinate systems used are relative to the wing, so the coordinate system is rotated about the x-axis even though the external dimensions of the sections do not rotate. Also, note that the wing is positioned more centrally along the x-axis in the acoustic section compared to its forward position in the aerodynamic section. These positions and coordinate systems are used for all subsequent depictions.

The microphone array used in experimental testing is simplified to one microphone positioned

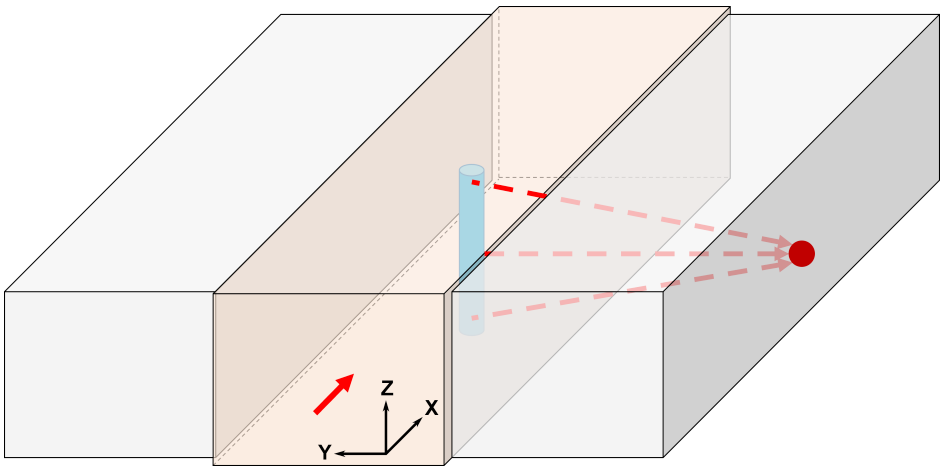

Figure 2.15: Graphic of the geometry of the anechoic chambers surrounding the acoustic test section. The experimental anechoic chambers are represented with gray boxes, and the location of the simulated microphone receiver is shown with a maroon circle. The dotted red lines represent sound propagating to the microphone from the wing.

in space for aeroacoustic simulations. Also, any features outside of the described tunnel section domain, such as clamshell anechoic chambers, are not simulated. Ideally, these features would be incorporated into analysis boundary conditions. A simple approximation of these features as a freestream boundary condition was used in this analysis. The geometry of the microphone receiver relative to the simulated aerodynamic domain and the position of the experimental anechoic chambers is shown in Fig. 2.15. In this figure, the microphone receiver is shown with a maroon circle and the anechoic chambers are shown with gray boxes. This figure also depicts how the domain for aeroacoustic analysis extends beyond the indicated orange domain for aerodynamic analysis.

For all analyses, slip wall boundary conditions were used on the parallel faces of the domain to simulate smooth walls. These boundary conditions ignore any viscous effects that would modify the flow in the direction tangential to the wall. The locations of these boundary conditions for the domain modeled after the acoustic experimental setup are shown in Fig. 2.16b. Velocity inlet and mass flow outlets were used for the front and back faces of the flow domain, as is shown in Fig. 2.16c.

For the acoustic analyses, freestream boundary conditions were used to allow for acoustic prop-

agation normal to the domain boundary, as is shown in Fig. 2.16a. These freestream conditions do not accurately represent the wall-like boundary found at the glass fiber mesh walls in the acoustic test section. However, wall boundary conditions in Star-CCM+ were found to prevent use of the aeroacoustic solver. Furthermore, the application of both outlet and pressure outlet boundary conditions to these planes caused solver instabilities and failure of the CFD analysis. Freestream boundary conditions set to the same velocity as the inlet boundary condition were found both to allow for aeroacoustic analysis and to prevent flow structures from crossing the boundary, resulting in a stable flow in the region of interest. This boundary condition assumption inhibits the accuracy of the CFD analysis and is an important topic for future investigation.

The Star-CCM+ user manual, the 2019 review paper by Götten et. al. and the NASA Langly 2D Multielement Airfoil Verification Case were utilized as reference works to determine the mesh and flow solver settings for aerodynamic and aeroacoustic analysis [26, 27, 28]. The aerodynamic and aeroacoustic simulation methodologies are described in the following sections.

2.3.1 Aerodynamic Analysis

A steady Reynolds-Averaged Navier Stokes (RANS) solution with a k-ω turbulent flow model was used as the initial CFD solution. The flow was modeled through a domain with walls on the sides, top, and bottom to represent an experimental wind tunnel section. Using the initial solution from the steady CFD result, an unsteady Large Eddy Simulation (LES) is run to create the input for the aeroacoustic analysis which is described in the following section.

2.3.1.1 3-Dimensional Aerodynamic Effects

To determine the impact of 3-dimensional effects for this problem, an analysis two dimensional face of the flow field parallel to the flow direction was meshed using the automatic 2D mesher in Star-CCM+. This 2D mesh was then extended with a variable number volume layers to fill the domain.

The number of volumetric layers in the mesh was decreased from 48 to 0, with 0 layers representing a 2-dimensional domain, to determine the impact of 3-dimensional effects on aerodynamic

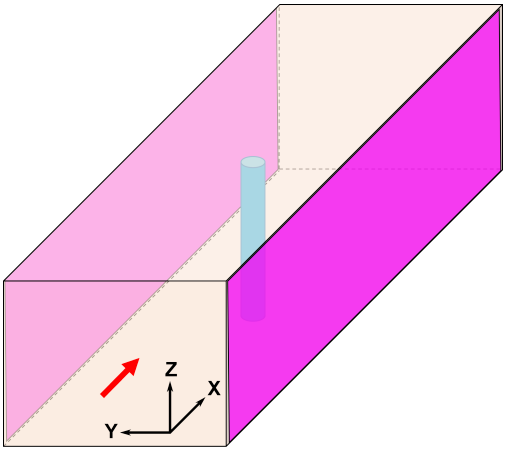

(a) Freestream boundary conditions.

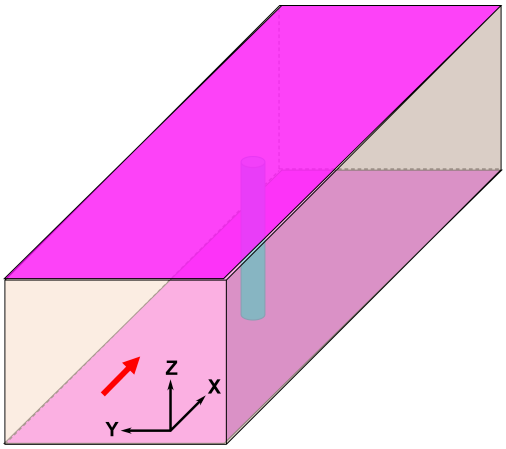

(b) Slip wall boundary conditions.

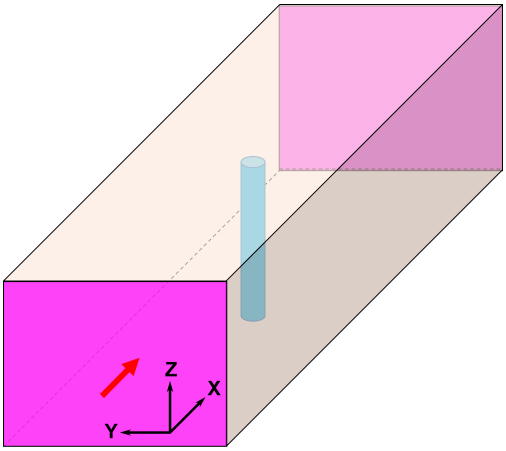

(c) Velocity inlet and outlet boundary conditions.

Figure 2.16: Boundary conditions used in Star-CCM+ for the domain representing the acoustic experimental configuration. The surfaces highlighted in pink in each subfigure are the described boundary condtions.

Table 2.3: Lift and drag coefficient CFD results compared to simulation runtime and number of volumetric layers for several directed meshes generated using Star-CCM+.

Number of Volumetric Layers	Lift Coefficient	Drag Coefficient	Runtime (s)
48	2.22	0.105	1344
24	2.21	0.106	781
12	2.21	0.108	493
6	2.20	0.107	356
3	2.20	0.108	278
2	2.20	0.106	302
1	2.20	0.107	165
2D Mesh	2.23	0.106	54

CFD results for the case of the section spanning HL-CRM wing. These simulations were executed using a mesh refined around wing with some wake refinement. The converged lift and drag coefficients were found to change very little, fluctuating only on the order of the third significant figure for each. These results are presented in Table 2.3.

Using a 12 layer volumetric mesh, lift and drag coefficients were determined for a selection of potential flow solvers in Star-CCM+. These results are presented in Table 2.4. It is clear that the segregated flow solver results in greater lift and drag compared to the coupled flow solver.[3] Furthermore, it appears that unsteady, DES simulations with either Spallart-Allarmes or k-ω turbulence models are the closest to matching the experimentally determined results. These observations are supported by recommendations to use unsteady simulations for aeroacoustics simulations and to use either Spallart-Allarmes or k-ω turbulence models with the segregated flow solver for aircraft-like simulations.

2.3.1.2 Aerodynamic Mesh Convergence Study

A mesh convergence study was executed by comparing results to those found in the 2D multi-element airfoil verification case study, [28]. This airfoil is a newer version of the HL-CRM airfoil studied in this analysis with the main changes being the increased chord and shortened slat. These

[3]The segregated flow solver in Star-CCM+ is a pressure-based solver that solves decoupled conservation equations in sequential order. The coupled flow solver is a density-based solver that solves coupled conservation equations simultaneously [27].

Table 2.4: Turbulence models available in Star-CCM+ compared to experimental results using lift and drag coefficients. Note that the italicized rows (9 and 10) were run using a 2-dimensional mesh instead of the 12 layer 3-dimensional mesh used for the other simulations.

Time	**Flow**	**Turbulence**	**Lift Coefficient**	**Drag Coefficient**
Steady	Segregated	RANS, k-ω	2.29	0.10
Unsteady	Segregated	RANS, k-ω	2.20	0.12
Unsteady	Segregated	RANS, Sp-Al	2.10	0.11
Steady	Segregated	RANS, Sp-Al	2.30	0.11
Unsteady	Segregated	LES	2.10	0.13
Unsteady	Segregated	DES, Sp-Al	2.17	0.14
Steady	Segregated	RANS, k-ϵ	2.19	0.09
Steady	*Segregated*	*RANS, k-w*	*2.22*	*0.11*
Steady	*Coupled*	*RANS, k-w*	*2.00*	*0.095*
Experimental			2.16	0.18

changes came as a result of a more inboard section on the CRM wing being used as the airfoil section with the chordwise part located at Y=640 inches from the model centerline. Additionally, this model uses a blended section cut that is slightly modified from an orthogonal cut to the leading edge up to 25% of the chord and then parallel to the chord from that point on to the end of the wing.

In the study, the airfoil was placed in a 2-dimensional domain with farfield Riemann boundary conditions imposed at 1000 chord lengths away from the airfoil. The flow was oriented such that the airfoil was at 16 degrees angle of attack and the Reynolds Number relative to a unit chord length was 5 million, given a freestream Mach number of 0.2.

To compare results to this domain, while learning useful information about the thesis objective, this domain was modified to represent a wind tunnel test configuration, similar to the CFD domain used in the SGF design study. The same airfoil section was used with the same Mach number as an inlet condition to the tunnel domain. The chord was reduced to 0.3216 of the original chord to represent the length scale of the experimental test article used in the real wind tunnel.

CFD meshes were generated in the tunnel domain to have similar features to the published meshes. Specifically, the meshes generated were highly refined around the airfoil with some refinement in the wake of the airfoil. An example of this mesh in the tunnel domain is shown in

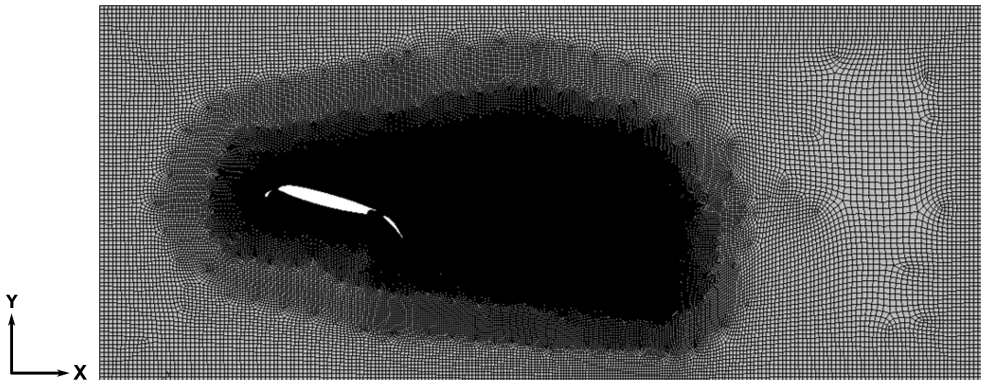

Figure 2.17: Mesh and domain used in the modified version of the NASA HL-CRM analysis.

Fig. 2.17.

Five meshes were generated and run with a coupled temperature and pressure flow solver using steady Reynolds Averaged Navier-Stokes turbulence with the Spalart-Allmaras formulation. The number of cells was roughly doubled for each generated mesh, and the number of cells can be seen in Table 2.5. Each CFD run was allowed to iterate until the residuals and the monitored coefficients stabilized for several hundred iterations. Usually, this took around 5000 iterations, but more iterations were required for the most refined meshes. Images of the Mach number in the domain, like Fig. 2.18, also revealed when the solution had stabilized as the low-speed wake behind the flap coalesced into an unchanging structure. The fifth and most refined mesh was also run with freestream conditions in place of the tunnel walls in an attempt to more closely match the reference results.

The results of this study compared to the reference are shown in Fig. 2.19a and Fig. 2.19b. As can be seen from these plots, the solutions found using the modified domain are similar but not completely analogous to the solutions found in the literature. This suggests that there will be error in the optimization procedure. Furthermore, computational limitations mandated an optimization CFD cell count most similar to the third coarsest mesh tabulated. However, it is important to recognize that both the computed lift and drag appear to be approaching the published value as the mesh element count increases. Therefore, a simple future improvement to the procedure presented herein would be refining the mesh and mitigating the increased runtime with usage of a supercomputer.

Table 2.5: Detailed results from mesh convergence study on modified 2D HL-CRM compared to published results from [28]. Italicized row contains results from repeated 15.6 million cell mesh using freestream boundary conditions instead of wall boundary conditions.

Cells (mil.)	**Base (m)**	**Mesh Time (hrs.)**	**Solve Time (hrs.)**	**Processors**	**C_L**	**C_D**
0.15	0.01	-	-	10	3.48	0.205
0.56	0.005	-	0.87	10	3.56	0.161
2.21	0.0025	1.5	3.3	10	3.62	0.147
10.0	0.00125	6.33	14.6	20	3.76	0.142
15.6	0.001	14.0	60.1	20	3.83	0.138
15.6	-	-	-	-	*3.83*	*0.198*
Published	-	-	-	-	3.79	0.062

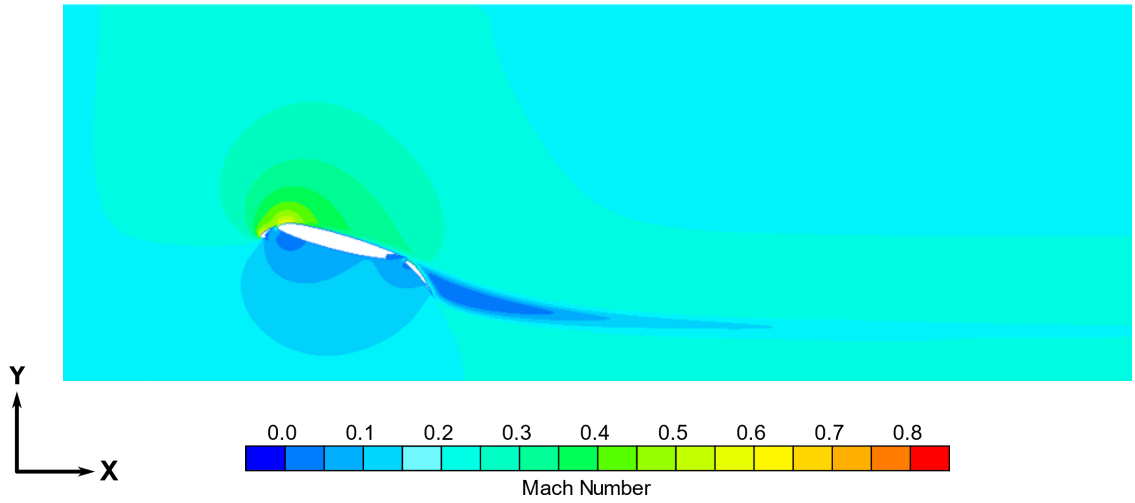

Figure 2.18: Mach Number contours for the wind tunnel domain with the 15.6 million cell refined mesh.

2.3.2 Aeroacoustic Analysis

A successful SGF primarily serves to reduce noise coming from the wing compared to the wing without any design modifications. Therefore, it is necessary to determine if the proposed SGF design configurations demonstrate a potential for noise reduction when compared to an unmodified wing using a computational aeroacoustics (CAA) analysis. Similar to the aerodynamic analysis, aeroacoustic analysis was completed using a model of the NASA HL-CRM wing in the low-speed

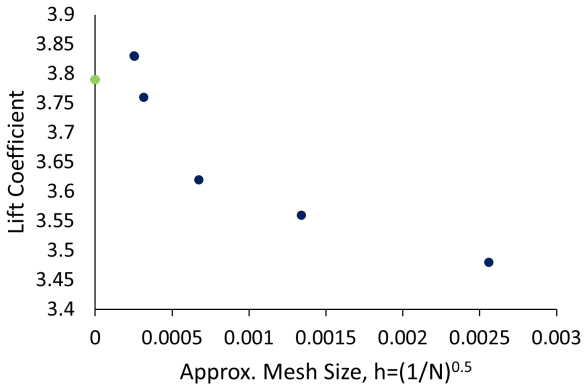

(a) Lift coefficient versus approximate mesh size.

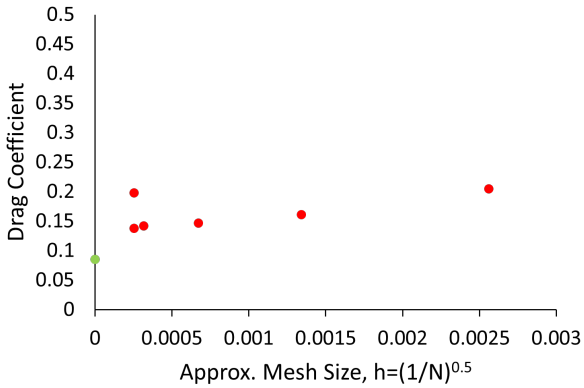

(b) Drag coefficient versus approximate mesh size.

Figure 2.19: Lift and drag coefficients for the modified 2D HL-CRM study where N is the number of cells in the mesh and the green dots represent the exact solution found in [28].

wind tunnel domain. However, the speed for this analysis was 35 m/s (approximately Mach 0.1) and this analysis was executed using the segregated flow solver instead of the coupled flow solver to better capture turbulence shedding. Furthermore, while a 2-dimensional domain was shown to be accurate for aerodynamic results a 3-dimensional domain is necessary to simulate the procession of acoustic pressures to the edges of the domain.

To mesh this domain for aeroacoustics analysis, local mesh refinement was required to capture the dominant sound waves. The mesh was generated to capture flow fluctuations on the order of micro-pascals to capture acoustic pressures, so the mesh must be refined beyond what is required for accurate aerodynamic simulations. The mesh frequency cutoff function was maximized in the regions of acoustic interest, namely the trailing edge of the slat and the leading edge of the flap. This is shown in Fig. 2.20. A predicted mesh cutoff frequency of about 3 kHz in these regions was achieved with a 12 million cell mesh generated with the trimmer mesh algorithm. This mesh was generated with additional refinement around the trailing edge of the slat and the leading edge of the flap using cylindrical volumetric controls.

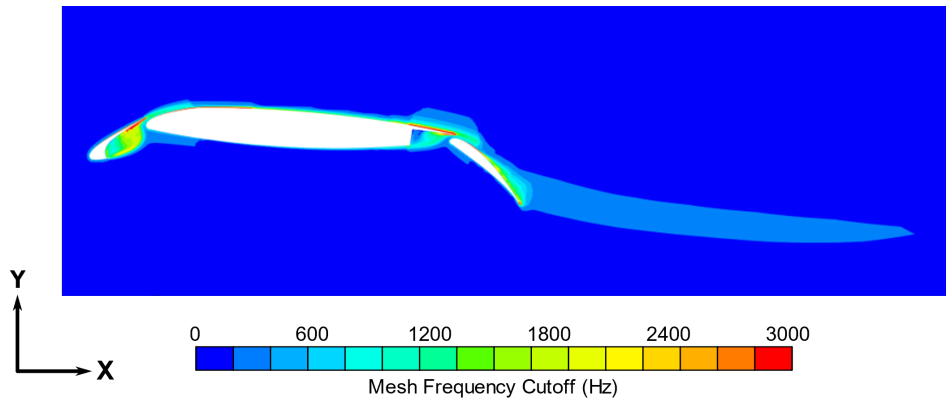

Figure 2.20: Mesh cutoff function results for a refined mesh showing the areas which are expected to be influential for aeroacoustic results.

Twenty prism layers starting from the surface of the wing model and extending to 0.2 m above the wing were suggested to capture the entirety of the boundary layer. The height of the first

prism layer next to the wing surface was 2.5E-5 m to ensure accurate representation of the near-surface flow behavior. The sufficiency of this layer was checked using the Wall y+ function once a simulation has been completed. For aeroacoustic analysis, the ideal wall y+ value is around one; a first prism layer of this height achieved a wall y+ near one in most regions.

These values were determined using the prediction functions found in the paper by Götten et. al [27]. Furthermore, the trimmer meshing algorithm was used to generate polyhedral cells, and the prism layers were stretched with a hyperbolic function according to the recommendations in this review paper.

To facilitate optimization iterations at a reasonable rate (approximately one iteration per 12 hours), the CFD mesh was coarsened from these ideal values. It was determined that the surface level interactions were the most important for computing aeroacoustic quantities, so the height of the first prism layer was unmodified. However, the total height of the boundary layer and the number of cells in the boundary layer were each cut roughly in half. Additionally, no wake refinement was enabled and the number of cells in the flow direction was significantly reduced. These simplifications resulted in the observed mesh cutoff frequency decreasing from a maximum around 3 kHz to a maximum around 1 kHz.

An example of the mesh used in the optimization procedure is shown in Fig. 2.21. This mesh was approximately the most refined mesh for which optimization iterations could be completed on locally available hardware. In some cases, a more refined mesh required more than the available 64 Gb of RAM to solve the meshing algorithm and store flow quantities during simulation. An image of a Wall y+ calculation demonstrating the successful retention of surface-level refinement is shown in Fig. 2.22. For the blank wing at 6° angle of attack with no SGF treatment applied, the coefficients of lift and drag were found to be 2.98 and 0.09. These values are similar to results from previous experimental analysis but their inaccuracy reflects the low quality of the mesh in wake region. The experimental lift and drag coefficients for this configuration were reported as 2.01 and 0.14. The previous experimental analysis is discussed further in Appendix 8.

The noise reduction objective was investigated using an aeroacoustic analysis in Star-CCM+.

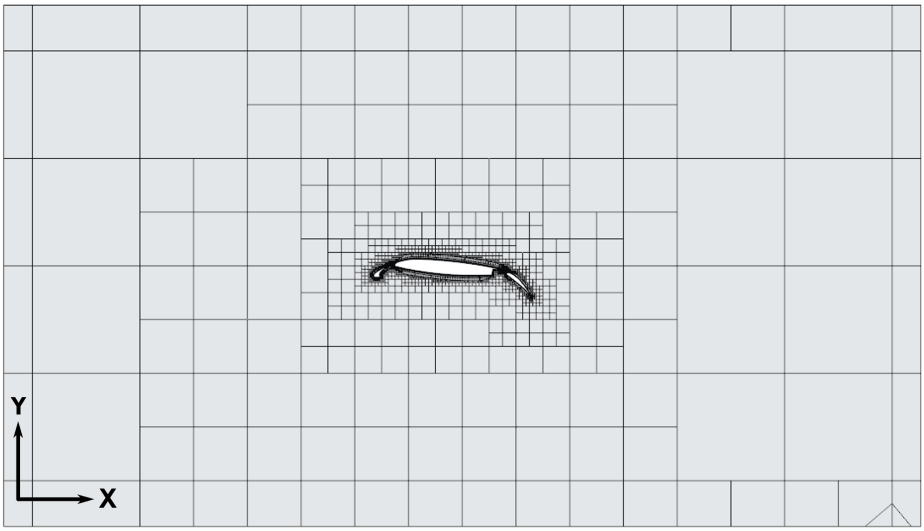

Figure 2.21: Mesh and domain used in the SGF CAA optimization analysis.

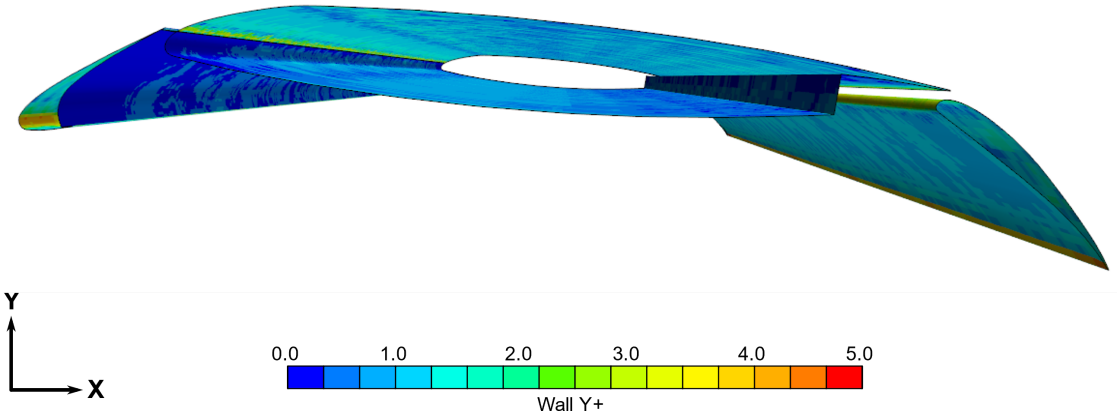

Figure 2.22: Wall y+ values for the example mesh after a completed analysis.

The Ffowcs Williams-Hawkings (FW-H) aeroacoustic equations are used to propagate the acoustic effects to the receiver from the results of a nearfield turbulent Direct Eddy Simulation (DES). The acoustic receiver is positioned 1.5 meters beneath the wing (along the negative y-axis) to match the experimental procedures in [11] and [8]. The FW-H solver takes the acoustic pressures computed at the bounds of the analysis and propagates them through idealized, stationary air using a modified

version of the wave equation. To accurately predict acoustic pressures at the boundary, freestream boundaries were used in place of the wind tunnel walls. The freestream boundary condition applies a tangential (downstream) velocity to flow at the boundary and allows for pressure and velocity fluctuations normal to the boundary face.

The pressure fluctuation equation can be used in an unsteady analysis to determine if elements, interfaces, or boundaries are creating un-physical acoustic results. Pressure fluctuations are determined by subtracting the mean pressure in an unsteady simulation from the instantaneous pressure, as shown in

$$p' = p(t) - p_{mean}. \tag{2.3}$$

Pressure at a point outside of the computational region is calculated using

$$p'(\mathbf{x}, t) = p'_T(\mathbf{x}, t) + p'_L(\mathbf{x}, t) + p'_Q(\mathbf{x}, t), \tag{2.4}$$

in the FW-H formulation. This pressure represents the summation of pressure due to monopole, $p'_T(\mathbf{x}, t)$, dipole, $p'_L(\mathbf{x}, t)$, and quadrupole, $p'_Q(\mathbf{x}, t)$ terms

$$p'_T(\mathbf{x}, t) = \frac{1}{4\pi}\left(\left(\frac{\partial}{\partial t}\right)\int_S \left[\frac{Q}{(r(1-M_r))}\right]_{ret} dS\right), \tag{2.5}$$

$$p'_L(\mathbf{x}, t) = \frac{1}{4\pi}\left(\left(-\frac{\partial}{\partial x_i}\right)\int_S \left[\frac{L_i}{(r(1-M_r))}\right]_{ret} dS\right), \tag{2.6}$$

$$p'_Q(\mathbf{x}, t) = \frac{1}{4\pi}\left(\left(\frac{\partial^2}{(\partial x_i)(\partial x_j)}\right)\int_V \left[\frac{T_{ij}}{(r(1-M_r))}\right]_{ret} dV\right). \tag{2.7}$$

Equations 2.5, 2.6, and 2.7 are the integral formulations for each of these terms.

Farrassat's Formulation 1A was selected as the FW-H formulation, since it is the preferred formulation for general subsonic source regions in Star-CCM+ [26]. In this formulation, the monopole and dipole terms are rewritten as thickness surface terms and loading surface terms,

as in

$$p'_T(\mathbf{x},t) = \frac{1}{4\pi}\left(\int_{(f=0)}\left[\frac{\rho_0(\dot{U}_n + U_{\dot{n}})}{r(1-M_r)^2}\right]_{ret} dS\right) + \\ + \frac{1}{4\pi}\left(\int_{(f=0)}\left[\frac{\rho_0 U_n[r\dot{M}_r + a_0(M_r - M^2)]}{r^2(1-M_r)^3}\right]_{ret} dS\right), \quad (2.8)$$

$$p'_L(\mathbf{x},t) = \frac{1}{4\pi}\left(\frac{1}{a_0}\cdot\int_{(f=0)}\left[\frac{\dot{L}_r}{r(1-M_r)^2}\right]_{ret} dS\right) + \\ + \frac{1}{4\pi}\left(\int_{(f=0)}\left[\frac{(L_r - L_M)}{r^2(1-M_r)^2}\right]_{ret} dS\right) + \\ + \frac{1}{4\pi}\left(\frac{1}{a_0}\cdot\int_{(f=0)}\left[\frac{L_r\left[r\dot{M}_r + a_0(M_r - M^2)\right]}{r^2(1-M_r)^3}\right]_{ret} dS\right). \quad (2.9)$$

Volume terms in the form of quadrupole sources $p'_Q(\mathbf{x},t)$ were not considered in this analysis primarily due to the inability to accurately mesh the wake off the trailing edge flap on the available hardware. An alternative method to consider volumetric terms using a fluid permeable surface that encircles all relevant noise sources exists [26]. For example, a cylindrical surface could be defined to encircle the slat, slat gap filler, leading edge of the main wing, and the recirculation vortex found behind the slat. FW-H analysis using the Farrassat 1A formulation on this surface would theoretically account for monopole, dipole, and quadrupole sources in the slat gap region. However, this method was not utilized because this permeable surface definition requires polyhedral elements instead of a hexahedral elements in Star-CCM+, and polyhedral elements were found to significantly reduce the accuracy of the simulation, especially in boundary regions. A polyhedral element domain mesh with a larger number of cells would most likely improve the flow in this region, so this method could be investigated in future works.

A freestream boundary condition does not perfectly simulate the wind tunnel setup which consists of 3-sided anechoic chambers covered by a glass fiber mesh in place of hard tunnel walls, as is shown in Fig. 2.13b. While the freestream boundary conditions behave similarly in that they

allow for flow fluctuations in the normal condition, they do not simulate any surface friction or turbulence caused by the glass fiber mesh surface. It is assumed in this analysis that flow structures generally do not cross these boundaries and that the freestream boundary surface is orthogonal to acoustic waves emitted by the wing.

The unsteady flow solver was executed for 0.115 seconds before acoustic data was recorded to allow time for the solution to stabilize. This stabilization time was approximated by multiplying the passthrough time for a particle moving at 35 m/s by two. To capture frequency sound waves for frequencies as low as 100 Hz, the FW-H solver was computed for 0.01 seconds following stabilization of the flow. Acoustic signal pruning was computed in the utilized FW-H formulation to ensure a complete noise sample is received at the receiver location.

This combined simulation resulted in a set of acoustic pressures in the time domain. These pressures were converted to the frequency domain using a Fast Fourier Transform (FFT) and converted to Sound Pressure Levels (SPL) in decibels using a reference pressure of 2E-5 pascals. The FFT was computed for a time period of 0.12 seconds to 0.129 seconds of simulation time, to account for signal pruning and transmission time to the acoustic receiver. Taking the root sum square of the pressures in the desired frequency domain and using the same reference value to convert to decibels results in the Overall Sound Pressure Level (OASPL), which characterizes the aeroacoustics of the wing with a single number. The OASPL result is scaled from the computational domain (which represents a characteristic unit span) to the experimental span using the scaling procedure in [29].

Sound Pressure Level in decibels is calculated for the i^{th} frequency band by taking the base 10 $\log$ of the summation of the squared root mean square sound pressure, p_{rms}^2, for each frequency band and normalizing by the reference pressure squared, p_{ref}^2, as in

$$SPL_i = 10 \cdot \log_{10} \left(\frac{\sum_i (p_{rms}^2)_i}{p_{ref}^2} \right). \tag{2.10}$$

Overall Sound Pressure Level in decibels is calculated by taking the base 10 $\log$ of the magnitude

of the root mean square pressure for the whole frequency range, p_{rms} normalized by the reference pressure, p_{ref}^2, which is written as

$$OASPL = 20 \cdot \log_{10}\left(\frac{p_{rms}}{p_{ref}}\right). \tag{2.11}$$

This is equivalent to taking the base 10 $\log$ of the root sum square of the pressure at each frequency band normalized by the reference pressure where the root sum square is $(\sum_i p_i^2)^{1/2}$ and P_i is given by

$$p_i = p_{ref} \cdot 10^{\frac{SPL_i}{20}}. \tag{2.12}$$

This equivalent formula[4] is written as

$$OASPL = 20 \cdot \log_{10}\left(\frac{(\sum_i p_i^2)^{1/2}}{p_{ref}}\right). \tag{2.13}$$

2.3.2.1 Comparability of the Computational Aeroacoustic Method and the Experimental Acoustic Method

In this work, it was assumed that the entire surface of the wing, slat, flap, and SGF were necessary to accurately determine noise using the described CAA surface method. However, it is possible it would be more accurate relative to experiments to only consider the bottom surfaces of the wing, slat, flap, and SGF as the microphone is positioned below the wing (along the direction of the negative y-axis), as is shown in Fig 2.15. In the experimental setting, the only method by which pressure waves originating on the far surface of the wing geometry propagate to the microphone is by diffusion around the wing or reflection from other surfaces. Additionally, limited amounts of noise propagate through the wing and SGF structures from the top to the bottom surface before transmitting through the air to the microphone. In the CAA formulation described herein, the only difference between noise sources on the top and bottom surfaces is a dot product between the normal velocity vector and the receiver distance vector incorporated into the L_i terms in Eq 2.9. The

[4]This second formulation is utilized to calculate OASPL for real microphone measurements for the experimental wind tunnel setup.

top and bottom surfaces of the wing are shown in Fig. 2.23 as red and blue surfaces, respectively.

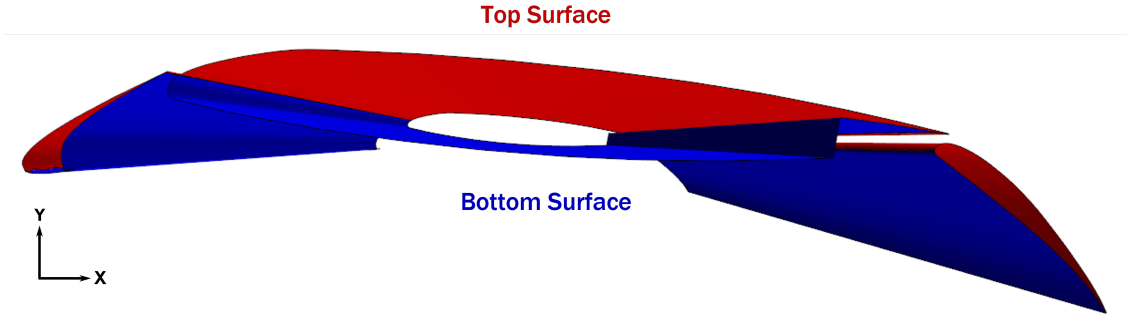

Figure 2.23: Top surface (red) and bottom surface (blue) used in the CAA noise source propagation comparison.

To determine the influence of far-surface noise sources on the CAA result, a test analysis was conducted using the same general procedure outlined previously. In this analysis, four microphone receivers were tested:

1. A microphone receiver in the standard location matching the experimental setup.
2. A microphone receiver mirrored across the xz-plane from the standard location.
3. A microphone receiver in the standard location only receiving propagated pressure data from the bottom surface of the wing.
4. A microphone receiver mirrored across the xz-plane from the standard location only receiving propagated pressure data from the bottom surface of the wing.

Together, these four microphones allowed for a determination of the influence of the top surface of the wing on the resulting noise at the microphone receiver. SPL versus frequency results for all four microphone receivers are shown in Fig. 2.24.

From the results presented in Fig. 2.24, a few conclusions can be reached. Most importantly, sound pressure level results obtained with the CAA method utilized herein do not change significantly if the microphone is located above the wing instead of below it. This suggests that, unlike as

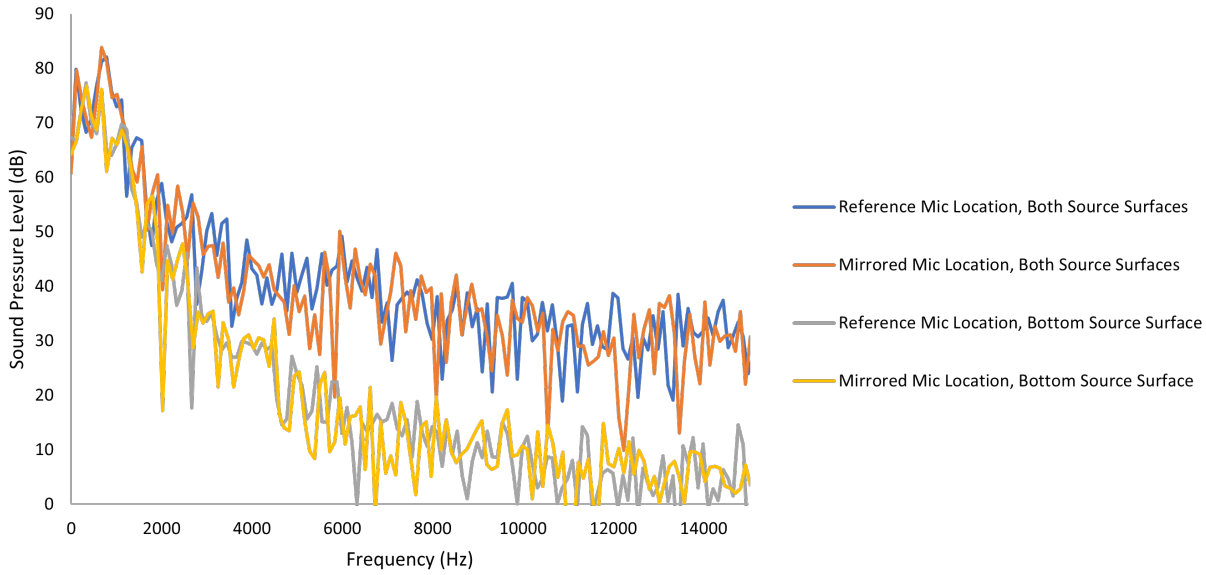

Figure 2.24: Sound Pressure Level in dB versus frequency in Hz. The reference microphone location corresponds to the standard microphone receiver location used in this work, while the mirrored microphone location refers to the microphone receiver positioned in a location mirrored over the xz-plane relative to the standard location. The bottom source surface results correspond to the microphone receivers that only considered noise sources on the bottom surface of the wing.

is predicted in the experimental setting, noise sources on the far-side surface of the wing do contribute to SPL results. However, the microphone receivers collecting pressures propagated from both surfaces of the wing receive a broadband noise level at around 40 dB SPL, which is similar to the broadband noise level found in experimental SPL results. Therefore, further testing and comparisons are required to determine if it is more useful to calculate sound pressure level at the microphone receiver using both surfaces of the wing or only the bottom surface of the wing.

2.4 Optimization Methods

While the structural analysis runtime of SGF configurations is on the order of a few minutes, the end goal of the design procedure is to include the noise metric resulting from aeroacoustic analyses in determining the best SGF designs. As described previously, the selected aeroacoustic analysis procedure is post-processing high-fidelity pressure results from unsteady, turbulent CFD facilitated by Star-CCM+. This analysis is significantly more time consuming, requiring runtimes

on the order of 12 hours 20-core processor. For this reason, evaluations of the objective function are extremely time consuming, ruling out many traditional optimization methods (e.g., gradient-based methods and many semi-random-searching heuristic methods). It is believed that an optimization method utilizing a surrogate model would overcome these runtime concerns without sacrificing accuracy in the resulting design. An efficient global optimization (EGO) scheme provides the ability to minimize objective function evaluations while determining the features of the global design space, avoiding local minimums. This algorithm functions by finding the maximum of the internal expected improvement function at each iteration. This function calculates the probability of a given new point improving the quality of the surrogate by considering distance to the current optimal point and the spread of the evaluated points. This surrogate-based method has the benefit of providing a mechanism of calculating the closeness of the optimal design to the true optimum through evaluation of the generated surrogates. The EGO algorithm implemented in this work is taken from the Surrogate Modeling Toolbox MATLAB library [30], and the EGO algorithm itself is based on the work of Jones et. al. [31].

EGO algorithms have been utilized and improved since the initial proposal of the expected improvement function by [31]. For example, a version of the EGO algorithm was utilized in a morphing structures framework by [32]. While a basic version of the algorithm is utilized in this work, research is ongoing to extend the algorithm to consider multiple objectives and constraints. An example of an extension of EGO to consider multiple objectives using a Pareto frontier framework was investigated in [33]. Finally, an alternative MATLAB toolbox called PlatEMO contains multiple recently developed versions of the EGO algorithm [34]. Continued investigation of the slat gap filler problem could be assisted by implementation of this toolbox in future works.

The EGO algorithm implemented here works by taking a set of input data points that are spread throughout the design space and creating an initial surrogate model of the hyperspace. Then, the algorithm seeks to alternatively evaluate points near the current best point (to find the minimum value) while exploring the areas in the bounded design variable hyperspace that are furthest from the points that have already been evaluated (to ensure that the minimum functional value is the

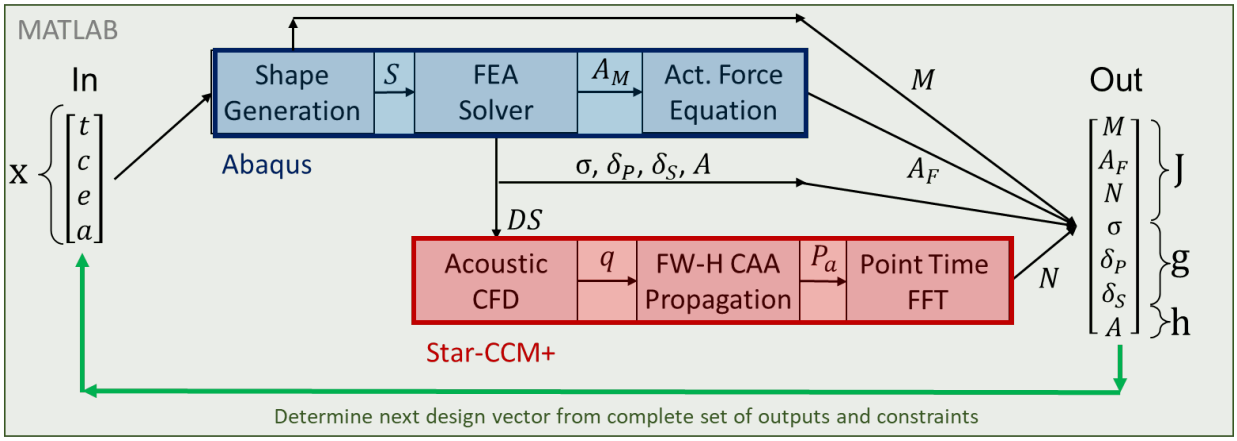

Figure 2.25: Optimization process carried out for each iteration of the EGO algorithm. The input and output vectors are managed by the algorithm in MATLAB, while intermediate inputs and outputs are managed by a combination of MATLAB, Abaqus, and Star-CCM+.

global minimum). The surrogate model available for use in this implementation was a first order linear exponential Kriging surrogate function [35]. To implement this algorithm, an objective cost function combining multiple objectives into a single "cost" for each design vector is required.

The optimization procedure was used both to execute a structurally based optimization of the SGF and to execute a combined structural and aeroacoustic optimization. Both optimizations utilized cost functions to condense the output variables to one number for the EGO toolbox. These cost functions are shown in

$$C = w_1 \cdot \frac{M}{n_1} + w_2 \cdot \frac{A_F}{n_2}, \tag{2.14}$$

and

$$C = w_1 \cdot \frac{M}{n_1} + w_2 \cdot \frac{A_F}{n_2} + w_3 \cdot \frac{N}{n_3}. \tag{2.15}$$

In these equations, w_i represents the relative weight applied to each output variable. The sum of the weights must equal one, and the weights were selected to emphasize certain outputs, for example noise, relative to other outputs. The output variables are normalized by a value n_i selected such that a desirable value of each output divided by n_i is approximately one.

The EGO algorithm implementation utilized provided no method to consider optimization con-

straints, so a penalty method was utilized. In this method, a multiplier was applied to the cost function if a constraint was violated. As a result of optimizer testing, this penalty multiplier was set to be two such that the surrogate function was not overly affected by penalized objective values. An over-penalized objective was found to prevent the optimizer from finding potential minimums in regions of the objective space close to constrained regions.

An image representing the software, inputs, and outputs utilized for each iteration of the optimizer configured for multiphysical analysis is shown in Fig. 2.25. For optimization considering only structural results, the Star-CCM+ processes boxed in red are skipped. In this figure, the vector of input variables, $\mathbf{x}$, are the design variables presented in Table 2.1. This vector is transmitted to Abaqus where the SGF configuration shape, S, is defined. An output of the shape generation process, combined with knowledge of SGF material density, is the mass, M, of the SGF configuration. The SGF shape is sent to the FEA solver along with loading and contact descriptions to determine a deformed shape, DS. A result of the FEA solution is the actuation moment, A_M, which is converted into an actuation force, A_F, as presented in Fig. 2.4. The deformed shape is exported using a universal format and imported to Star-CCM+ for fluid domain modification prior to CFD analysis. The results of the CFD analysis, indicated by q, are used as inputs to the CAA analysis for the FW-H algorithm. Following CAA analysis, acoustic pressures, P_a, are used in a point time fast Fourier transform (FFT). Integrating over the results of this FFT in the frequency domain results in a number for overall noise, N. Together, M, A_F, and N form the vector of output variables, $\mathbf{J}$. Note that, in this optimization procedure, the output vector is converted to a single objective cost value, C, using Eq. 2.15. Inequality constraints, labeled with the vector $\mathbf{g}$, are calculated using values representing maximum stress σ, displacement under pressure δ_P, and displacement when stowed δ_S[5]. Also, equality constraints, labeled with the vector $\mathbf{h}$, include a requirement for the SGF to remain attached to the slat when loaded, A.

The mathematical form of the optimization problem given these variable definitions is pre-

[5]Inequality constraints must be defined such that they are less than or equal to 0. Therefore, comparison values were subtracted from the output values for σ, δ_P, and δ_S. For the stress constraint, the maximum yield stress, σ_y was used. For the displacement constraints, a safety factor relative to the maximum thickness of the SGF, t_max, was used

sented as

$$\begin{aligned} \min_{\mathbf{x}} \quad & \mathbf{J}(\mathbf{x}) \\ & \mathbf{x_{lb}} \leq \mathbf{x} \leq \mathbf{x_{ub}} \\ \text{s.t.} \quad & \mathbf{g}(\mathbf{x}) \leq 0 \\ & \mathbf{h}(\mathbf{x}) = 1. \end{aligned} \tag{2.16}$$

In Eq. 2.16, the relevant vectors are defined as follows: The vector of design variables is

$$\mathbf{x} = \begin{bmatrix} t \\ c \\ e \\ a \end{bmatrix}. \tag{2.17}$$

The vector of output variables is

$$\mathbf{J} = \begin{bmatrix} M \\ A_F \\ N \end{bmatrix}. \tag{2.18}$$

The vector of inequality constraints is

$$\mathbf{g} = \begin{bmatrix} \sigma - \sigma_y \\ \delta_P - 2 \cdot t_{max} \\ \delta_S - 10 \cdot t_{max} \end{bmatrix}. \tag{2.19}$$

The vector of equality constraints is

$$\mathbf{h} = \begin{bmatrix} A \end{bmatrix}. \tag{2.20}$$

2.5 Mixed Reality CFD Visualization

A novel combination of Star-CCM+ CFD results, the Blender object editing toolbox, the Unity game development engine, and the Oculus Experimental Passthrough API was utilized to provide three-dimensional visualizations of CFD results in a real wind tunnel environment. Methodolo-

gies specific to mixed reality research are defined and discussed in detail in Chapter 5, while an overview of applied CFD methods are presented here.

Low fidelity Star-CCM+ aerodynamics simulations of a low speed wind tunnel environment were executed to minimize processing time on the display hardware. Directed meshes with fewer than 500,000 cells were used in the CFD simulations. A two dimensional slice of the directed mesh was tabulated and exported to provide localized flow field results for a particle spawning algorithm. For other visualizations, Star-CCM+ scenes were created, exported, converted to simulation objects, placed in the mixed reality scene, and displayed as virtual reality objects in the head mounted display (HMD).

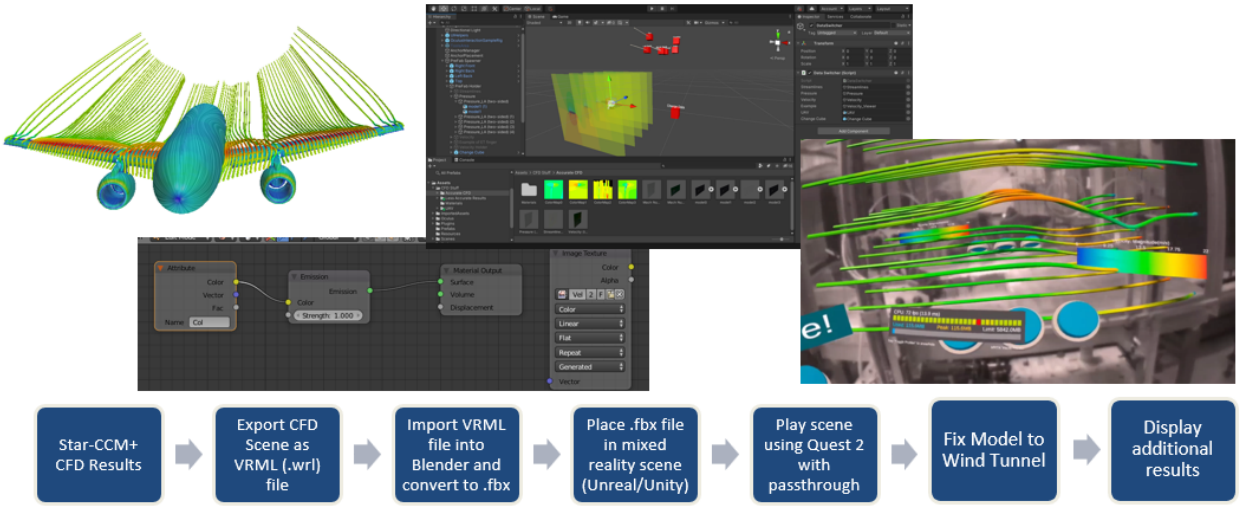

Figure 2.26: Computational process for creating mixed reality CFD scene.

The process for creating a mixed reality CFD visualization and displaying it in the desired facility can be broken down into three steps: first, the CFD simulation of the wind tunnel model is executed and the flow results are exported using a 3-dimensional file format. Second, the flow results are converted into a format that can be used in virtual reality development engines and imported to the simulated portion of the mixed reality scene. Finally, the mixed reality scene is programmed to utilize video pass-through around the flow-displaying objects and the scene is

oriented to align with the wind tunnel. Fig. 2.26 shows a flow chart detailing these steps.

CFD analysis was conducted using simplified flow and boundary conditions to simulate the flow state of the Texas A&M 4 ft. by 3 ft. cross section closed-loop low-speed wind tunnel shown in Fig. 2.13a. Specifically, the tunnel flow was simulated using steady, turbulent 3-dimensional flow with the Reynolds-Averaged Navier Stokes (RANS) solver in Star-CCM+. These settings are simplified relative to the settings used in the design and optimization procedure because it was determined that a lower fidelity CFD result would suffice for instructive visualization purposes. However, the same process could be replicated with higher fidelity, and more time consuming CFD simulation results.

These CFD simulations using were validated to precisely represent flow occurring in the wind tunnel by comparing lift coefficients between experimental results and simulated results. Lift coefficients are determined in the laboratory wind tunnel by post processing data from load cells mounted to the ends of the spar holding the test article. CFD lift coefficients are determined using a summation of pressure force on the surface of the modeled test article and normalizing with a reference area. Drag coefficients were not considered because:

- It is difficult to account for drag produced by experimental mounts (the spar holding the model) and by experimental surfaces (3D printed parts and actuator discontinuities).
- It is difficult to accurately compute drag in CFD using the low fidelity simulations required to limit maximum file-sizes and maintain a fast run time on available computational hardware.[6]

Table 2.6: Comparison of lift and drag coefficients between experimental and CFD results for both models analyzed.

	Section Spanning HL-CRM Wing			**UAV Model**	
	Wind Tunnel	CFD Solution		Wind Tunnel	CFD Solution
C_L	2.16	1.80	C_L	0.40	0.40
C_D	0.18	0.09	C_D	-0.05	0.08

[6]CFD simulations were executed using a 20 core Intel(R) Xeon(R) processor with a base speed of 2.20GHz and 64 GB of RAM

Experimental and simulated coefficients are compared in Table 2.6 for the test cases presented. As can be seen, the lift coefficients found in CFD were similar to those found in experiments while the drag coefficients were less comparable with a larger relative error between the analysis types. These results represent a lower fidelity CFD solution compared to the solution generated for the optimization procedure. However, the results in Table 2.6 still generally match experimental results, further validating the CFD analysis presented throughout this thesis.

3. Structural Design and Down-selection of SGF Concepts

The three SGF concepts were each structurally analyzed using the solver settings described in Chapter 2. The results of these design explorations are used to determine which SGF concept is the best candidate for optimization and experimental testing.

3.1 Design of Experiment for Each Concept

For all three design concepts, a 2 level, 4 variable, 8 experiment Taguchi Orthogonal Array was used to determine the input variables such that a fully balanced design space was explored. The Taguchi Table values are presented in Table 3.1. All concepts were analyzed for both load cases of the deploy-retract cycle and the deploy-stow cycle.

Generally, each DOE considered a design variable representing thickness, SGF start location, and SGF end location with respect to the main wing surface. Each design variable study also examined a fourth design variable unique to that SGF concept. The design explorations for each concept are slightly different such that they both accurately describe the design space for that SGF concept and exploit the unique qualities of the examined SGF.

For each design study, the bounds on each design variable were determined by a combination of physical limitations and simulation restrictions. SGF thickness was limited to values between 0.05 mm and 0.10 mm because these are the lower and upper limits of manufacturability for SMA sheets according to previous work. The upper attachment point for a SGF was limited to be lower than the point at which the retracted slat connects with the main wing such that no discontinuities are presented to the flow during cruise. For all three SGF concepts, this attachment point was moved closer to the tip of the wing because design exploration showed that long SGF configurations provide little acoustic benefit and always increased mass. The lower bound of the attachment point and the upper bound of the SGF end point, which determines SGF length, were set to ensure the resulting SGF had sufficient length to maintain contact with the fully deployed slat under a pressure load. The lower bound of the SGF end point was determined by the point at which the structural

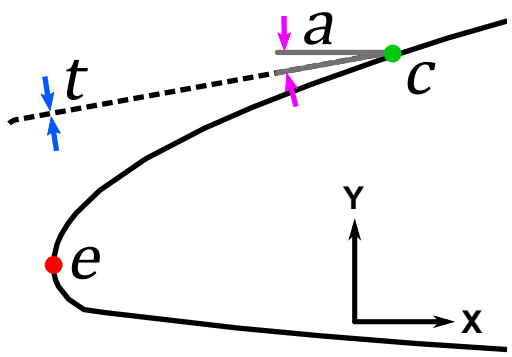

(a) Locations of the thickness, t, connection point, c, end point, e, and attachment angle, a, design variables for the WFMS SGF concept.

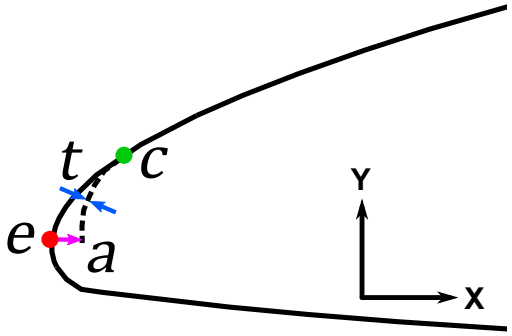

(b) Locations of the thickness, t, connection point, c, end point, e, and overwrap coefficient, a, design variables for the WFAS SGF concept.

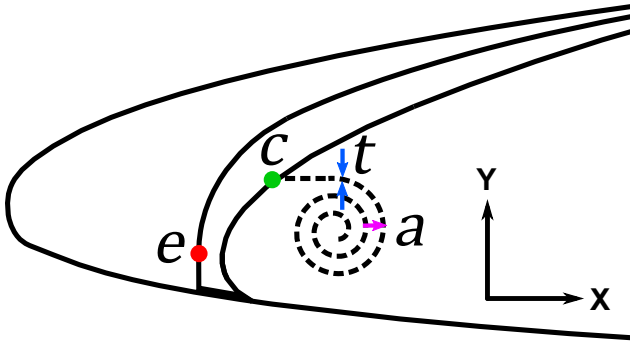

(c) Locations of the thickness, t, wing point, c, slat point, e, and pitch coefficient, a, design variables for the ICAS SGF concept.

Figure 3.1: Reprint of Figs. 2.2a, 2.2b, and 2.2c for reference in this chapter

.

Table 3.1: Two level four variable eight configuration Taguchi Table utilized for design of experiment studies. Design variables (DVs) range from a normalized lower bound, 0, to a normalized upper bound, 1.

Configuration	DV 1	DV 2	DV 3	DV 4
1	0	0	0	0
2	0	0	0	1
3	0	1	1	0
4	0	1	1	1
5	1	0	1	0
6	1	0	1	1
7	1	1	0	0
8	1	1	0	1

solver would complete its analysis. It is believed that the solver has difficulties solving the contact algorithm for regions with large local curvature, as is the case for the leading edge of the main wing. These solver difficulties created a lower limit for the SGF end point, and determined a maximum SGF length.

The output variables for all three DOE studies were mass and actuation force. For the DOE studies, all constraints were calculated and monitored but no design output variables were penalized if a configuration violated any constraint. All three DOE studies considered constraints on maximum von-Mises stress. For the auto stowing SGF concepts, a displacement constraint checking for complete stowing against the surface of the main wing was implemented. This constraint was not required for the WFMS SGF because the mechanical stowing was specified as a boundary condition, meaning that the solver would fail if the WFMS SGF did not stow. Similarly, a constraint stipulating that the SGF stay attached to the slat under the pressure load was not required for any of the three DOE studies because the structural solver would fail if the SGF detached from the slat. A final constraint considering displacement of the SGF under the pressure load was implemented.

For each DOE study, the results are primarily presented with main effects plots showing the important design trends. Additionally, the best design found by each study according the cost

Table 3.2: Design variables and bounds for the WFMS SGF DOE study.

Design Variable (Units)	Symbol	Lower Bound	Upper Bound
Thickness (mm)	t	0.05	0.10
Connection Point (mm)	c	-15.0	-8.0
End Point (mm)	e	-22.5	-21.0
Attach Angle ($^\circ$)	a	0.0	8.0

function used in the optimization study is pictured in its assembled, loaded, and stowed states. Only stress contours are shown because none of the best configurations transformed into martensite. It is believed this lack of transformation was caused by a low pressure load and a decision to not consider constraints when determining the best DOE configuration.

3.1.1 Wing Fixed Mechanism Stowed SGF Design of Experiment

The bounds for the Wing Fixed Mechanism Stowed (WFMS) SGF DOE were determined by a combination of manual design exploration and a preliminary design study. For more information regarding the preliminary design study, see Appendix 7. An image of depicting the parameterization of the WFMS SGF to a given set of design variables is shown in Fig. 2.2a.

The bounds used for each design variable are shown in Table 3.2. The fourth design variable refers to the angle at which the SGF is attached to the wing. The angle is defined in the counterclockwise direction from the negative x-axis in Fig. 2.2a, with a 0° angle defining a horizontal SGF. The results of the WFMS SGF DOE are tabulated in Table 3.3 and the main effects of each design variable compared to the output variables are shown in the Fig. 3.2a and Fig. 3.2b.

The main effects plots for the WFMS SGF show that all design variables considered are of similar importance. The attachment angle variable, as could be expected, appears to have very little impact on the mass of the SGF structure. However, it has a clear inverse relationship with the actuation force output suggesting that a greater angle, which corresponds to a downward pointing SGF, may result in less necessitated actuation force. The thickness design variable clearly has a large impact on both measured outputs. It is the only design variable out of the four that appears to

Table 3.3: Results from the DOE study for the WFMS SGF concept. Configurations were generated using the Taguchi table, Table 3.1. Mass, Actuation Force, and Cost outputs are presented, with cost being defined by the fitness equation used in structural optimization, Eq. 4.1. The bolded configuration is the best configuration found in this study.

	t (mm)	c (mm)	e (mm)	a (°)	M (g)	A_F (N)	C
1	0.05	-10.0	-21.0	0.0	0.007	0.0008	1.08
2	0.05	-10.0	-21.0	8.0	0.007	0.0005	1.07
3	0.05	-15.0	-22.5	0.0	0.004	0.0061	0.69
4	**0.05**	**-15.0**	**-22.5**	**8.0**	**0.004**	**0.0042**	**0.66**
5	0.10	-10.0	-22.5	0.0	0.016	0.0077	2.54
6	0.10	-10.0	-22.5	8.0	0.016	0.0042	2.49
7	0.10	-15.0	-21.0	0.0	0.007	0.0353	1.52
8	0.10	-15.0	-21.0	8.0	0.007	0.0246	1.38

have a similar type of relationship with both output variables. For both mass and actuation force, low thickness results in minimal output values. However, it is believed that thickness could be an important design variable for the unconsidered noise output variable, so it is not set to a minimum value. The connection point design variable most directly determines the length of the SGF in the WFMS concept. A proportional relationship between length and mass and an inverse relationship between length and actuation force matches intuition. The opposite behavior is observed for the end point design variable. This behavior is expected, since the opposite relationship to length exists for this design variable as it does for the connection point variable. It is possible that a lower end point has a relationship to a higher actuation force due to the nonlinear curvature of the slat bottom surface, resulting in a smaller slope for this plot compared to the slope of the connection point plot.

Stress contour results for the best WFMS SGF configuration according to the structural optimization cost function are shown in the assembled state in Fig. 3.3a, in the loaded state in Fig. 3.3b, and in the stowed state in Fig. 3.3c. These figures show that the largest stresses occur near the wing-side boundary condition in the stowing step of this analysis. This configuration is nearly stress free in the deployed state, as is the intention of this SGF concept. The side view shows that this WFMS SGF does not deflect much under an applied pressure load and that it retracts to a curve that is similar to the curve of the main wing but not exactly the same. This type of retraction would sat-

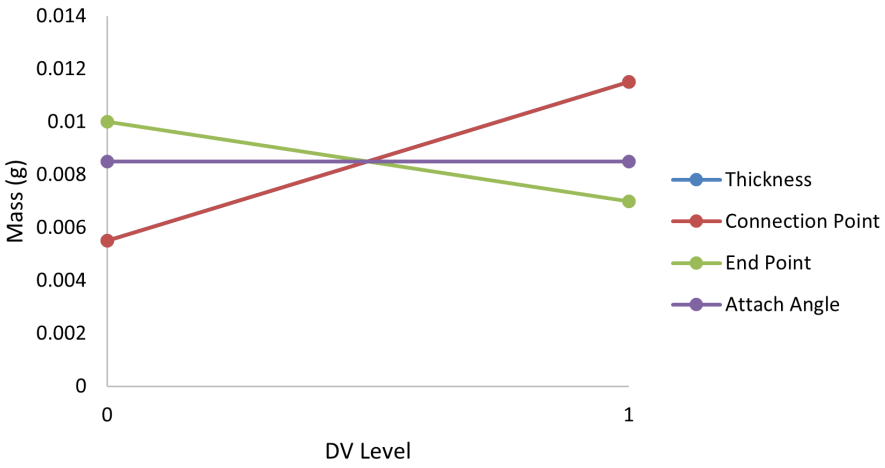

(a) Mass main effects plots.

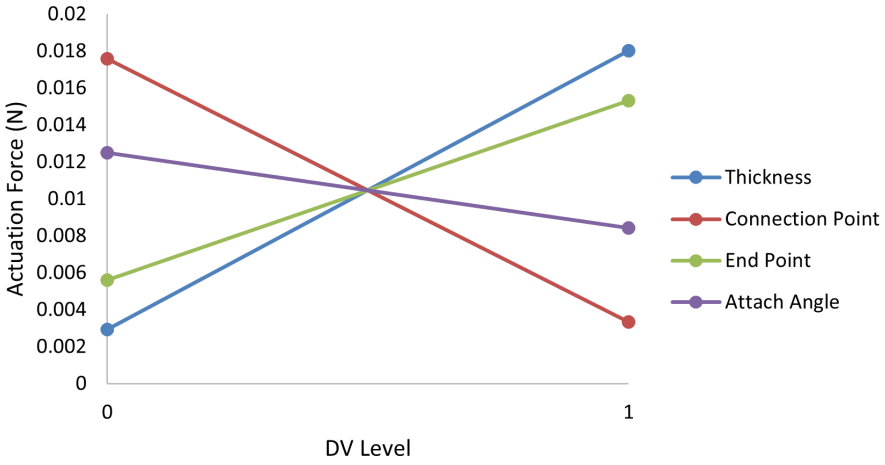

(b) Actuation force main effects plots.

Figure 3.2: Main effects plots for 8 configurations of the WFMS SGF concept representing a balanced observation of the design space.

isfy constraints but could be problematic in aerodynamic analysis. Finally, the maximum stress observed around 216 MPa was not large enough to trigger the material to begin transforming into martensite.

3.1.2 Wing Fixed Auto Stowed SGF Design of Experiment

The wing fixed auto stowed (WFAS) SGF design space was explored in a similar procedure to that of the WFMS SGF concept. The four design variables considered were thickness, con-

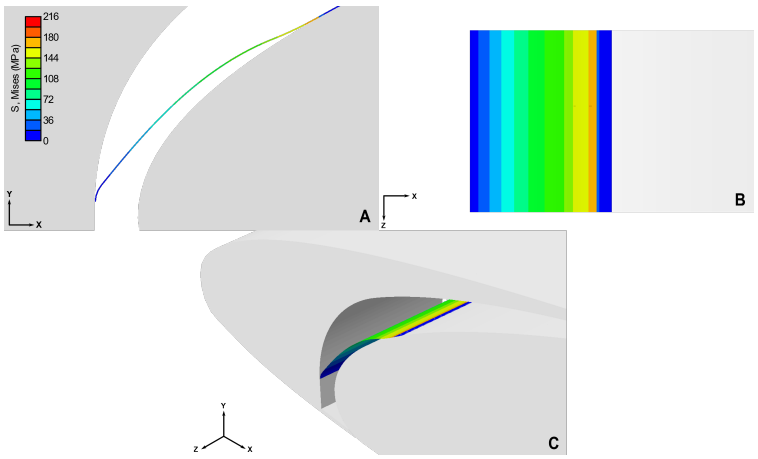

(a) Assembled state of the best WFMS SGF configuration.

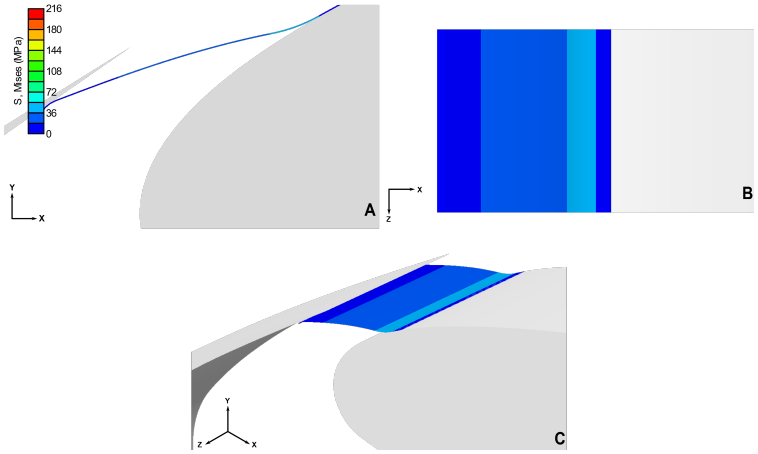

(b) Pressure loaded state of the best WFMS SGF configuration.

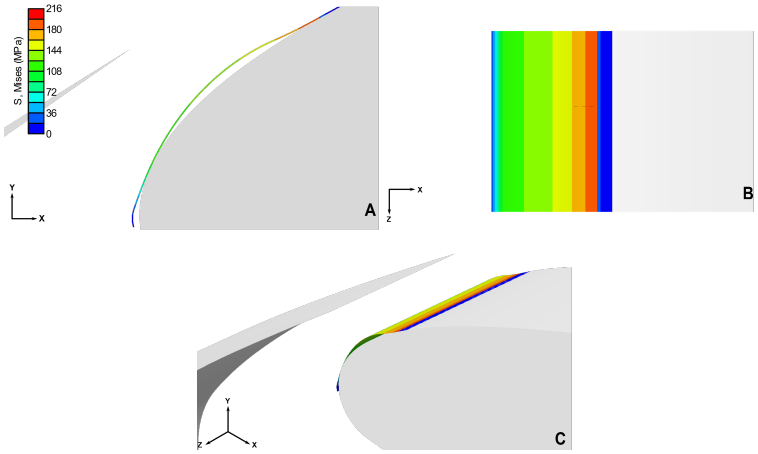

(c) Stowed state of the best WFMS SGF configuration.

Figure 3.3: Assembled, deployed, and stowed states of the best WFMS SGF configuration found in the DOE study.

Table 3.4: Design variables and bounds for the WFAS SGF DOE study.

Design Variable (Units)	Symbol	Lower Bound	Upper Bound
Thickness (mm)	t	0.05	0.10
Connection Point (mm)	c	-65.0	-60.0
End Point (mm)	e	-22.25	-21.50
Overwrap Coefficient	a	0.10	0.12

Table 3.5: Results from the DOE study for the WFAS SGF concept. Configurations were generated using the Table 3.1. Mass, Actuation Force, and Cost outputs are presented, with Cost being defined Eq. 4.1. The bolded configuration is the best configuration found in this study.

	t (mm)	c (mm)	e (mm)	a (°)	M (g)	A_F (N)	C
1	0.05	-60.0	-21.50	0.10	0.004	0.036	1.08
2	**0.05**	**-60.0**	**-21.50**	**0.12**	**0.004**	**0.034**	**1.05**
3	0.05	-65.0	-22.25	0.10	0.002	0.17	2.57
4	0.05	-65.0	-22.25	0.12	0.003	0.16	2.54
5	0.10	-60.0	-22.25	0.10	0.008	0.29	4.93
6	0.10	-60.0	-22.25	0.12	0.009	0.26	4.71
7	0.10	-65.0	-21.50	0.10	0.005	1.73	22.96
8	0.10	-65.0	-21.50	0.12	0.005	1.53	20.42

nection point, end point, and overwrap coefficient, and these are illustrated on an example result in Fig. 2.2b. Their bounds are presented in Table 3.4. The overwrap coefficient, a, is defined in Eq. 2.1.

The results of the Wing Fixed Auto Stowed SGF DOE study are presented in Table 3.5, and as main effects plots in Fig. 3.4a and Fig. 3.4b. As can be seen from Fig. 3.4a, the effects of changing each design variable on the mass are intuitive, since each design variable is geometric. The connection point design variable is the most influential in determining configuration length. Perhaps the key result from this analysis is that moving towards the upper bound for the connection point, which increases the mass, decreases the actuation force. This represents a coupling between a short SGF design and the actuation force that is not intuitive. The opposite trend is shown for the end point design variable, which also determines configuration length. However, the end point

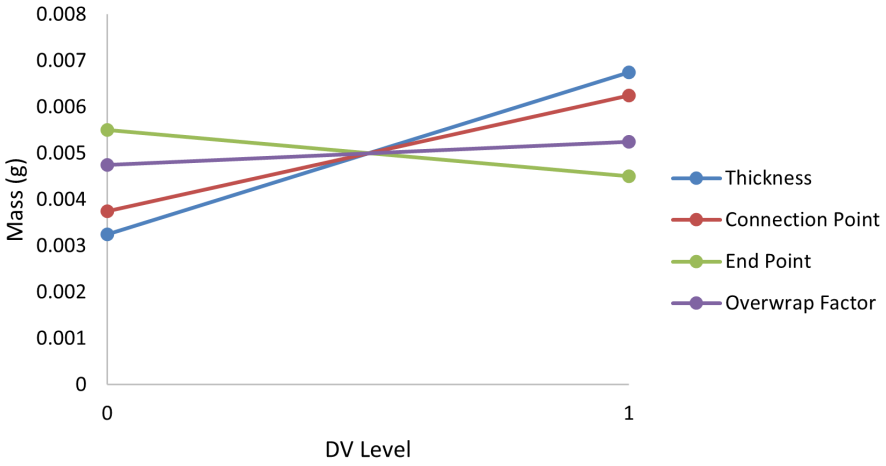

(a) Mass main effects plots.

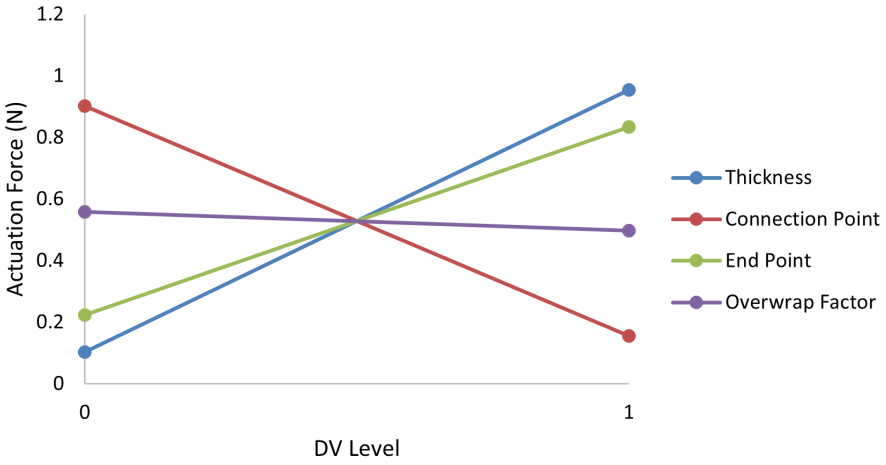

(b) Actuation Force main effects plots.

Figure 3.4: Main effects plots for 8 configurations of the WFAS SGF concept representing a balanced exploration of the design space.

design variable also determines the radius of curvature of the tip of the configuration, since it must match the curvature of the main wing at this point. This suggests that a small radius of curvature results in a SGF configuration that is more difficult to assemble and deploy.

Images of stress contours on the best WFAS SGF DOE configuration are shown in Figs. 3.5a, 3.5b, and 3.5c. These images show that the largest stresses observed in this configuration occur in the deployed SGF when pressure loads are applied, and that the smallest stresses occur in the

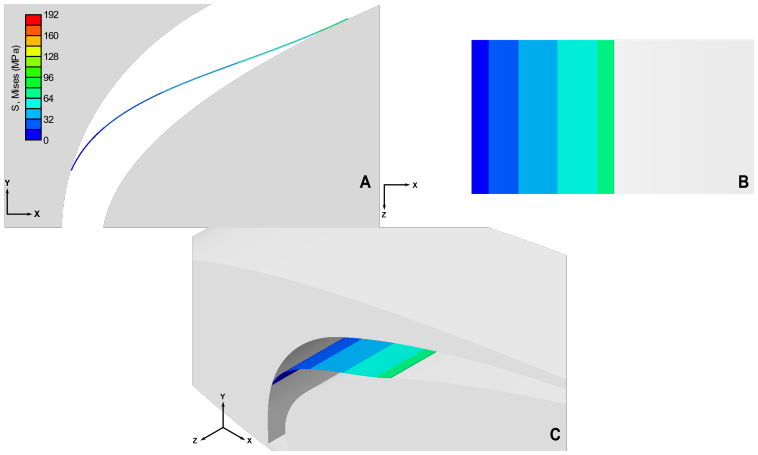

(a) Assembled state of the best WFAS SGF configuration.

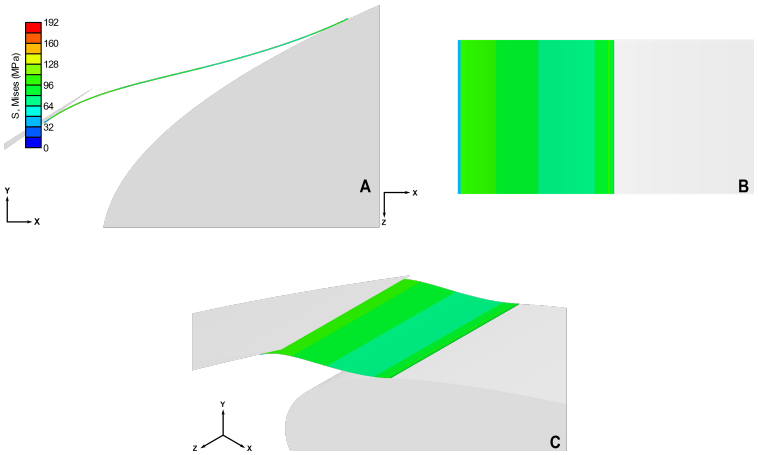

(b) Pressure loaded state of the best WFAS SGF configuration.

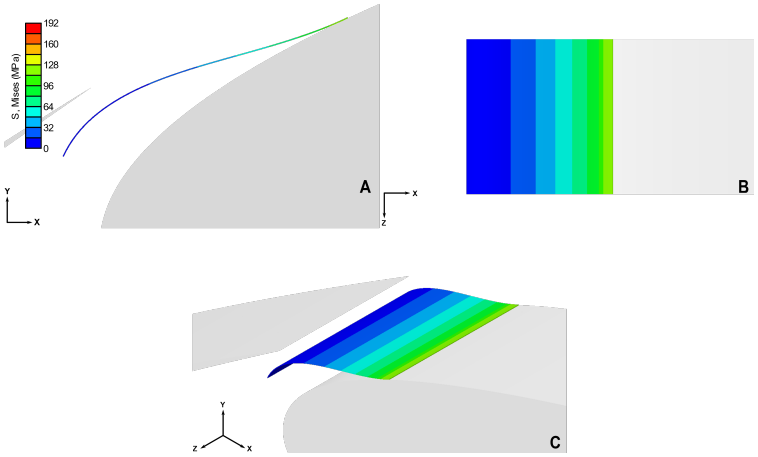

(c) Stowed state of the best WFAS SGF configuration.

Figure 3.5: Assembled, deployed, and stowed states of the best WFAS SGF configuration found in the DOE study.

assembled state. However, even these small stresses are significantly larger than the nearly stress free deployed state of a WFMS SGF. This is because stress must be in a WFAS SGF at all times such that it has the capability to automatically stow when it is released from contact with the slat.

As can be seen most clearly in Fig. 3.5cA, this WFAS configuration does not completely stow after the slat contact interaction is released. However, this configuration does not rely on a contact force from the slat to retract; rather it appears to float in a balance of forces between the pressure load and the geometric stowing force. Since the stowing analysis step is an implicit dynamic step, this type of response results in an oscillation of the structure between a position close to the main wing and a position close to the slat. It is unclear if this oscillation would eventually result in a more stowed position as it is slowly damped over time. Regardless, this image illustrates the need for implementation of the stowing constraint, since an SGF positioned like this configuration would violate assumptions about the pressure field.

3.1.3 Interior Coil Auto Stowed SGF Design Exploration

The Interior Coil Auto Stowed (ICAS) SGF concept is slightly different from the other two concepts in that geometric configurations were defined as a Archimedean spiral and assembled from an initial state fully on the interior of the main wing surface. The spiral geometries were conceptualized specifically to demonstrate and utilize the superelastic properties of SMAs, achieving large strains as the structure deploys, retracts, and stows. These nonlinear deformations were found to result in significant solver problems. ICAS SGF configurations were found to be the most computationally demanding and the most likely to cause a solver failure during structural analysis.

The complexities inherent in stowing a fully deployed ICAS SGF necessitate an implicit, dynamic simulation step. In this stowing step, a spring-like SGF is released at one end and allowed to fluctuate under simulated pressure loads while bouncing off various contact surfaces as the SGF returns to its original spiral geometry. This simulation step is more computationally intensive than all other simulation steps combined. Therefore, the capability to simulate the stowing step is demonstrated but not utilized in the DOE study for this SGF concept.

The design variables considered in this DOE study were thickness, wing exit point, slat at-

Table 3.6: Design variables and bounds for the ICAS SGF DOE study.

Design Variable (Units)	Symbol	Lower Bound	Upper Bound
Thickness (mm)	t	0.05	0.10
Wing Point (mm)	c	-16.0	-12.0
Slat Point (mm)	e	-21.5	-12.5
Pitch Coefficient	a	0.5	1.2

Table 3.7: Results from the DOE study for the ICAS SGF concept. Configurations were generated using the Taguchi table. Mass, Actuation Force, and cost outputs are presented, with cost being defined by the fitness equation used in structural optimization. The bolded configuration is the best configuration found in this study.

	t (mm)	c (mm)	e (mm)	a (°)	M (g)	A_F (N)	C
1	0.05	-12.0	-12.5	0.5	0.036	0.11	6.94
2	**0.05**	**-12.0**	**-12.5**	**1.2**	**0.035**	**0.06**	**6.12**
3	0.05	-16.0	-21.5	0.5	0.036	0.12	7.12
4	0.05	-16.0	-21.5	1.2	0.035	0.06	6.17
5	0.10	-12.0	-21.5	0.5	0.073	0.18	13.46
6	0.10	-12.0	-21.5	1.2	0.071	0.53	17.65
7	0.10	-16.0	-12.5	0.5	0.073	0.68	19.93
8	0.10	-16.0	-12.5	1.2	0.071	0.26	14.21

tachment point, and spiral angle. The wing exit point and slat attachment point design variables together defined a configuration length, which was required to be sufficiently long to fill the slat gap. These design variables mirror the function of the connection point and end point design variables in the Wing Fixed SGF concepts. The fourth design variable considered in this DOE was the pitch of the SGF spiral geometry. The pitch, a, of an Archimedean spiral defines the distance between each spiral loop, as in Equation 2.2. The bounds on these design variables are presented in Table 3.6, and example bounds for an ICAS SGF configuration are shown in Fig. 2.2c.

Results from the ICAS SGF DOE are presented in Table 3.7. Mass and actuation force main effects plots are shown in Fig. 3.6a and Fig. 3.6b, respectively. These results show that thickness is much more important than the other design variables for mass and actuation force. The fixed

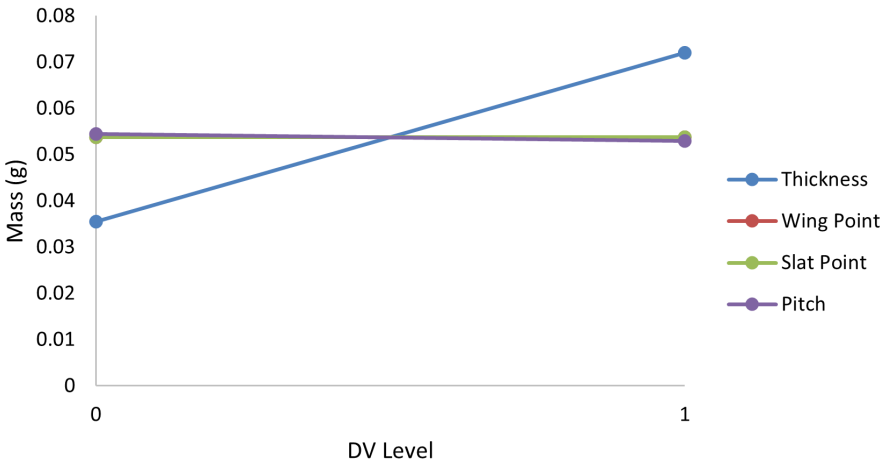

(a) Mass main effects plots.

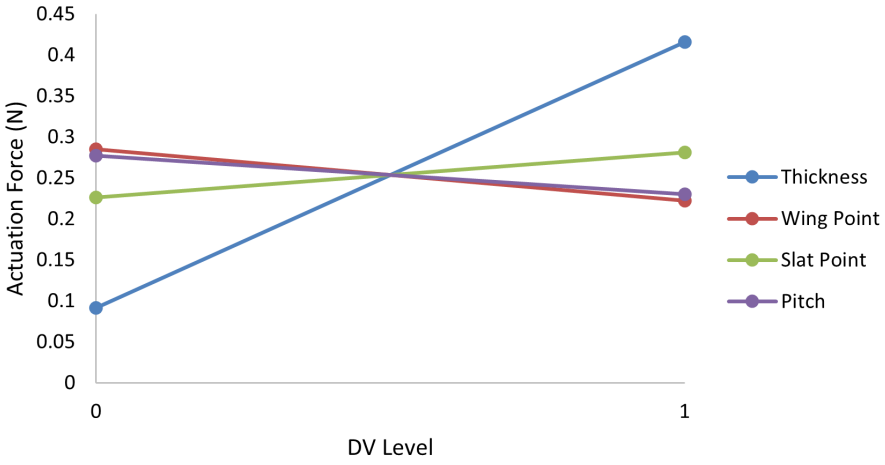

(b) Actuation Force main effects plots.

Figure 3.6: Main effects plots for 8 balanced configurations of the ICAS SGF concept.

slat-end of ICAS SGF configurations removes any dependence on thickness for satisfying pressure load related constraints. Furthermore, the lack of a stowing step and related constraints in this analysis seems to result in lighter configurations.

Interestingly, the pitch design variable appears to have an inverse relationship with actuation force. In geometric terms, a high pitch corresponds to an ICAS SGF configuration with larger outer diameters. This suggests that a relatively larger spiral structure is less stressed when it is deployed compared to a smaller spiral structure, resulting in a lower actuation force. All ICAS

SGF configurations have a significantly greater mass than any tested configuration from the other concepts, resulting in generally larger cost function values compared to the other concepts.

FEA stress contour results for the best configuration found in the ICAS SGF DOE are shown in Figs. 3.7a, 3.7b, and 3.7c. Unlike the similar figures for the other two concepts, the third ICAS SGF result figure is of the retracted state instead of the stowed state. These images reveal that, even at the lower bound of the slat point design variable, which corresponds to the highest position on the slat, there is much more SGF surface area exposed to flow compared to the surface area in other concepts. Also, the largest stress observed, near the fixed boundary condition during the deployed pressure load state, is nearly double the maximum stress observed in the best configuration results from the other two SGF concepts. However, these images demonstrate that the ICAS SGF concept can be structurally analyzed. Furthermore, this concept could be considered in future studies if it is determined that the high stresses and mass are acceptable drawbacks in exchange for increased stowing force.

3.1.4 DOE Trend Comparison

After examining the results of the three design of experiment studies, a few trends became clear. First, the interior coil auto stowed concept, while interesting to study, is incredibly difficult to design in a way that can compete with the other two concepts using the outlined metrics. The coil geometry results in a significant structural mass that does not serve any purpose once the SGF is deployed. Also, the reaction forces required for the slat to move this mass are much larger than the actuation forces for either of the other SGF concepts. If the applied pressure load was higher, this concept might become useful as its large strains provide a greater stowing force compared to the other concepts which would allow the ICAS concept to stow under harsher conditions. However, most WFMS and WFAS configurations that satisfy constraints related to the pressure constraints (staying attached to the slat under pressure and stowing under pressure). In addition to these problems, the ICAS concept requires the largest modifications to the existing wing geometry to implement and would be difficult to test at experimental scales. In terms of practicality for optimization studies, ICAS configurations require around two orders of magnitude more computational

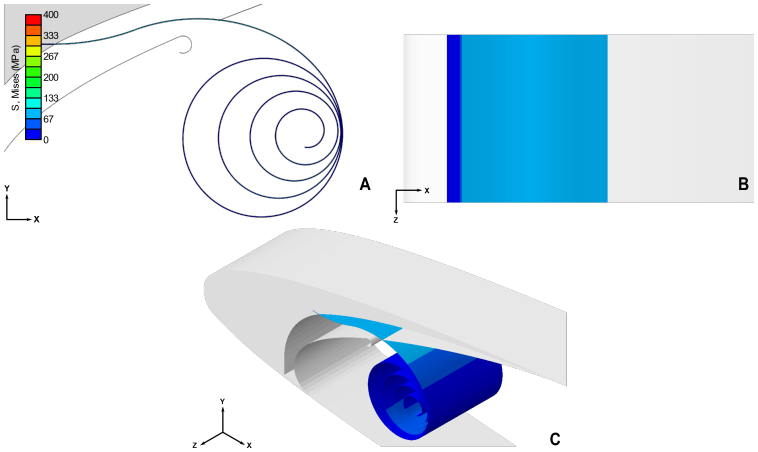

(a) Assembled state of the best ICAS SGF configuration.

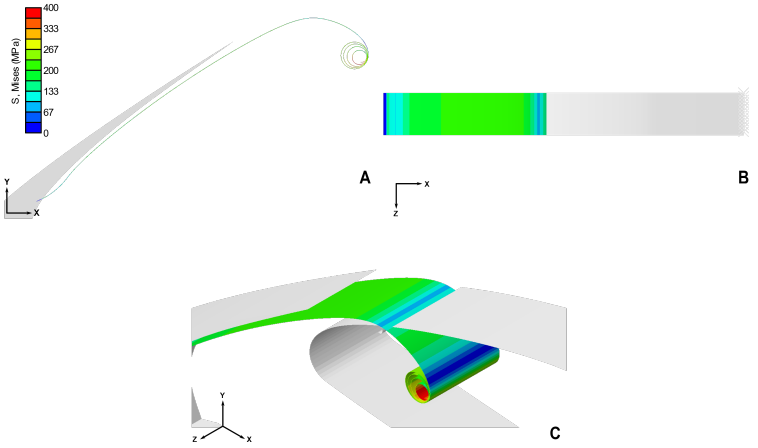

(b) Pressure loaded state of the best ICAS SGF configuration.

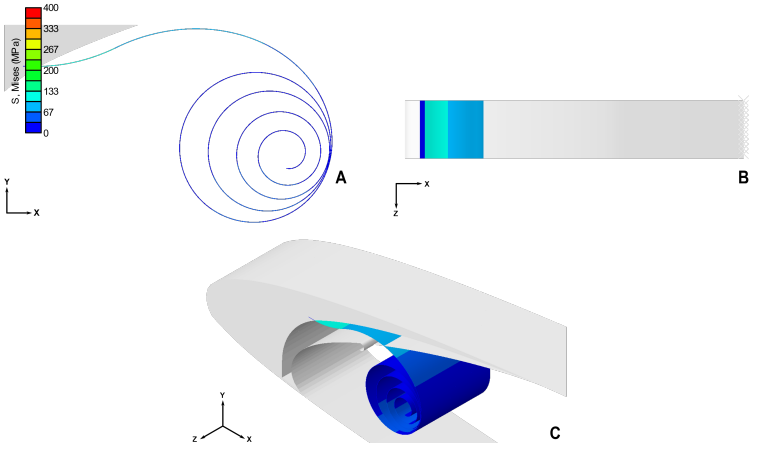

(c) Retracted state of the best ICAS SGF configuration.

Figure 3.7: Assembled, deployed, and retracted states of the best configuration of the ICAS SGF DOE.

runtime to simulate, which makes further design studies and optimization studies difficult.

The comparison between the wing fixed mechanism stowed and wing fixed auto stowed SGF concepts is more nuanced. Both concepts had similarly sized design spaces in which a multitude of potential configurations were found. Neither design was more or less likely to violate constraints compared to the other, since both DOE studies found a similar range of maximum von Mises stresses and displacements under the aerodynamic pressure load in the studied configurations. As is shown in Fig. 3.8b, all WFMS SGF configurations require a very low actuation force compared to the WFAS configurations. This is likely caused by the difference in slat attachment method – with the WFMS configurations only requiring a no-penetration contact force to be applied while the WFAS configurations required the slat to hold them in the deployed state. Conversely, the smaller structural geometry required for the WFAS SGF configurations meant that they were largely lighter than the WFMS configurations, as is shown in Fig. 3.8a.

The key design space feature in determining which design to optimize was the spread of actuation forces found in the WFAS design study. While the average actuation force for the studied WFAS configurations was significantly greater than the average actuation forces found in the WFMS design study, the lower bound of actuation force in the WFAS design study was similar to the range actuation forces found in the WFMS design study, as can be seen in Fig. 3.8b. Therefore, it is likely that an effectively implemented optimizer could drive the actuation forces towards this lower bound, while maintaining the mass savings inherent in the WFAS concept. For these reasons, the WFAS concept was selected for further investigation and optimization.

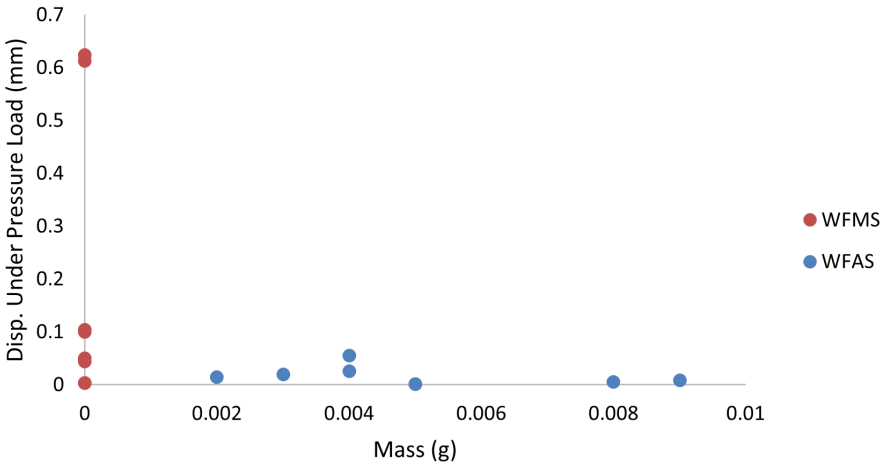

(a) Displacement under pressure load in millimeters plotted against mass in grams for the WFMS and WFAS SGF concepts.

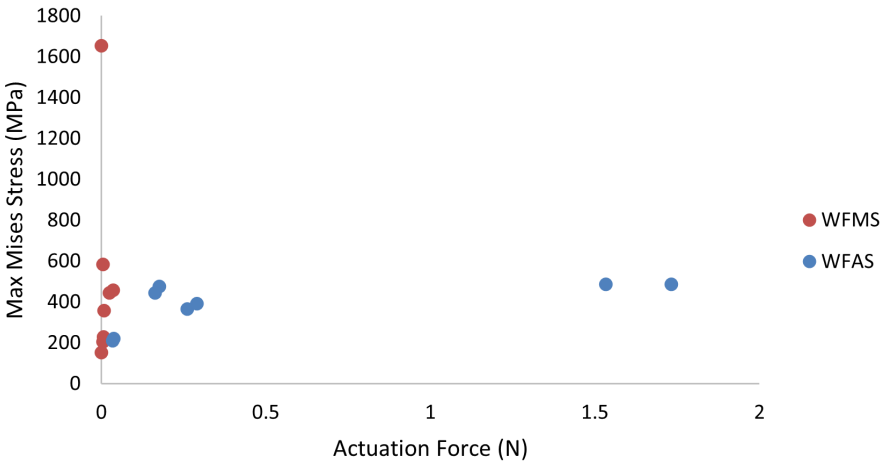

(b) Mises stress in megapascals plotted against actuation force in newtons for the WFMS and WFAS SGF concepts.

Figure 3.8: Comparison of the numeric output variables and constraints for the WFMS and WFAS SGF concepts.

4. Optimization

Three optimization procedures were undertaken to study the Wing Fixed Auto Stowed (WFAS) SGF concept. First, an optimization considering only structural objectives was executed, based on the results of the design of experiment studies. Then, two optimizations additionally considering the acoustic objective were completed. The bounds, constraints, and cost function used in these optimizations were modified in accordance with results from the structural optimization.

The mathematical form of the full optimization problem is presented in Equation 2.16, where $\mathbf{x}$ represents the design variable vector, presented in Equation 2.17, $\mathbf{J}$ represents the vector of output variables, listed in Equation 2.18. For this optimization procedure, the vector of output variables is converted to a single objective using an objective cost function, denoted by C.

The variables $\mathbf{g}$ and $\mathbf{h}$ represent the inequality and equality constraint vectors, respectively. The constraints are listed in Equations 2.19 and 2.20. For these constraints, the value for yield stress of an SMA, σ_y was assumed to be 800 MPa, and the maximum thickness, t_{max}, of an SGF was assumed to be 0.1 mm, as discussed in Chapter 3. The equality constraint, A refers to the constraint requiring the SGF to stay attached to the slat when the SGF is loaded.

4.1 Structural Objective Optimization

First, an optimization using the structural solver only was executed. This optimization procedure selected a design vector using the efficient global optimization (EGO) code and then executed an Abaqus run for the input design vector. The function running Abaqus returned an output file that was parsed and interpreted by the EGO code for the objectives and constraints. The objective was to minimize a cost function with mass and actuation force weighted equally. This optimization implemented constraints that the SGF must stow, must not deform significantly when it is deployed, and must not plastically deform. The algorithm was executed using a spacefilling latin hypersquare (LHS) method to determine input designs that created the initial Kriging surrogate model. Then, the optimization was executed for a number of unique design vectors, at which point

it was determined that the algorithm found a design sufficiently close to the global minimum.

This optimization procedure was evaluated 13 times as small improvements were made to the optimizer and Abaqus code. Results from one of the early successful optimization analyses were selected as normalizing values for the objective function to ensure that the two objectives considered were equivalently affecting the combined cost objective. The objective cost function is presented in Equation 2.14 where C represents the objective cost, w_1 is the weight applied to the mass objective, M, n_1 is the value used to normalize the mass objective given in grams, and n_2 is the value used to normalize the actuation force objective, A_F given in Newtons. The numerical values used for the structural optimizations are presented in Equation 4.1

$$C = 0.5\frac{M}{0.0033\ \mathrm{g}} + 0.5\frac{A_F}{0.0038\ \mathrm{N}}. \tag{4.1}$$

The best optimization analysis results are presented below. This optimization incorporated a key edit to the structural solver by not considering actuation forces calculated during the pre-deployment assembly steps, resulting in lower values of the cost function. This optimization was executed using 10 spacefilling points to determine the initial surrogate and 20 optimization points over which the EGO algorithm determined the points according to a balance between exploring the design space and finding a minimum objective value.

A plot showing the change in the objective function value compared to iteration number for the best structural optimization is shown in Fig. 4.1. This plot shows that, after the 10 iteration spacefilling procedure is complete, the algorithm quickly determines the area in the design space where it is most likely to find a minimum and searches this area, before exploring the rest of the design space. In the case of this optimization run, the best value found by the algorithm was found before exploring the design space, but in other optimization module executions, the best value was found in later iterations.

Figures 4.2a, 4.2b, 4.2c, and 4.2d show the values for each design variable selected by the optimizer during the procedure compared to the resulting cost function values. The design variable

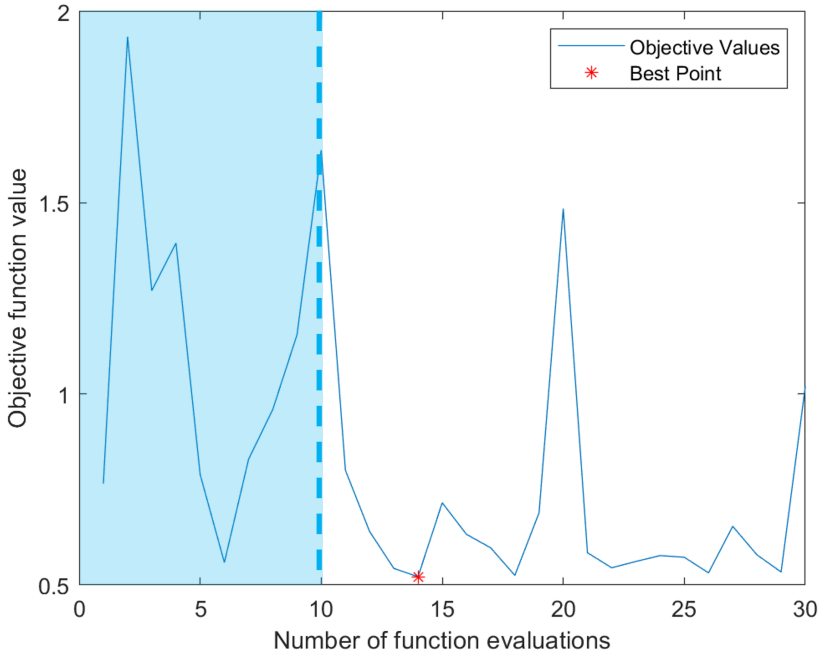

Figure 4.1: Objective cost function plotted against iteration number for the structural optimization. The blue area covers the initial evaluations prior to optimization.

Table 4.1: Design variable values found for the best vector in the structural optimization procedure.

Thickness, t (mm)	Connection Point, c (mm)	End Point, e (mm)	Overwrap Coefficient, a
0.05	-63.53	-21.00	0.12

values are plotted as scaled values between zero and one so that they can easily be compared. These plots show that, with the exception of the thickness design variable, there are potential minimum values spread through the design space, and that the design variable bounds are well defined. There is a clear trend in Fig. 4.2a showing that the optimizer is always selecting thickness values at or near the minimum bound. However, this optimization was run before the pressure load was increased to better match the aeroacoustic analysis, so it was decided that thickness could still be an important design variable to consider. The thickness design variable was therefore not set to a minimum value and removed from the optimizer.

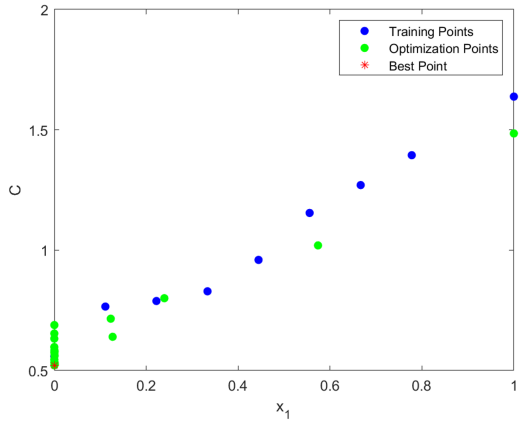

(a) Objective cost function plotted against the thickness.

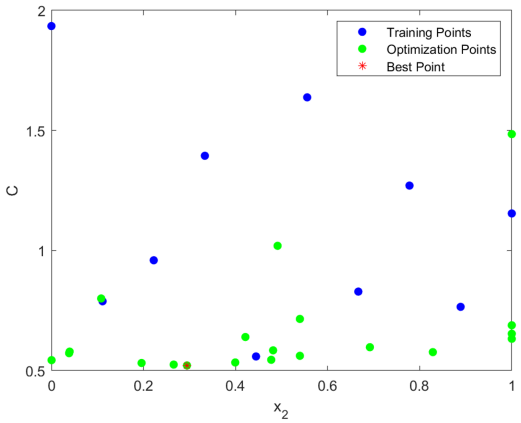

(b) Objective cost function plotted against the connection point.

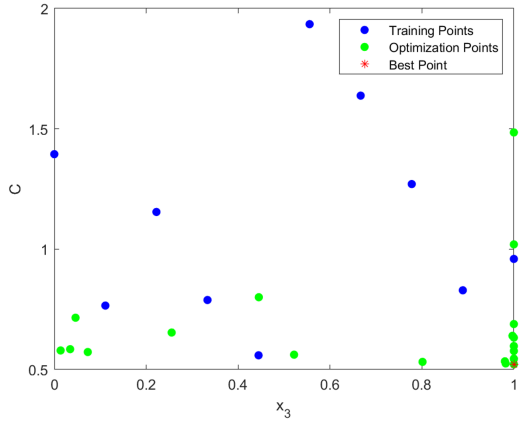

(c) Objective cost function plotted against the end point.

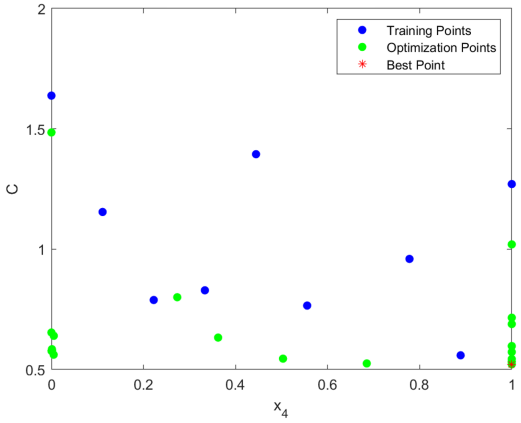

(d) Objective cost function plotted against the overwrap coefficient.

Figure 4.2: Comparison of normalized design variables plotted against objective cost for the optimization considering structural objectives.

Table 4.2: Objective variable and cost function values found for the best design vector in the structural optimization procedure.

Mass, M (g)	Actuation Force, A_F (N)	Cost, C
0.0028	0.0078	0.52

The best design vector found in the optimization procedure is presented in Table 4.1, and the resulting objective values are presented in Table 4.2. Finite element analysis results from Abaqus for the best design vector are shown in Figs. 4.3a, 4.3b, and 4.3c. These images depict similar maximum stress levels to the best configuration found in the WFAS SGF DOE study. However, this optimized configuration is significantly shorter than the best DOE configuration, resulting in a much lower mass and objective function value. Also, the optimized WFAS configuration returns to a completely stowed state while still under the applied pressure load, as can be seen in Fig. 4.3c. Similar to the DOE studies, the optimal design did not transform into martensite, so no martensite volume fraction figures are shown.

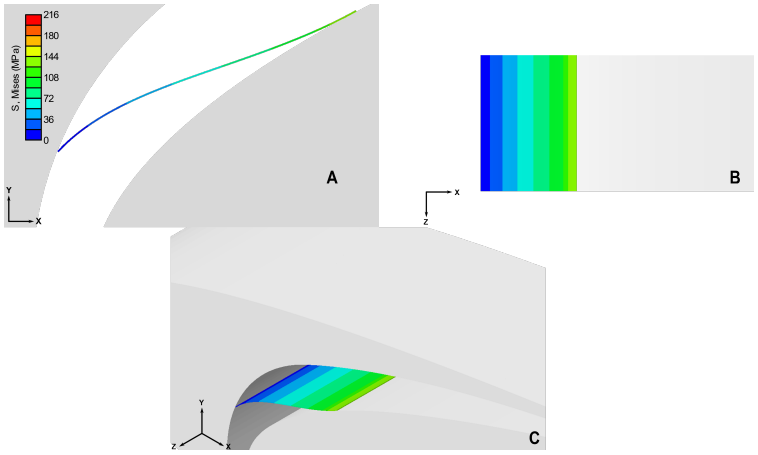

(a) Assembled state of the best WFAS SGF configuration.

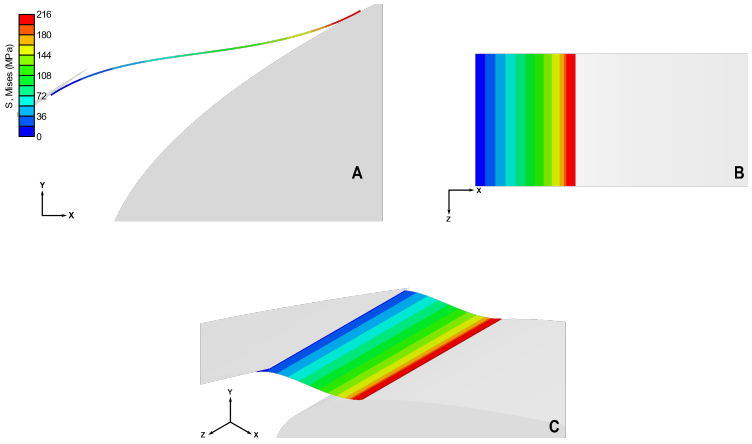

(b) Pressure loaded state of the best WFAS SGF configuration.

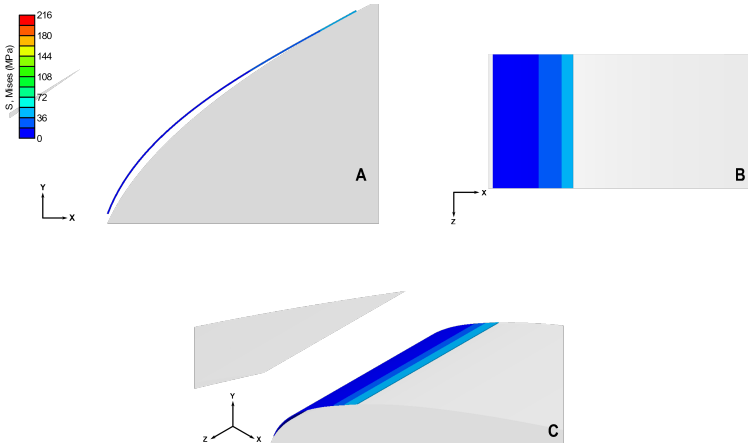

(c) Stowed state of the best WFAS SGF configuration.

Figure 4.3: Assembled, deployed, and stowed states of the best WFAS SGF found in the structural optimization.

Table 4.3: Design variables and bounds for the WFAS SGF preliminary optimization.

Design Variable (Units)	Symbol	Lower Bound	Upper Bound
Thickness (mm)	t	0.05	0.10
Connection Point (mm)	c	-66.0	-60.0
End Point (mm)	e	-22.0	-20.5
Overwrap Coefficient	a	0.10	0.12

4.2 Preliminary Structural and Aeroacoustic Objective Exploration

Following the structural optimization, the design variable bounds were updated and the noise objective, OASPL of a wing modified with a given SGF configuration, was added to the cost function. The updated design variable bounds are presented in Table 4.3. During the presented structural optimization, no runs failed or violated constraints. This helped the optimizer execute quickly but it also increased the chance that a successful design located near a constraint in the design space could be overlooked. Therefore, the connection point and end point design variable bounds were extended slightly. The thickness and overwrap coefficient design variable bounds were already determined by manufacturing and geometric restrictions, so they could not be modified. A test structural optimization was executed with the updated bounds prior to the preliminary total optimization, and it found a best cost function value of 0.5331. This value is similar to the one previously presented, and the design vector is also similar to the one discussed in the previous section with the exception that the end point variable moved to from the old lower bound of -21.0 to the new bound of -20.5. It was determined that the pressure load should be increased from 500 Pa to 3700 Pa in accordance with preliminary aerodynamic and aeroacoustic results at Mach 0.1 (35 m/s velocity).

A preliminary exploration was executed using the same methodology as the structural optimization, with the inclusion of the noise objective variable. This preliminary multiphysical exploration was executed with 5 spacefilling designs to create the initial surrogate and was optimized using EGO for 2 iterations. Because of runtime concerns, it was determined that a small exploration like

this could be useful to validate bounds, constraints, objectives, and optimizer procedure, prior to running a longer optimization. The objective cost equation used in the preliminary optimization is presented in Eq 2.15 and numerically as

$$C = 0.33\frac{M}{0.0033\ \text{g}} + 0.33\frac{A_F}{0.0038\ \text{N}} + 0.34\frac{N}{70.08\ \text{dB}}. \tag{4.2}$$

The objective progression of this preliminary exploration is shown in Fig. 4.4. This progression plot clearly shows that 2 iterations of EGO are not sufficient to find a minimum for the complexity of this design problem, since the best design vector was found in the spacefilling, surrogate defining iterations. The best design vector is presented in Table 4.4, and the vector of output variables for this design vector is presented in Table 4.5. Note that the structural results (mass and actuation force) presented in this table are multiplied by 1000 to approximately scale them from a 1 millimeter structure to a 1 meter structure. This was done such that these results are representative of an SGF structure the size of the experimental testing wing.

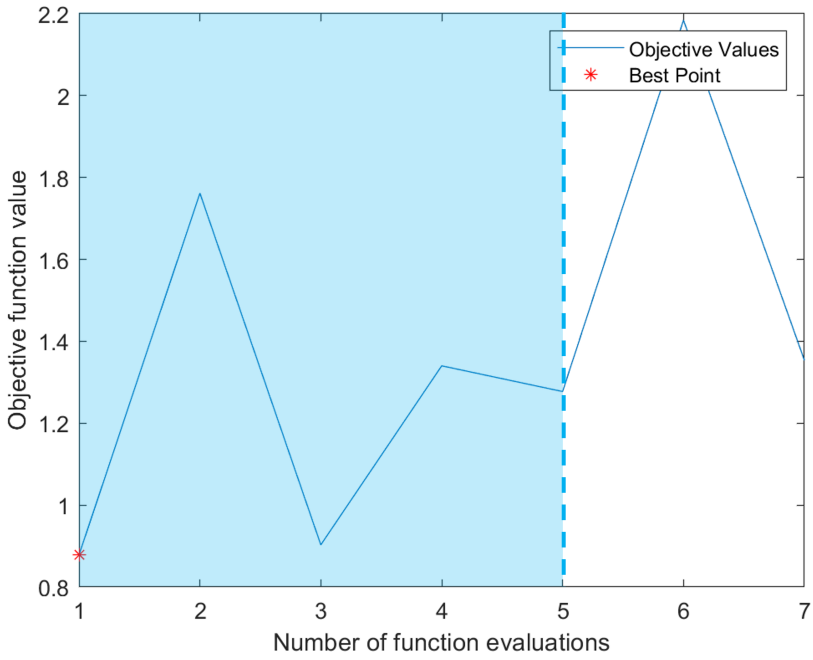

Figure 4.4: Progression of the objective cost function during the preliminary exploration.

Table 4.4: Design variable values found for the best vector in the preliminary exploration procedure.

Thickness, t (mm)	Connection Point, c (mm)	End Point, e (mm)	Overwrap Coefficient, a
0.05	-66.00	-21.25	0.11

Table 4.5: Objective variables scaled to match the wing in the wind tunnel and cost function values found for the best design vector in the preliminary exploration procedure.

Mass, M (g)	Actuation Force, A_F (N)	OASPL, N (dB)	Cost, C
1.88	30.70	89.29	0.88

4.2.1 Discussion of Preliminary Results

These results primarily demonstrate that the optimizer will have difficulty finding designs that reduce the calculated OASPL relative to the baseline wing value, which is around 73 dB. It is believed that this is because of two factors relating to the CAA methodology. First, no volumetric effects are considered in this analysis. It is likely that the shear layer formed beneath the slat in the untreated wing is a significant source of noise, and that WFAS SGF configurations inhibit formation of this shear layer. However, this shear layer is a volumetric effect so it is not considered in this optimization. Secondly, since the addition of a SGF increases the total surface area of the wing, it it possible that surface methods will always calculate more total noise for any SGF configuration.

Images of stress contours on the best WFAS SGF are presented in Figs. 4.5a, 4.5b, 4.5c, and 4.5d. Note that images of the SGF configuration in the retracted state are included along with the other states presented previously. These figures show much higher stresses compared to previous WFAS SGF results, but this is caused by the increased pressure load. Aside from this difference, the identified configuration is fairly similar to the best configuration found in the structural optimization.

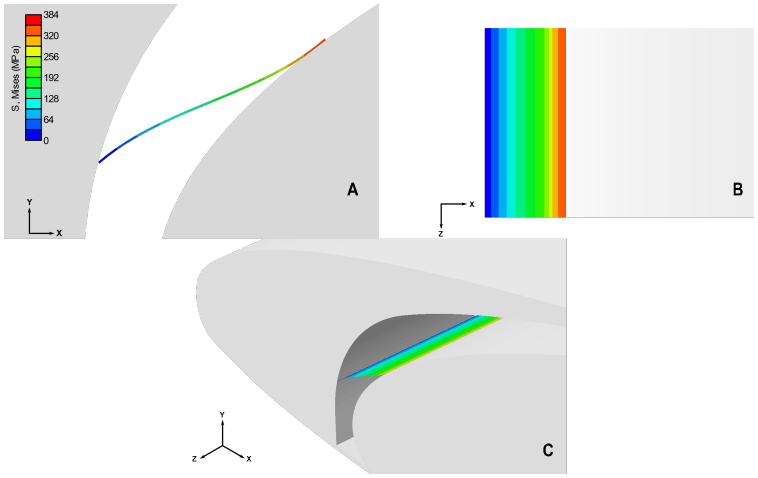

(a) Stress contours for the assembled state of the best WFAS SGF configuration.

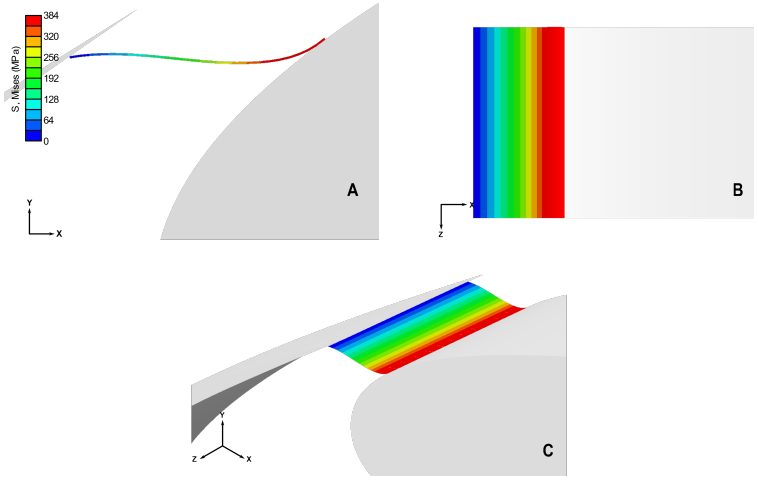

(b) Stress contours for the pressure loaded state of the best WFAS SGF configuration.

Figure 4.5: Stress contours for the best WFAS SGF configuration found in the preliminary exploration study.

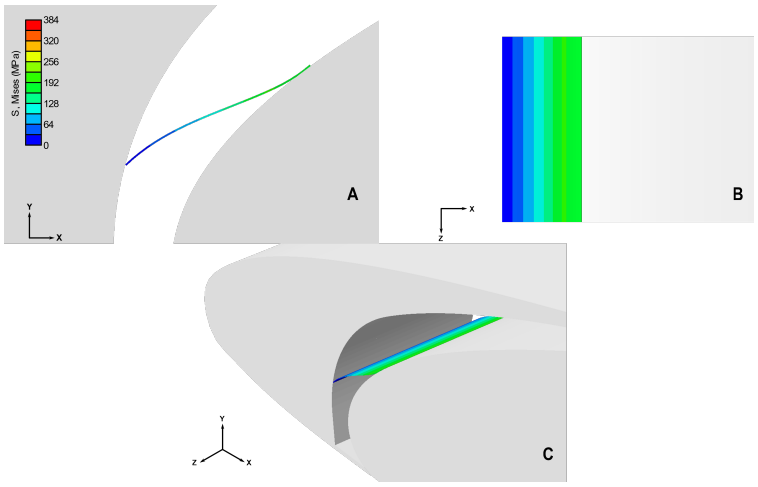

(c) Stress contours for the retracted state of the best WFAS SGF configuration.

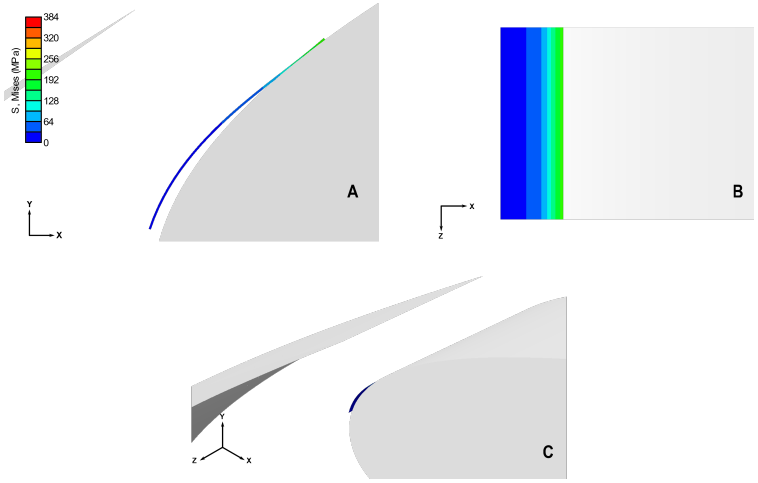

(d) Stress contours for the stowed state of the best WFAS SGF configuration.

Figure 4.5: Stress contours for the best WFAS SGF configuration found in the preliminary exploration study.

Due to the increased pressure loads and increased stresses, the best WFAS SGF configuration found by the preliminary exploration procedure did begin to transform into martensite, reaching a peak martensite volume fraction (MVF) near 0.25 while exposed to the pressure load. This WFAS SGF configuration transforms under pressure loading and recovers back to full austenite during stowing. However, the structure does not completely recover during the simulated retraction under pressure.

CFD results show that this configuration achieved a lift coefficient of 2.76 and a drag coefficient of 0.125 at the end of the analysis. The stabilized value for C_L is slightly greater than what is expected from similar studies. The value for C_D is slightly lower compared to the same result from similar studies, but the drag coefficient is more prone to error than the lift coefficient, as is discussed in Chapter 2. These values are both reasonable for this wing treated with an SGF.

4.3 Multiphysical Optimization of the WFAS SGF Concept

Following the structural optimization and the preliminary multiphysical exploration, a longer optimization procedure was executed. The aim of this optimization was to find a near optimal Wing Fixed Auto Stowed SGF considering structural and aeroacoustic objectives. As a result of the preliminary exploration, a few modifications were made to the optimizer. First, the total number of iterations was increased from 7 to 14. The bounds on each design variable were set to be the same as used in the preliminary exploration, as presented in Table 4.3. Additionally, the stowing constraint was updated to better account for configurations that detach from the slat but do not stow completely against the wing.

After testing the multiphysical optimization procedure with 14 functional evaluations, further modifications were made to improve the quality of the optimized solution. The density of the SMA was edited to better represent experimental materials. This modification was found to have little effect on selected previous designs. Additionally, the implementation of the noise objective, N, in the cost function was changed such that a maximum reduction in noise relative to the untreated wing would be calculated. The initial result of the multiphysical optimization procedure found a most optimal design with an overall sound pressure level (OASPL) of 87.35 dB, which is about

one decibel *louder* than the wing with no SGF treatment. To correct this error, the objective cost function was reformulated to be

$$C = 0.25\frac{M}{0.0019\ \mathrm{g}} + 0.25\frac{A_F}{0.0307\ \mathrm{N}} + 0.5\frac{N}{4.45\ \mathrm{dB}}. \tag{4.3}$$

where

$$N = \mathrm{OASPL}_{\mathrm{calc}} - \mathrm{OASPL}_{\mathrm{untreated}} \tag{4.4}$$

The value used for the OASPL of the simulated wing without any SGF treatment, $\mathrm{OASPL}_{\mathrm{untreated}}$ was found to be 86.45 dB using the same process for noise calculation described in Chapter 2. The value $\mathrm{OASPL}_{\mathrm{calc}}$ refers to the OASPL calculated for the wing treated with a WFAS SGF, which previously was the variable N. Note that this formulation results in a quieter wing relative to the baseline untreated wing resulting in a negative N term in the objective cost function while a relatively louder wing would result in a positive term in the cost function. The normalizing value of 4.45 dB was approximated from previous results. The other normalizing values are from the best output vector from the preliminary optimization.

The progression of the optimization procedure is shown in Fig. 4.6. The first five iterations of the optimizer were used to generate an initial surrogate of the objective space. These iterations are highlighted with the blue box in the figure. Five iterations may be sufficient to generate an initial surrogate for this problem because the optimizer immediately found one of the most optimal points in the first iteration of optimization. In this optimization procedure, the most optimal value was found in functional evaluation 10. Design variables and objective values from this iteration are presented in Tables 4.6 and 4.7, respectively. A magnified image of the local velocity contours and streamlines around the most optimal configuration is shown in Fig. 4.8. Additionally, the SGF studied in functional evaluation 10 had the lowest value of the cost function, even when ignoring the penalty applied to the configurations that violated constraints (3, 5, 7, 12, and 13).

Figures 4.7a, 4.7b, 4.7c, and 4.7d show the values for each design variable selected by the optimizer during the procedure compared to the resulting cost function values. These plots show

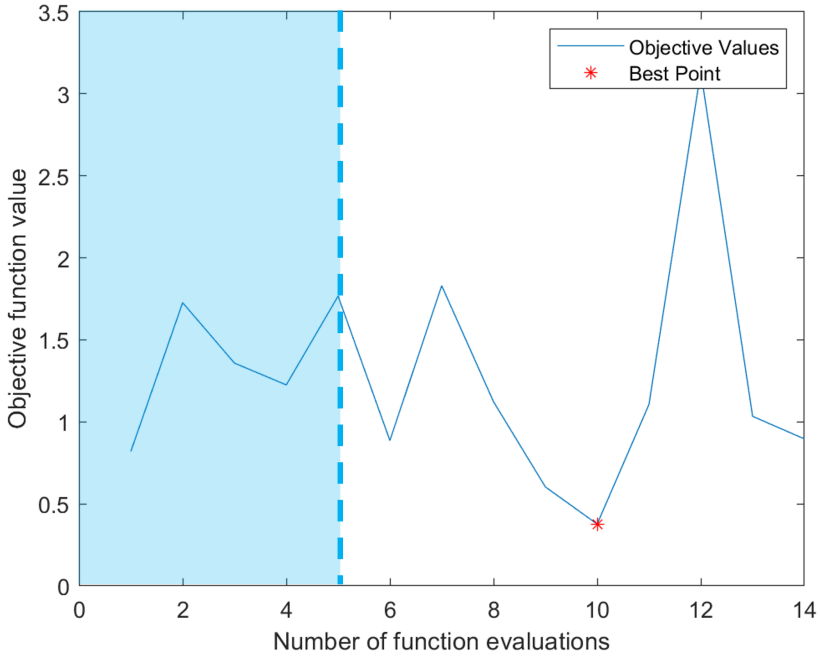

Figure 4.6: Progression of the objective cost function during the multiphysical optimization. The points to the left of the dotted line are the points explored during the spacefilling surrogate creation.

Table 4.6: Design variable values found for the best vector in the multiphysical optimization procedure.

Thickness, t (mm)	Connection Point, c (mm)	End Point, e (mm)	Overwrap Coefficient, a
0.0503	-66.00	-20.81	0.10

that, while the best configuration studied is located at the bounds of some design variables (thickness and connection point), other configurations located at these same bounds violated constraints. This suggests that there is a complex interaction occurring between the optimization bounds, constraints, and objectives, and that this area of the design space should be investigated with more functional evaluations. Additionally, these plots generally do not show positive or negative trends, suggesting that there are potentially good designs throughout the design space and that the design space is well defined for the WFAS SGF optimization problem.

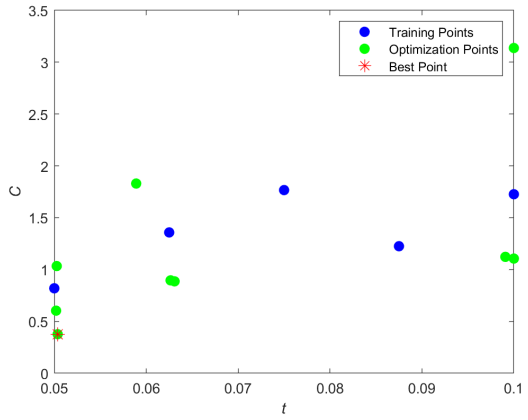

(a) Objective cost function plotted against the thickness.

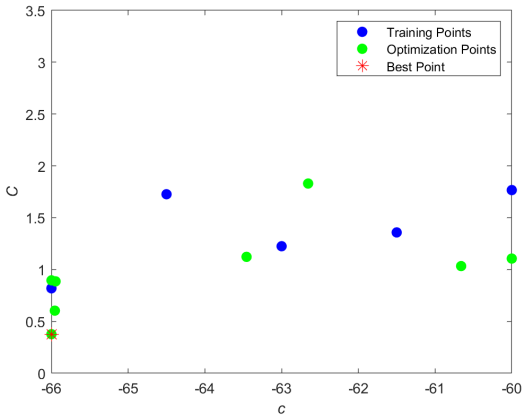

(b) Objective cost function plotted against the connection point.

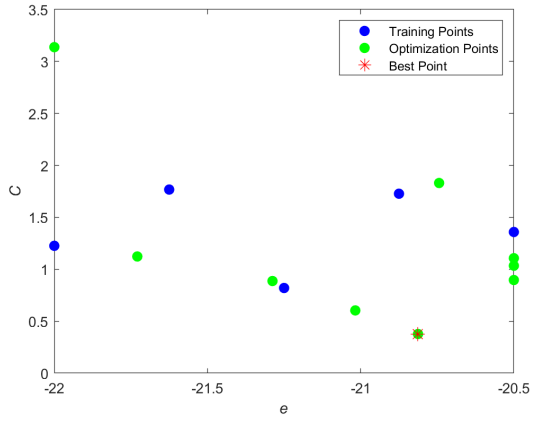

(c) Objective cost function plotted against the end point.

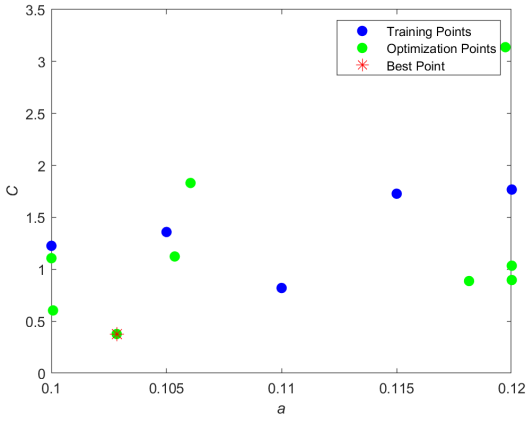

(d) Objective cost function plotted against the overwrap coefficient.

Figure 4.7: Comparison of design variables plotted against objective cost for the optimization considering multiphysical objectives.

Table 4.7: Objective variable and cost function values found for the best design vector in the preliminary optimization procedure. The mass and actuation force values are scaled to correspond application to the experimental model.

Mass, M (g)	Actuation Force, A_F (N)	OASPL, N (dB)	Cost, C
1.72	40.12	84.87	0.38

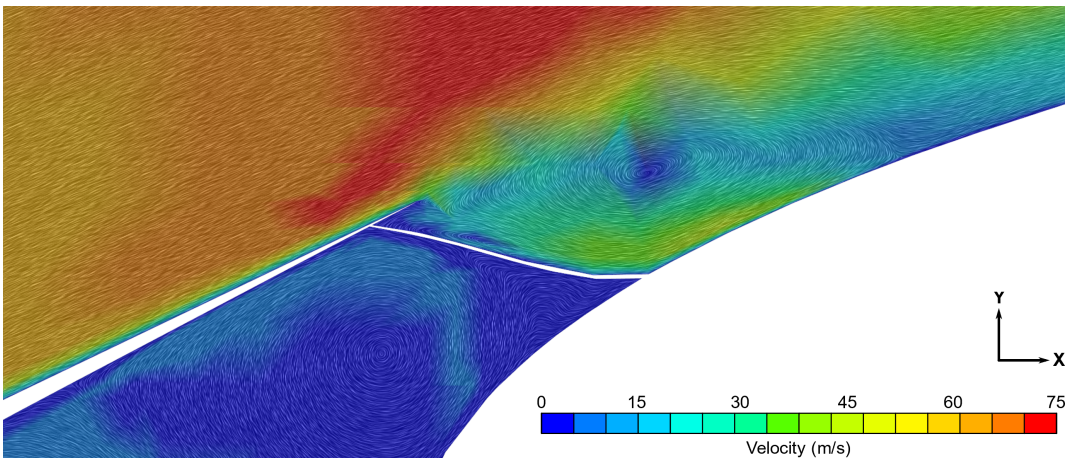

Figure 4.8: A magnified image of velocity CFD results around the best WFAS SGF configuration found in the multiphysical optimization. The streamlines in the image are line integral convolutions of the local velocity vector.

Structurally, the most optimal WFAS SGF configuration found in the multiphysical optimization is similar to the best configuration found in the structural optimization. The main difference is in the overwrap coefficient design variable, a, which is at the lower bound for the best multiphysically optimized configuration compared to being at the upper bound for the best structurally optimized configuration. This overall similarity results in an objective cost value of 0.78 for the multiphysically optimized configuration using the structural cost function, Eq. 2.14. Stress contours for the most optimal WFAS SGF configuration found in the multiphysical optimization are presented in Figs. 4.9a, 4.9b, 4.9c, and 4.9d. These figures show that a relatively large amount of stress is generated in this WFAS configuration, but this value still does not approach the yield stress constraint of 800 MPa.

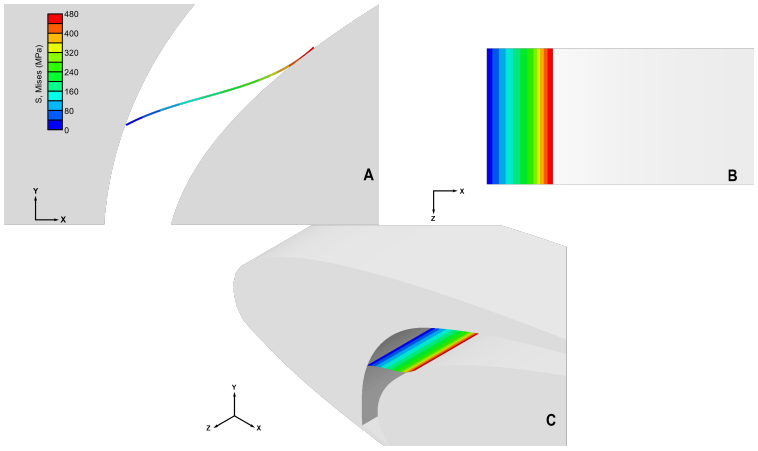

(a) Stress contours for the assembled state.

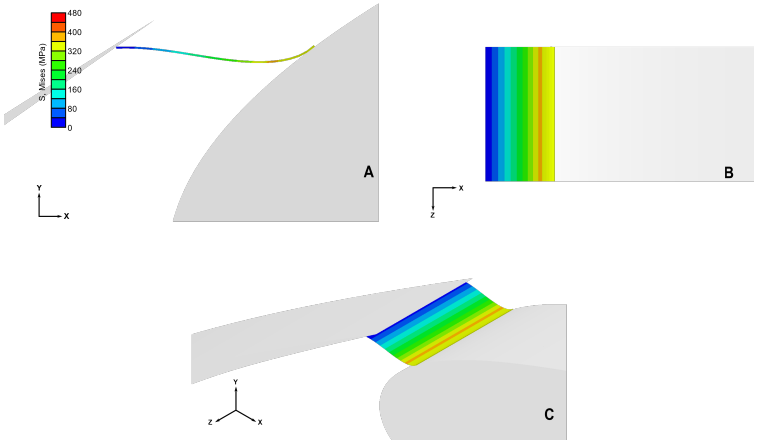

(b) Stress contours for the deployed and loaded state.

Figure 4.9: Stress contours for the best WFAS SGF configuration found in the multiphysical optimization study.

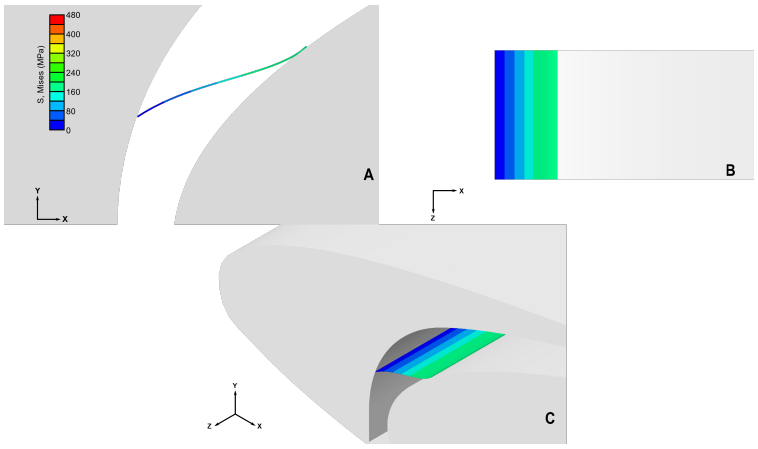

(c) Stress contours for the retracted state.

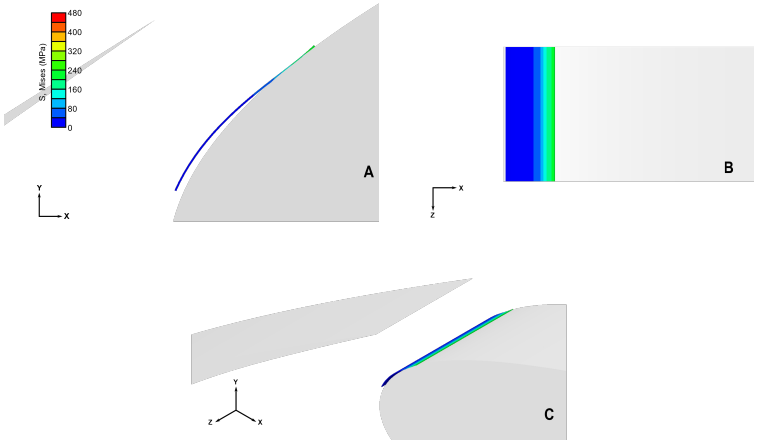

(d) Stress contours for the stowed state.

Figure 4.9: Stress contours for the best WFAS SGF configuration found in the multiphysical optimization study.

The best WFAS SGF configuration found by the multiphysical optimization procedure transformed into martensite slightly during the deployed and loaded stage of the analysis cycle. Martensite volume fraction (MVF) contours are shown in Figs. 4.10a, 4.10b, 4.10c, and 4.10d. Note that MVF ranges from 0 to 1 but the range on the contours presented is 0 to 0.5 to highlight the transformations. These figures show that this WFAS SGF configuration transforms under pressure loading and recovers back to full austenite during stowing but not during the simulated retraction. This result is similar to the result found in the preliminary exploration and suggests that a superelastic material may be necessary in the design of a noise reducing SGF. However, since full transformation to martensite does not occur, it is possible that other materials like beta-Titanium could suffice in the experimental testing setting.

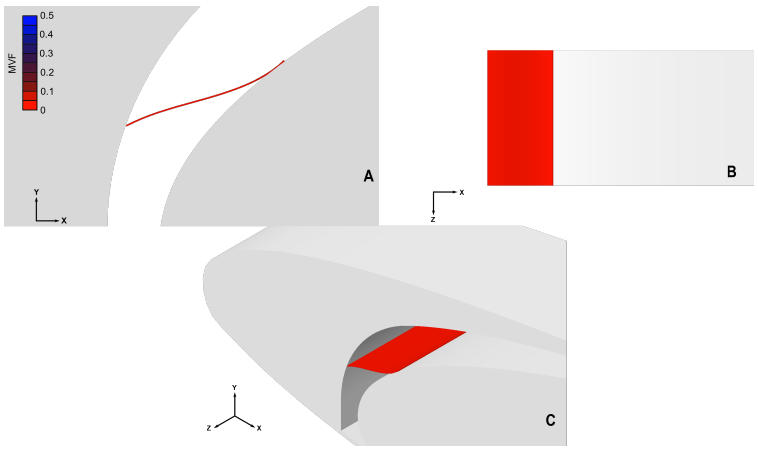

(a) MVF contours for the assembled state.

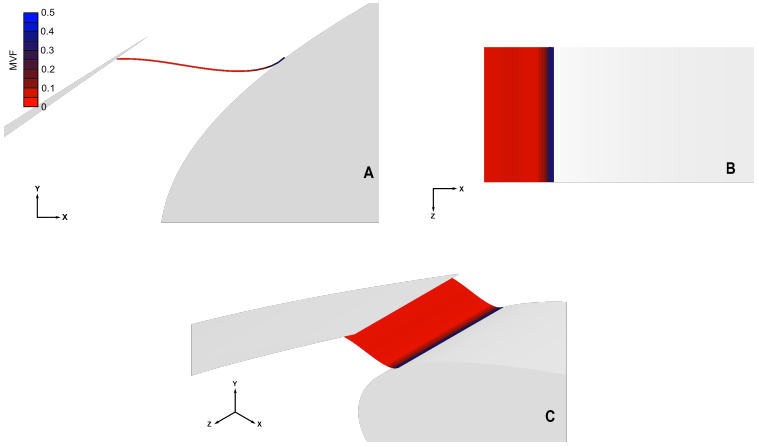

(b) MVF contours for the pressure loaded state.

Figure 4.10: Martensite volume fraction results for the best WFAS SGF configuration found in the preliminary optimization study.

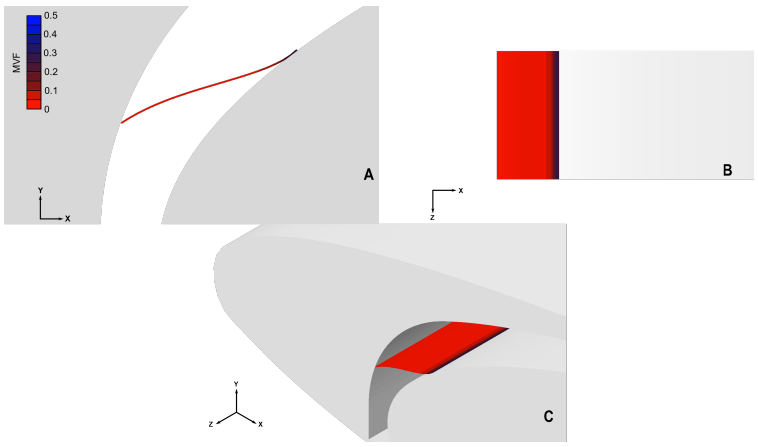

(c) MVF contours for the retracted state.

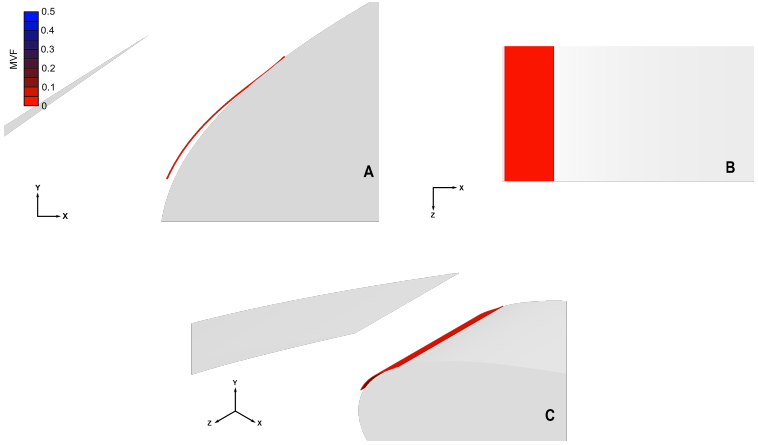

(d) MVF contours for the stowed state.

Figure 4.10: Martensite volume fraction results for the best WFAS SGF configuration found in the multiphysical optimization study.

The lift and drag coefficients from the most optimal iteration are 2.71 and 0.11. Mach number contours and streamlines are shown in Fig. 4.11. This image most clearly shows that flow underneath the slat is much slower compared to flow in this area of the untreated wing, where a high speed shear layer is present. This image also shows the extended, attached high speed flow region over the top of the wing, that is likely the cause of the higher-than-expected lift coefficient results. Furthermore, the lack of resolution in the wake behind the trailing edge flap is likely the cause of the lower-than-expected drag coefficient.

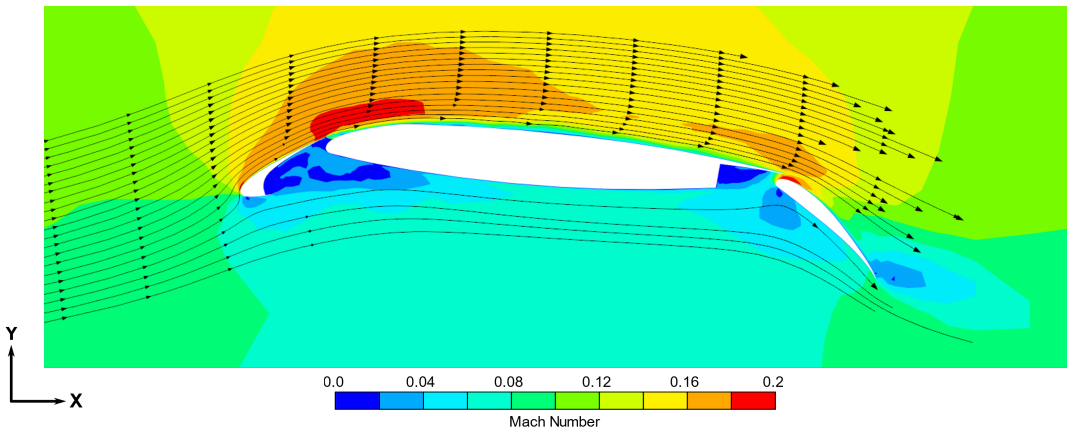

Figure 4.11: Mach number contours and streamlines for the most optimal WFAS SGF configuration applied to the wing in the acoustic tunnel section representative domain.

Acoustic results can be qualitatively viewed by subtracting the mean pressure over 200 iterations from the current pressure, as described in Equation 2.3. Areas where there is a significant positive or negative value of the contour plot shown in Fig. 4.12 are likely areas where noise is being generated. The contours shown for this WFAS SGF configuration follow the expected result that there are significant but small noise sources near the implemented SGF and larger noise sources present on the flap. This result for the most optimal SGF shows a consistent, smooth flow in most regions around the wing, except for the trailing edge of the slat where some increased vorticity occurs.

A plot of sound pressure level against frequency is shown in Fig. 4.13 where the red line repre-

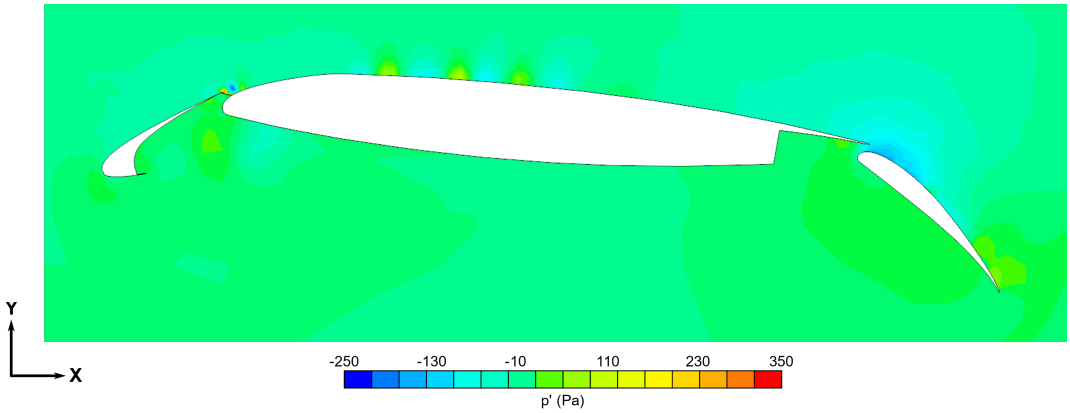

Figure 4.12: Acoustic pressure in Pa, as calculated by the formula presented in Equation 2.3. Areas showing pressure magnitudes far from zero represent locations where noise is generated.

sents the most optimal WFAS SGF wing treatment and the grey line represents the untreated wing. From this plot, it can be seen that the optimized SGF treatment reduces noise at low frequencies but is similar in noise level at higher frequencies. The OASPL from the most optimal configuration was 84.87 dB, which was the second quietest design studied in the optimization procedure. This suggests that the reformulation of the cost function was likely successful in emphasizing the noise objective, but further study is needed to confirm this conclusion.

Figure 4.14 also shows the simulated SPL versus frequency plot from the best WFAS SGF treatment compared to results from experimental studies of the untreated NASA CRM wing, a morphing slat cove filler wing treatment, and static slat cove and gap filler wing treatments from [25] and [11]. The inlet speed for each test is listed in parentheses in the figure legend. The plot of the most optimal WFAS SGF shows that there is a peak in sound pressure below 2 kHz and that there is broadband noise up to 15 kHz. (Broadband noise corresponds to SPL results above about 5kHz frequency in Fig. 4.14).

Comparing the computational result to previous experimental results is difficult due to the different inlet velocities and external tunnel noise present in experimental tests[1]. However, a few conclusions are clear. First, the relatively high OASPL of 84.87 dB found in the most optimal

[1]This external tunnel noise is mostly related to the carrier frequency of the wind tunnel controller which results in the clear spike in SPL present at 5kHz. Additionally, low frequency noise is generated by flow through wind tunnel features like the turning vanes and propeller.

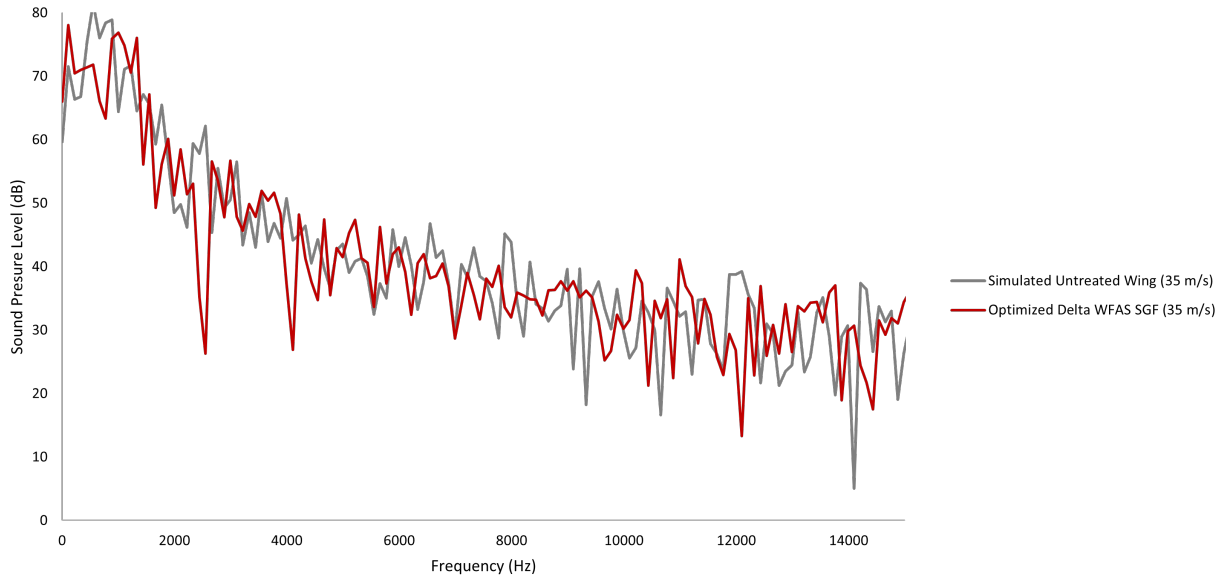

Figure 4.13: Sound Pressure Level in dB plotted against frequency in Hz for the optimized WFAS SGF (red) and the simulated untreated wing (grey).

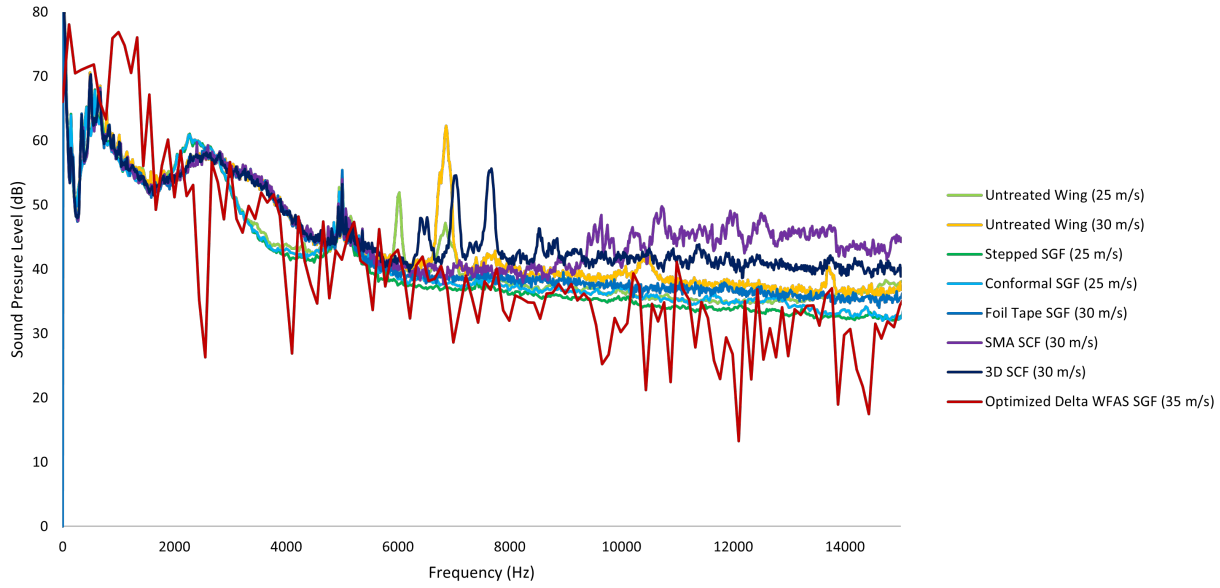

Figure 4.14: Sound Pressure Level in dB plotted against frequency in Hz for the optimized WFAS SGF, as well as experimental results for other slat gap and slat cove fillers tested in the wind tunnel [25, 11].

simulated WFAS SGF configuration is clearly a result of greater amount low frequency noise recorded in the CAA analysis. The reported OASPL result from these experimental studies was around 80 dB for a 30 m/s inlet velocity. This computational low frequency noise is partly caused by an increase in inlet velocity to 35 m/s, but other causes of this increase are uncertain. It is possible that this effect is partly due to the FW-H surface formulation used in this work and that a volumetric formulation would report a lower noise level.

Secondly, the broadband noise calculated at higher frequencies for the most optimal WFAS SGF appears to be lower than the broadband noise from any previous experiment. This effect is likely influenced by the wind tunnel noise present in experimental studies. However, this remains a promising result that demonstrates the potential effectiveness of an SGF, especially because the WFAS SGF was analyzed at a higher velocity compared to the experimental treatments. The higher analysis velocity should increase noise at all frequencies, so a lower broadband noise result suggests that this SGF configuration achieves the at least part of the stated noise reduction goal.

5. Mixed Reality Visualizations of Complex Multiphysical Results*

Through the design of experiment studies and optimization procedures executed for this thesis, it was discovered that it is difficult to present structural and aerodynamic simulation results for this problem with 2-dimensional media. Each structural result requires 3 unique views to display, and these views must be repeated for every state of each result and every display variable. Furthermore, only planar slices of the computational fluid dynamics results can be presented. These results could obscure 3-dimensional effects. Streamlines can be used to display flow results in a 3-dimensional format but these must be flattened and shown with a fixed perspective for traditional presentation methods. Work on other projects, like the design and experimental testing of small UAV models, revealed that these visualization limitations exists for many other projects as well. Sections of the following chapter were also published in a paper discussing mixed reality visualizations [36].

Virtual reality technology provides the capability to present and view 3-dimensional simulation results as if they were physical, 3-dimensional objects. Additionally, these virtual objects can be presented in conjunction with live video of the surrounding environment, termed video pass-through. The combination of virtual reality objects with video pass-through viewed with a head mounted display is called a mixed reality visualization[1]. In a mixed reality (MR) visualization, 3-dimensional results can be oriented relative to a physical, 3-dimensional environment like a wing in a wind tunnel test section.

Mixed reality result visualizations were found to be especially effective for projects attempting to compare simulated aerodynamic results generated with computational fluid dynamics to experimental aerodynamic results produced through wind tunnel testing, like the SGF design presented in this thesis. These visualizations can increase understanding of simulated results by presenting them in 3 dimensions while also enabling perception of relevant features to experimental analysis.

*Parts of this chapter were from "Mixed Reality Wind Tunnel Visualizations" by Schrass, J., Cate, J., Dean, J., and Hartl, D.; reprinted by permission of the American Institute of Aeronautics and Astronautics, Inc.

[1]The combination of video pass-through with virtual reality objects viewed with devices other than a head mounted display, like smartphones, is called an augmented reality visualization.

For example, an important region of flow too small to be individually observed in a wind tunnel test could be observed by overlaying CFD results on the test environment with mixed reality.

A mixed reality toolkit for viewing simulated aerodynamic results in conjunction with a wind tunnel test section was created to assist with visualizing the results generated for this thesis. The following sections describe the methods and terminology specific to this application of mixed reality research. Then, two example applications of the mixed reality toolkit are discussed.

5.1 Precompiled CFD Analysis

For the application of creating a MR wind tunnel environment, precompiling flow simulations is preferred to real-time CFD. Herein, precompiling is defined as computing a set of results and storing them for later presentation. This method allows for accurate simulation of complex flow structures that may occur when attempting to display flow around previously unknown aircraft models. In addition, precompiled flow simulations allow the user to change the size of the domain to show, for example, flow through the entirety of the closed-loop tunnel. Furthermore, precompiling simulations allows the user to adjust the precision of the CFD to the application. For example, a section spanning wing may require fewer computational cells to depict than a model of a rocket-propelled UAV. To create the precompiled result set, Star-CCM+ CFD display scenes containing flow information like velocity, pressure, or streamlines were stored.

5.2 Display Methodology for Mixed Reality Scenes

Unity was selected as the software development engine for this application because it is commonly used in generation of virtual and mixed reality experiences and because it supports the Oculus Experimental Passthrough API [37]. The Passthrough API provides developers with the capability to use the Oculus Quest 2 head mounted display (HMD) as a MR device by compositing video pass-through from the front facing cameras with 3D objects rendered in Unity.

The Oculus Quest 2 was selected as the HMD for this application because it is a low-cost MR device that does not require external tracking systems or cabling to a stationary computer, allowing for complete freedom of motion around the wind tunnel. The Oculus Passthrough API

enables highly interactive MR displays and can only be used with Quest devices. Additionally, there is an Oculus API that enables the use of hands in place of controllers by utilizing tracking information from the onboard cameras. The Quest 2 system provides a greater level of interactivity compared to other available HMDs through the combination of MR, hand-tracking, and wireless communication.

Unity uses software scenes as well as an entity-component system to pair with scripts in the C# coding language. A scene is a software environment that contains visualization and control information. Mixed reality objects are placed in a scene as entities. The entities are then given components provided by the Oculus API which allow the entities to be manipulated through Oculus interactions. Additional scripts can be added as components to display entities with a desired scale and orientation. For example, streamlines, particle flow, and contour images are selectable display options. These result objects were uniquely generated and applied to the wind tunnel environment by enabling video pass-through in the scene.

The Unity scene was compiled and loaded onto a Quest 2 device. The scene was designed to be manually oriented around the wind tunnel model using the a system of four anchor blocks which can be placed at the tunnel corners. CFD results stored on the headset were displayed to the user by toggling between the edit and display modes. An example scene demonstrating transparent virtual objects aligned to the wind tunnel is shown in Fig. 5.1. The MR visualization in conjunction with the wind tunnel provides the ability to move around the wind tunnel to look at different portions of the flow results.

5.3 Results Presented in Mixed Reality

CFD results were exported in the Virtual Reality Modeling Language (VRML) file format (for both 2- and 3-dimensional scenes) and were imported to the 3D graphics software, Blender. These files were converted to Filmbox (FBX) files using an in-house Python script.

The Python script functions by first isolating the 3-dimensional object on which to display the result information and deleting all other objects, including any unnecessary camera or viewport objects. Then, the script unwraps the object into individual components. This Blender process

Figure 5.1: An example mixed reality object (transparent blue) aligned with an experimental test article (section spanning wing) inside of the 4 ft. by 3 ft. wind tunnel using the Oculus Quest 2.

generates a flattened 2-dimensional configuration from a 3-dimensional geometry. Colors depicting result contours are imported at the vertices of cells in the CFD domain mesh. These vertex colors are mapped to the 2-dimensional configuration. The mapped vertex color information is converted to a Portable Network Graphic (PNG) image using the texture baking feature [38]. This texture conversion is required because Blender and Unity display objects using surface color information but Star-CCM+ exports objects with color information stored in the cell element vertices. Finally, the script exports the object containing CFD results as an FBX. These FBX files and PNG files were imported to the game development engine Unity 3D and placed in MR visualization scenes. Within Unity the PNG file was applied to a 3-dimensional object as a material. The combination of the PNG file produced from texture baking and the FBX file containing a 3-dimensional object allowed for display of high fidelity data within the Unity environment.

5.3.1 2-dimensional Planar Data

Planar data displayed as 2-dimensional images in CFD software was exported from Star-CCM+ and converted to Unity objects using the Blender script. Reflective color display and scaling attributes were applied to the Unity object. Displaying 2-dimensional result objects in

a 3-dimensional scene allowed for simultaneous display of multiple slices of the domain. For example, velocity contour slices in front of, near, and behind the wing in the tunnel domain were be viewed at the same time using this post-processing method. When the user selected this display a spherical light generating object was spawned into the scene. The light source object was moved around the domain and resized to provide more or less light using hand-tracking controls. This light source only illuminated the results close to it such that all data slices were simultaneously present in the scene but only certain sections were viewed at any given time. A planar data display example is shown in Fig. 5.2.

Figure 5.2: A demonstration of the hand-tracked light source planar display showing pressure contours between several planar slices of a CFD result.

5.3.2 3-dimensional Streamline Data

Streamline results were generated using the streamline generator in Star-CCM+ and exported as 3-dimensional objects using the VRML file format. The streamline generator in Star-CCM+ spawns streamlines from a geometrically defined location and then uses a flow quantity and a Runge-Kutta scheme to determine the streamline location. For this application, velocity was the flow quantity utilized and the adaptive step Runge-Kutta solver was used.

The generated VRML file was imported to Blender and converted to the FBX file format using the procedure described above. After a 3D object was imported to Unity, the object was given attributes that display it as an interactive object and size it according to user specified dimensions. The process for displaying other 3-dimensional static objects such as flow quantity isosurfaces is nearly identical to the described process. An example of a streamline result is shown in Fig. 5.3.

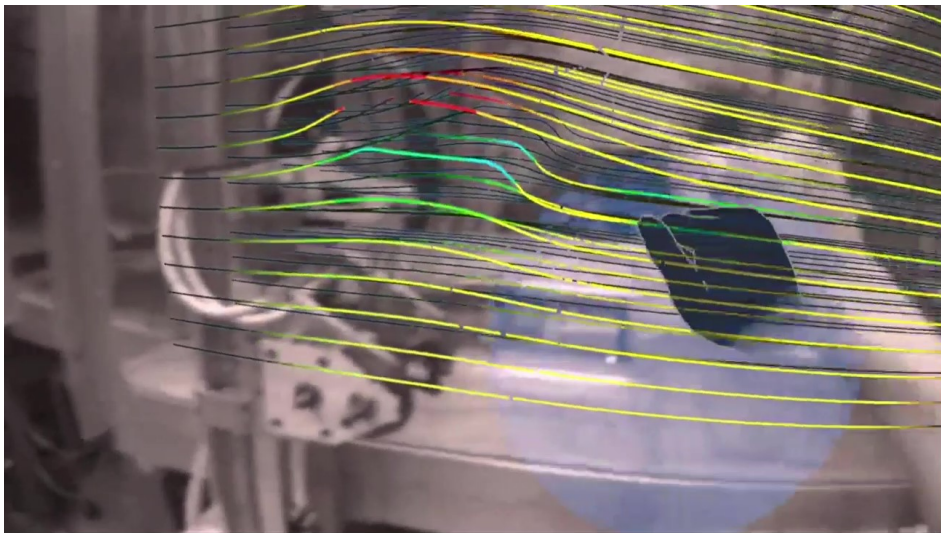

Figure 5.3: Virtual velocity streamlines displayed in the wind tunnel section using Oculus Passthrough technology.

5.3.3 Particle-Spawning to Represent Flow Data

Particles were spawned into an empty scene using a controller trigger input. These particles display flow information by moving to follow the local velocity vector nearest to the particle. Additionally, the particles changed in size and color to represent pressure gradients as they moved through the flow. The flow data (velocity and pressure) was stored in Star-CCM+ per cell present in the CFD solution. This data was tabulated and exported to a comma-separated value (CSV) file. Cell location information was also stored in the CSV file.

This data storage method creates exceptionally large file sizes if the CFD mesh exceeds around 100,000 cells. To enable an accurate, refined CFD mesh, a 2-dimensional slice of the mesh can be

exported. In this case, it is assumed that the flow data does not change significantly in the span-wise direction, as is the case in the section spanning wing example. Exporting a 2-dimensional mesh slice is facilitated using quadrilateral meshes Star-CCM+ with a slice specified at a location in the simulated domain.

The flow data stored in the CSV file was imported to Unity using a C# script. This script also contained the algorithm that determined movement of each particle. Currently, the script determines the location of the nearest cell to each particle at each increment of time using a brute-force search, but implementation of a more efficient K-D tree algorithm is under investigation. Once the nearest cell to a particle is determined, the algorithm interpolates between the current velocity vector of the particle and the velocity vector of the nearest cell. This interpolated velocity vector is then applied to the particle and time is incremented before repeating the process. The pressure scalar stored in the particle is directly set to be the pressure scalar in the nearest cell. The movement algorithm iterated once every 15-30 milliseconds for the number of cells used in this work. Note that the velocity applied to each particle in the scene was scaled down from the CFD velocity results such that the particle can be visualized moving down the tunnel. A particle moving at CFD velocity would traverse the display domain in less than a tenth of a second.

The particles spawn into the pass-through scene at the end of a indicated, variable length extension of the controller so that the user can generate particles anywhere in the wind tunnel section without physically moving. An example of the particles following the velocity field is shown in Fig. 5.4.

5.4 Example Tool Usage

To demonstrate the MR wind tunnel experience, example scenes were shown to undergraduate students and to technical researchers. The visualization shown to students was based on results from a class project, while the visualization shown to technical researchers was generated using results from a technical study.

In the case of the student project, the students designed wing and horizontal stabilizer features on a model scale rocket-propelled UAV to meet specified aerodynamic criteria. The models were

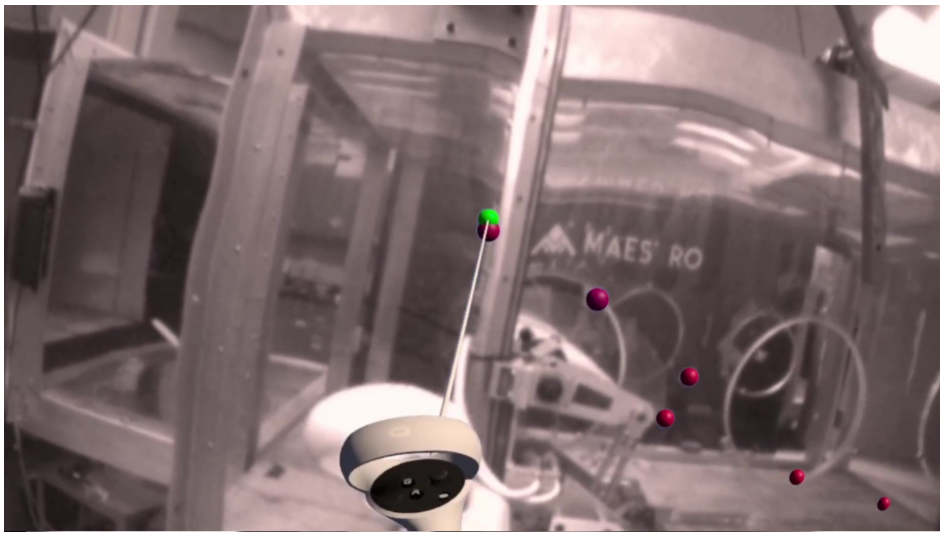

Figure 5.4: A set of particles following local velocity vectors as they move through the pass-through scene in the wind tunnel section.

3D printed and tested in the wind tunnel to verify their analytical calculations. These models were simulated in tunnel flow using CFD and the model results were displayed in the MR environment. This visualization provided students with the ability to see flow structures created by their model. A student utilizing the MR system is shown in Fig. 5.5A and a scene viewed by this student is shown in Fig. 5.5B.

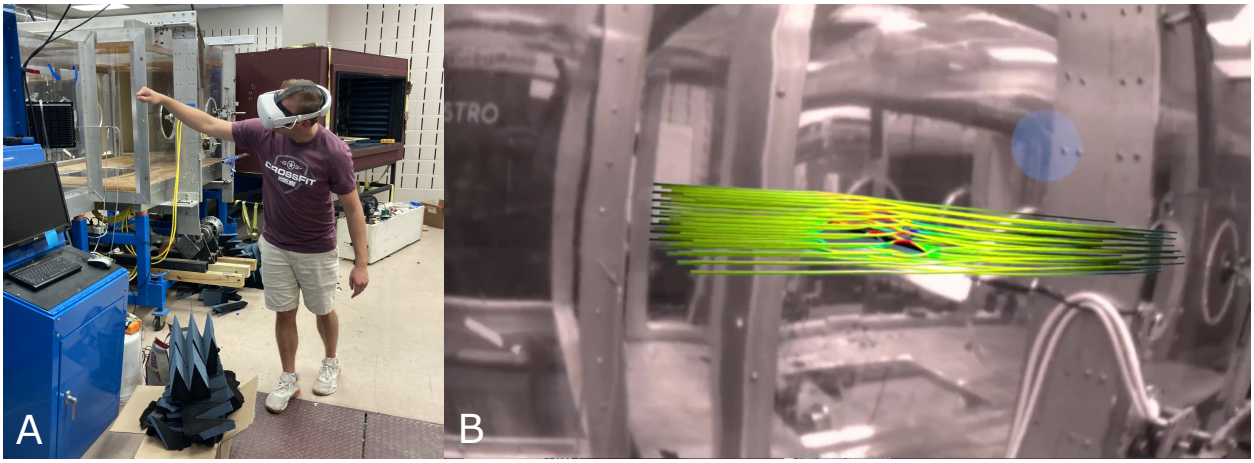

Figure 5.5: A student standing in front of the wind tunnel section wearing the Quest 2 headset (A) and a view of streamlines around a UAV seen by the student (B).

The second test case centered around SGF design for the NASA CRM wind tunnel model. The MR visualization allowed researchers to examine aerodynamic changes caused by potential designs at test scale before manufacturing the modifications. Also, the MR experience allowed the design discussion to be broadcast to collaborators who were not physically present at the test facility. This MR scene is shown being broadcast in an online video call in Fig. 5.6.

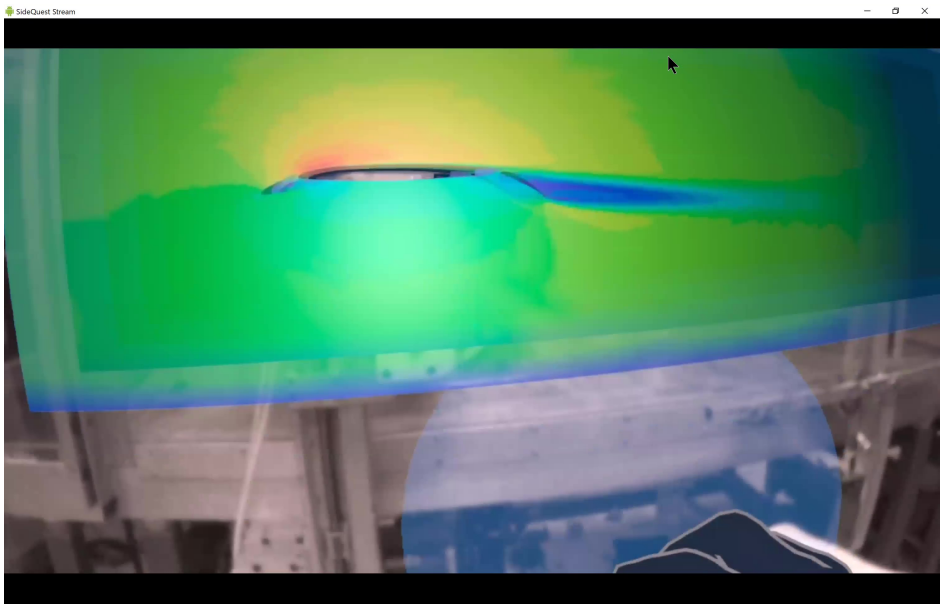

Figure 5.6: An image of the pass-through scene being broadcast in a video call to assist in a research technical presentation.

For both cases, participants viewing the MR demonstration scenes provided feedback on potential ways to improve the system and on how the system could affect their usage of the wind tunnel testing facility. Three main points of feedback revealed from these discussions are:

1. The demonstrated MR scene provides a new way to view wind tunnel experimentation and encourages participants to think about the aerodynamic effects that created their results instead of focusing on scalar force outputs.

2. More options for data display such as shear force displays or acoustic pressure displays would improve the visualization.

3. Colorful CFD results displayed on top of a low-resolution grayscale video feed can be disorienting. However, visualized results are robust to movement around the tunnel and viewing from multiple angles.

This feedback suggests that the mixed reality toolkit is an effective framework for presenting complex, 3-dimensional results. It assisted with technical discourse surrounding the design of an SGF for experimental testing by highlighting areas where flow was modified by a SGF design. Additionally, the flexibility of the MR toolkit was demonstrated in applying it to multiple testing scenarios.

6. Summary and Conclusions

This work has presented a novel simulation workflow by which a morphing slat gap filler can be defined, structurally analyzed, acoustically analyzed, and visualized for analysis. While it is not clear from this first analysis that the shape memory alloy slat gap fillers designed herein are effective at reducing aircraft noise, this framework provides future researchers with the tools necessary to identify such a structure. The shortcomings of this work are largely caused by limitations on simulation scale caused by the more limited computational resources used for intensive iterative framework development. Follow on efforts should consider implementation of this framework using more powerful computational hardware and potentially a high performance computing center. Furthermore, a novel visualization method for wind tunnel testing was developed such that future students and researchers can better understand how their simulation results relate to a wind tunnel flow environment. This tool will be useful not only for the continuation of this project but also for any future projects utilizing wind tunnel facilities. A summary of the findings of this work are itemized as follows:

- Three unique SGF concepts (Fig. 1.6) were geometrically defined and structurally analyzed using accurate models for SMA structural behavior.
- A simulation framework was defined by which an SGF could be quantitatively analyzed structurally and acoustically using Abaqus FEA and Star-CCM+ CFD and CAA solvers (Fig. 2.1).
- The three concepts were compared such that the concept with the most potential for experimental testing was studied in optimization (Figs. 3.2a, 3.2b, 3.4a, 3.4b, 3.6a, and 3.6b).
- One SGF concept, the Wing Fixed Auto Stowed SGF, was selected for further study in an optimization procedure (Figs. 3.8a, and 3.8b).
- The WFAS SGF was optimized to two unique configurations: one considering only struc-

tural objectives (Tables 4.1 and 4.2) and the other considering structural and aeroacoustic objectives (Fig. 4.8).

- The WFAS SGF optimized for noise reduction demonstrated a potential to reduce overall noise if implemented in an experimental test article (Figs. 4.13 and 4.14).

- A mixed reality visualization tool was developed to help students and researchers understand the flow features that cause various measurements in a wind tunnel testing environment (Fig. 5.5).

- The mixed reality visualization tool is prepared for expanded use on other projects and models, as well as for continued use in this project.

- A simulated WFAS SGF was examined as a candidate for manufacturing and experimental testing using the mixed reality visualization tool (Fig. 5.6).

6.1 Challenges

The main challenges encountered in this work were related to computational hardware limitations. Computational fluid dynamics and computational aeroacoustics analysis is very dependent on simulation mesh quality, and the fluid meshes generated in this work were limited by the available memory hardware. These mesh limitations had the effect that only certain flow results like lift coefficients and surface generated noise could be considered as valid results; more detailed flow phenomena like volumetric noise sources could not be considered. Also, further investigation is necessary to determine what method of application of the Ffowcs Williams-Hawkings formulation is most comparable to experimental work. Specifically, a study should be carried out to examine the effect of noise sources originating on the top surface of the wing, potentially by taking simultaneous experimental measurements using two microphone arrays with one aimed at the top and one aimed at the bottom surface of the wing.

A CFD boundary condition that allowed for CAA propagation while accurately representing the mesh wind tunnel walls was not found. Successfully implementing a boundary condition that

simultaneously provides these two conflicting phenomena (acoustic pressure propagation and no-penetration of flow) would likely improve the accuracy of CFD results compared to experimental analysis while allowing for the previously suggested improvements to the CAA analysis.

While the efficient global optimization algorithm was demonstrated to be effective for a limited number of functional evaluations, an extremely small number of functional evaluations was necessitated by an average configuration evaluation runtime of more than 10 hours. It is likely that a better solution could have been found if more functional evaluations were executed, and if more consideration was given to the optimizer parameters. Specifically, either investigation of a better formulation of the objective cost function or elimination of the objective cost function using a multiobjective EGO code like [33] is suggested. Additional improvements to the optimizer could be found by considering other surrogate-based algorithms and by an alternate method of considering objective constraints that does not influence the surrogate. A repository of different codes which could be used to make these improvements can be found from [34].

6.2 Further Work

To build upon this work, there are several potential areas for improvement. The first and most obvious improvement would be to create better discretized simulation domain meshes. This would enable the computation of volumetric noise sources and would likely improve the accuracy of the simulation relative to experimental tests. In addition, executing more functional evaluations during optimization would provide greater confidence that a near-global minimum was found and that there are not better designs that simply were not evaluated. Both of these framework modifications could be enabled by establishing the capability to execute functional evaluations on a supercomputer.

If these simulation improvements are made, the next step for this analysis would be to verify the results found in the simulation with experimental testing. The best WFAS SGF configuration found in the optimization procedure demonstrated a potential to reduce noise while being applied to the experimental model, so manufacture and testing of an experimental model based on this configuration is recommended. The facilities at Texas A&M are capable of carrying out this

experimental testing. Further computational analysis may be required prior to this experimental step if it is determined that the limitations on the WFAS SGF results presented herein prohibit the described solution from achieving the stated noise reduction goal. If this is the case, further examination of the other two SGF concepts is recommended.

Finally, technological improvements to computational codes and available hardware will provide the potential to dramatically improve these analyses. As discussed, more improvements to simulation solvers would provide greater confidence in the determined solution and could provide the novel capability to simulate structural and aeroacoustic interactions at full scale, where the number and indeterminate nature of complexities currently prohibit analysis. Technological advancement could also significantly improve the mixed reality visualization tool by providing greater ease of use and understanding with improvements like adding color to the video feed. These advancements are being pursued by other researchers, so it will be important to the future of this project that technological advancements are unitized when they become available.

Moving forward, manufacturing design and experimentation on an SGF using a novel translating microphone array will provide new information to the field of morphing aerostructural noise reduction in the slat gap area. Also, increased usage of MR technologies for educational and research discourse will provide an enhanced understanding of complex phenomena both to beginners and to field experts. Therefore, the framework presented herein will be necessary to provide a baseline for future improvements.

REFERENCES

[1] C. Clark, "Aircraft noise effects on health," *Centre for Psychiatry*, 2015.

[2] M. Basner, C. Clark, A. Hansell, J. I. Hileman, S. Janssen, K. Shepherd, and V. Sparrow, "Aviation noise impacts: state of the science," *Noise & health*, vol. 19, no. 87, p. 41, 2017.

[3] M. Khorrami and D. Lockard, "Effects of geometric details on slat noise generation and propagation," in *12th AIAA/CEAS Aeroacoustics Conference (27th AIAA Aeroacoustics Conference)*, p. 2664, 2006.

[4] K. Mau and W. Dobrzynski, "Flexible airflow separator to reduce aerodynamic noise generated by a leading edge slat of an aircraft wing," Sept. 14 2004. US Patent 6,789,769.

[5] W. Gleine, K. Mau, and U. Carl, "Aerodynamic noise reducing structure for aircraft wing slats," May 28 2002. US Patent 6,394,396.

[6] W. D. Scholten, D. J. Hartl, T. L. Turner, and R. T. Kidd, "Development and analysis-driven optimization of superelastic slat-cove fillers for airframe noise reduction," *AIAA Journal*, vol. 54, no. 3, pp. 1078–1094, 2016.

[7] R. Patterson, W. Scholten, T. Strganac, T. Turner, and D. Hartl, "Experimental validation of a shape-memory alloy slat-cove filler: Structural response and computational model development," *Journal of Intelligent Material Systems and Structures*, vol. 31, no. 17, pp. 1986–2001, 2020.

[8] A. Leaton, W. Scholten, K. Lieb, D. J. Hartl, T. Strganac, and T. L. Turner, "Aerostructural and aeroacoustic experimental testing of shape memory alloy slat cove filler," in *AIAA Scitech 2020 Forum*, p. 1040, 2020.

[9] T. L. Turner and D. L. Long, "Development of a sma-based, slat-gap filler for airframe noise reduction," in *23rd AIAA/AHS Adaptive Structures Conference*, p. 0730, 2015.

[10] Y. Zhang, L. N. Cattafesta, K. A. Pascioni, M. M. Choudhari, D. P. Lockard, M. R. Khorrami, and T. Turner, "Slat noise control using a slat gap filler," in *AIAA AVIATION 2020 FORUM*, p. 2553, 2020.

[11] M. S. Mu, J. Schrass, K. F. Lieb, and D. J. Hartl, "Aerodynamic and aeroacoustic experimentation of a slat-gap filler for airframe noise reduction," in *AIAA Scitech 2021 Forum*, p. 1997, 2021.

[12] D. Lagoudas, *Shape memory alloys: modeling and engineering applications*. New York: Springer, 1st ed ed., 2008.

[13] F. T. Calkins, J. H. Mabe, and G. W. Butler, "Boeing's variable geometry chevron: Morphing aerospace structures for jet noise reduction," in *Smart Structures and Materials 2006: Industrial and Commercial Applications of Smart Structures Technologies*, vol. 6171, p. 61710O, International Society for Optics and Photonics, 2006.

[14] P. B. Leal, H. R. Stroud, and D. J. Hartl, "Design and fabrication of a shape memory-based bio-inspired morphing wing," in *VIII ECCOMAS Thematic Conference on Smart Structures and Materials (SMART)*, 2017.

[15] S. Bryson, S. Johan, L. Schlecht, B. Green, D. Kenwright, and M. Gerald-Yamasaki, "The virtual windtunnel," in *Computational Fluid Dynamics Review 1998: (In 2 Volumes)*, pp. 1113–1130, World Scientific, 1998.

[16] D. Paeres, J. Santiago, C. J. Lagares, W. Rivera, A. B. Craig, and G. Araya, "Design of a virtual wind tunnel for cfd visualization," in *AIAA Scitech 2021 Forum*, p. 1600, 2021.

[17] A. R. Harwood, P. Wenisch, and A. J. Revell, "A real-time modelling and simulation platform for virtual engineering design and analysis," in *Proceedings of 6th European Conference on Computational Mechanics (ECCM 6) and 7th European Conference on Computational Fluid Dynamics (ECFD 7)*, pp. 11–15, 2018.

[18] R. Durscher, A. M. Pankonien, and N. Bhagat, "Aardvark: Aerospace analysis and design in virtual and augmented reality toolkit," in *AIAA Aviation 2019 Forum*, p. 3560, 2019.

[19] "Simcenter vr - why cfd engineers need it in 2020." https://blogs.sw.siemens.com/simcenter/star-ccm-vr-who-needs-it-you-do-already/, Jul 2020.

[20] F. Bruno, F. Caruso, L. De Napoli, and M. Muzzupappa, "Visualization of industrial engineering data visualization of industrial engineering data in augmented reality," *Journal of visualization*, vol. 9, no. 3, pp. 319–329, 2006.

[21] J.-R. Lin, J. Cao, J.-P. Zhang, C. van Treeck, and J. Frisch, "Visualization of indoor thermal environment on mobile devices based on augmented reality and computational fluid dynamics," *Automation in Construction*, vol. 103, pp. 26–40, 2019.

[22] P. Benölken, H. Graf, and A. Stork, "Exploring flow fields in augmented reality environments," in *Workshop on Augmented Virtual Reality (AVIR). Genf, Schweiz*, pp. 36–38, 2003.

[23] T. Schweiß, D. Nagaraj, S. Bender, and D. Werth, "Towards collaborative analysis of computational fluid dynamics using mixed reality.," in *VISIGRAPP (1: GRAPP)*, pp. 284–291, 2021.

[24] F. Auricchio and R. L. Taylor, "Shape-memory alloys: modelling and numerical simulations of the finite-strain superelastic behavior," *Computer Methods in Applied Mechanics and Engineering*, vol. 143, no. 1, pp. 175–194, 1997.

[25] A. Leaton, "Experimental testing of a shape memory alloy slat cove filler for noise reduction," 2020.

[26] Siemens Digital Industries Software, "Simcenter STAR-CCM+ User Guide v. 2020.3," Siemens 2020.

[27] F. Götten, D. Finger, M. Marino, C. Bil, M. Havermann, and C. Braun, "A review of guidelines and best practices for subsonic aerodynamic simulations using rans cfd," 12 2019.

[28] "2d multielement airfoil verification - intro page." https://turbmodels.larc.nasa.gov/multielementverif.html, 2021.

[29] J. Ruiz, "Star-ccm+: Naca0012 flow and aero-acoustics analysis." http://mdx2.plm.automation.siemens.com/presentation/star-ccm-naca0012-flow-and-aero-acoustics-analysis, 2011.

[30] J. Müller, "User guide for modularized surrogate model toolbox," 2012.

[31] D. R. Jones, M. Schonlau, and W. J. Welch, "Efficient global optimization of expensive black-box functions," *Journal of Global optimization*, vol. 13, no. 4, pp. 455–492, 1998.

[32] G. Wilson, D. Lagoudas, and D. Hartl, "Designing a morphable parabolic reflector antenna using origami-inspired discretization and efficient global optimization," in *Smart Materials, Adaptive Structures and Intelligent Systems*, vol. 84027, p. V001T03A017, American Society of Mechanical Engineers, 2020.

[33] J. Knowles, "Parego: A hybrid algorithm with on-line landscape approximation for expensive multiobjective optimization problems," *IEEE Transactions on Evolutionary Computation*, vol. 10, no. 1, pp. 50–66, 2006.

[34] Y. Tian, R. Cheng, X. Zhang, and Y. Jin, "Platemo: A matlab platform for evolutionary multi-objective optimization [educational forum]," *IEEE Computational Intelligence Magazine*, vol. 12, no. 4, pp. 73–87, 2017.

[35] S. N. Lophaven, H. B. Nielsen, J. Søndergaard, *et al.*, *DACE: a Matlab kriging toolbox*, vol. 2. Citeseer, 2002.

[36] J. Schrass, J. Cate, J. Dean, and D. J. Hartl, "Mixed reality wind tunnel visualizations," in *AIAA AVIATION 2022 Forum*, p. 3494, 2022.

[37] "Passthrough api: Oculus developers." https://developer.oculus.com/experimental/passthrough-api/, 2021.

[38] "Render baking." https://docs.blender.org/manual/en/latest/render/cycles/baking.html, May 2022.

[39] D. S. Lacy and A. J. Sclafani, "Development of the high lift common research model (hl-crm): A representative high lift configuration for transonic transports," in *54th AIAA Aerospace Sciences Meeting*, p. 0308, 2016.

[40] F. Auricchio, R. L. Taylor, and J. Lubliner, "Shape-memory alloys: macromodelling and numerical simulations of the superelastic behavior," *Computer Methods in Applied Mechanics and Engineering*, vol. 146, no. 3, pp. 281–312, 1997.

[41] "scipy.optimize.minimize." `https://docs.scipy.org/doc/scipy/reference/generated/scipy.optimize.minimize.html`, 2008.

[42] J. Blank and K. Deb, "Pymoo: Multi-objective optimization in python," *IEEE Access*, vol. 8, pp. 89497–89509, 2020.

[43] K. Deb, K. Sindhya, and T. Okabe, "Self-adaptive simulated binary crossover for real-parameter optimization," in *Proceedings of the 9th Annual Conference on Genetic and Evolutionary Computation*, GECCO '07, (New York, NY, USA), p. 1187–1194, Association for Computing Machinery, 2007.

[44] R. Dougherty, *BeamformX Reference Manual. OptiNav Inc.*, 2018.

7. Wing Fixed Mechanism Stowed Preliminary Design and Optimization

This appendix presents the process by which a potential design for a leading-edge slat gap filler (SGF) was created and optimized. This process was completed as part of the MEEN 683 - Multidisciplinary System Analysis and Design Optimization at Texas A&M University. This design is most similar to the Wing Fixed Mechanism Stowed SGF. Herein are presented the results of a design of experiment study, two single objective optimizations, and a multi-objective optimization executing using the NSGA-II algorithm. This cycle of design and optimization revealed potential improvements to the simulation model that could result in a more realistic and applicable final design. Nonetheless, the optimization resulted in a converged final model that could be manufactured for experimental testing.

7.1 Problem Formulation

The design used in this optimization is inspired by the design proposed by Turner et al., shown in Fig. 7.1. Specifically, the design herein is similar to the "Stress-free-deployed" case, in which the SGF is modeled to be at an initial state with the slat fully deployed [9]. In this paper, Turner suggests use of a shape memory alloy (SMA) as the material for the SGF because SMA superelastic properties allow for large, restorable deformations without yielding. These material properties allow the SGF to deform into an ideal aeroacoustic shape. Perhaps more importantly, a SMA SGF provides the potential for these desired shapes to be achieved on a real wing with sweep and variable chord [9].

For this design and optimization problem, the stress-free-deployed design is modified so that the SGF is initialized at a state above the slat. After assembling the structure, this results in a restoring force exerted on the SGF that keeps it attached to the slat as the slat cycles from a retracted to a deployed state. Additionally, the SGF is modeled with an out-of-plane depth of one unit using symmetry conditions to simplify structural and flow simulations. To improve runtime, only nearfield flow calculations are computed, and the noise is propagated to a distance of 1.5 m

(based on the intended experimental setup [8]). The experimental parameters also set the scale for the NASA Common Research Model (CRM) wing [39], used to simulate a transportation class aircraft, at 6.25%. This scale corresponds to a stowed wing chord of 0.32 m and span of 1.22 m. The slat used in the simulation model is slightly modified from the CRM slat to facilitate attachment of the SGF. An example of the CRM model used in the optimization is shown in Fig. 7.2.

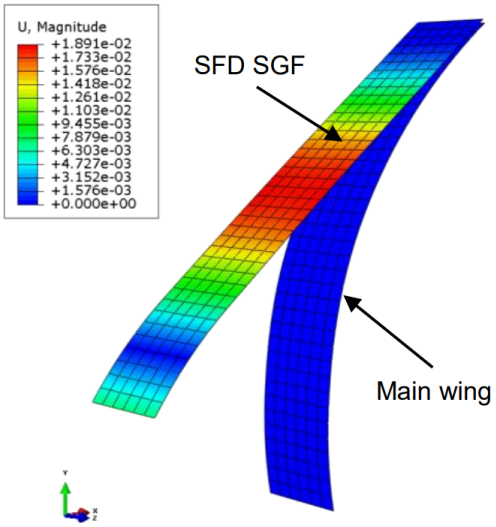

Figure 7.1: Stress-free-deployed SGF from [9].

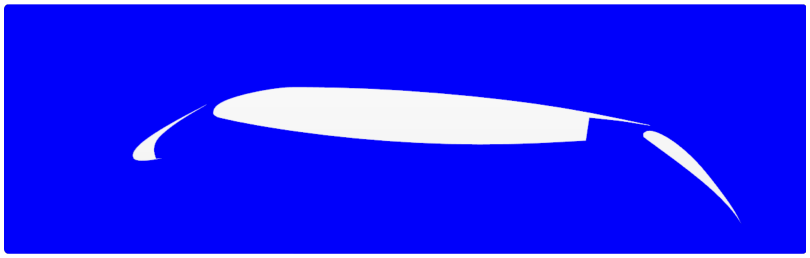

Figure 7.2: Example CRM wing geometry used in the optimization.

As stated, the minimization objectives for this optimization are mass and noise. Mass is simply calculated using the geometry of the SGF and the density of the material selection. Noise is calculated using a Fast Fourier Transform (FFT) on pressure data at the receiver point over a brief period of time. The pressures at the receiving point are calculated using the Ffowcs-Williams and Hawkings (FW-H) formulation in Star-CCM+ to propagate the nearfield pressures found using computational flow dynamics (CFD). These pressures are converted to SPL and OASPL for the noise objective value.

There are two constraints implemented in the optimization. The first constraint is an equality constraint that checks if the SGF is attached to the slat in its deformed configuration under a pressure load. The second constraint is an inequality constraint that requires the maximum stress in the SGF at every point in the assembly, deployment, and loading simulation steps to be less than the yielding stress of the material.

The design variables considered for this optimization problem can be split into two categories: the shape variables that describe the undeformed SGF geometry, and the flow variables that describe the flow conditions. The shape variables considered are length, thickness, attachment angle, attachment location, and material. These design variables are labeled in Fig. 7.4. The three materials considered are Nitinol, a SMA following from the suggestion by Turner, Aluminium 6061, and Titanium Ti-6Al-4V. Simulation of a superelastic SMA is executed in Abaqus by the native Arruchio model [24],[40] which accurately describes the austinite-martensite phase transformation that gives a SMA its unique properties. The material and attachment location design variables are defined as discrete design variables in the optimization framework with integer values corresponding to each option. The attachment locations are very precise values such that the selected attachment point is guaranteed to lie along the spline defining the leading edge of the main wing. The attachment location options are shown in Table 7.1, and the material properties are shown in Table 7.2.

For this optimization, only the velocity is considered as a flow variable, but future optimizations could expand this to include other relevant variables like the location of the sound receiver.

Design Variable Mapping	Attachment Location (mm, mm)
0	(-18.150576920157107, -1.7043697649327)
1	(-25.741118254157115, -2.537683566932701)
2	(-37.62901573815711, -5.1039606289327)
3	(-40.0, -5.77717534350906)
4	(-51.13497399415709, -9.3370128689327)
5	(-63.53388010815708, -14.8356932609327)

Table 7.1: Possible attachment locations and their corresponding design variable values.

	Design Variable Mapping	Density (g/cm^3)	Young's Modulus (GPa)	Poisson's Ratio	Yield Stress (MPa)
Nitinol*	0	6.45	48.9	0.33	690
Ti-6Al-4v	1	4.41	111	0.33	924
Al 6061	2	2.70	68.9	0.33	241

Table 7.2: Material properties. Note: Nitinol* properties listed are Austenite properties.

Velocity ranges are used to determine the pressure force applied to the structural model to obtain the deformed shape. The velocity is also used as an input to the CFD solver.

The parameters for simulating the SGF described by these design variables are the applied pressure forces and the material properties. Specifically, a pressure load of 100 Pa is applied to the structural model of the SGF if the velocity is below 20 m/s, and a pressure load of 200 Pa is applied if the velocity is above 20 m/s. These approximate values were determined by examining the CFD flow solution in the case without the SGF. Improving the fidelity and accuracy of the pressure paramaterization beyond this simple implementation is one area where the simulation could be improved in the future. Also, the key material parameters are the density, Young's modulus, Poisson's ratio, and yielding stress of each material. These are shown in Table 7.2.

The design variables (x), objective variables (J), inequality constraints (g), and equality constraints (h) are defined in Eqs. 7.1,7.2,7.3, and 7.4, respectively. They are written together as an optimization problem in Eq. 7.5. The relationships between the input and output variables are displayed in a N^2 diagram in Fig. 7.3 showing their relationships. The locations of the design variables are shown in Fig. 7.4.

$$x = \begin{bmatrix} l \\ t \\ a \\ \theta \\ m \\ v \end{bmatrix} = \begin{bmatrix} \text{length} \\ \text{thickness} \\ \text{attach location} \\ \text{attach angle} \\ \text{material properties} \\ \text{velocity} \end{bmatrix} \tag{7.1}$$

$$J = \begin{bmatrix} M \\ N \end{bmatrix} = \begin{bmatrix} \text{mass} \\ \text{OASPL} \end{bmatrix} \tag{7.2}$$

$$g = \begin{bmatrix} \sigma - \sigma_y \end{bmatrix} = \begin{bmatrix} (\text{max von Mises stress}) - (\text{yield stress}) \end{bmatrix} \tag{7.3}$$

$$h = \begin{bmatrix} A \end{bmatrix} = \begin{bmatrix} \text{SGF Slat attachment} \end{bmatrix} \tag{7.4}$$

$$\begin{aligned} \min_{x} \quad & J(x) \\ & lb \leq x \leq ub \\ \text{s.t.} \quad & g(x) \leq 0 \\ & h(x) = \text{True} \end{aligned} \tag{7.5}$$

7.2 Physical Models and Benchmarking

Aeroacoustic noise solutions provided by Star-CCM+ can be scaled to match the size of the target experimental model using the procedure in [29]. There is an approximate 10-20 dB difference between the simulated noise and the experimental noise found in [8], but this can be attributed to a number of factors including the noise of the wind tunnel in the experimental measurements and errors coming form the small domain used in the CFD simulations. The nearfield CFD simulation is modeled using a Direct Eddy Simulation with a k-ω turbulence model. The FW-H model is applied to this solution to calculate acoustic pressures at a far-field receiver. All of these methods

In	L,t,a,θ,m	L,t,a,θ,m	V	V		
	Shape Generation		Shape			
		Mass Calculation				Mass
			Structural Solver	Deformed Shape		Maximum Stress, Attachment
				Acoustic CFD	SPL	
					Noise Calculation	OASPL
						Out

Figure 7.3: N^2 Diagram of design variables, intermediate variables, and calculations.

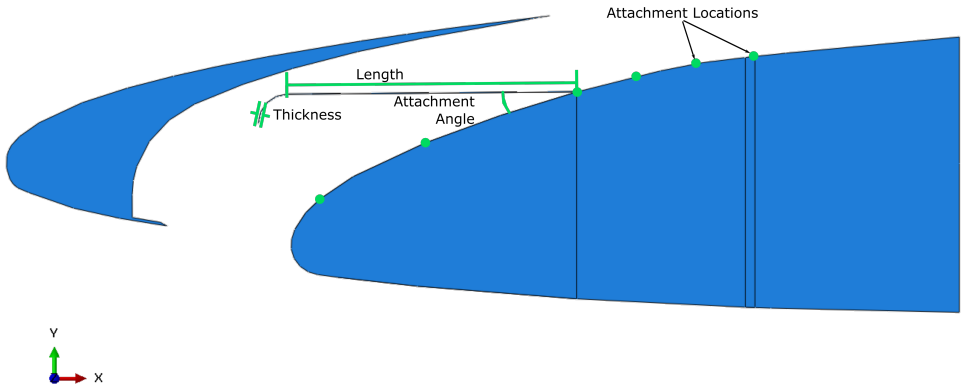

Figure 7.4: Diagram depicting locations for each design variable for an example SGF on the leading edge of the CRM.

have been tested and are suitable to simulate the SGF-wing body.

Abaqus FEA and Star-CCM+ represent the multidisciplinary aspect of this optimization problem by simulating the structural response of a part, and the flow response to a deformed body, respectively. The physical models implemented also add significant complexity to the optimization problem. The high accuracy required for commercial codes results in a optimization framework that can change dramatically due to small changes in the design variables. Unfortunately, this high

accuracy also results in high simulation runtimes of about 5 minutes per objective function run using 20 computational cores. Also, the simulation of sliding contact between the SGF and the slat during slat deployment is very difficult, meaning that some design variable inputs can cause the structural analysis to fail. Therefore, several tuning iterations were required to define a problem that would allow the objective to always or almost always be calculated. Also, dummy values for the objectives are implemented in the optimization framework to protect against the case of a failed simulation while minimally affecting the optimization process.

7.3 Design and Optimization

A design of experiment (DOE) study, two single objective optimization algorithms, and a final multi-objective optimization algorithm were used to find a set of solutions describing the ideal shape of a SGF. A block diagram demonstrating an iteration of the objective function used in all algorithms is shown in Fig. 7.5.

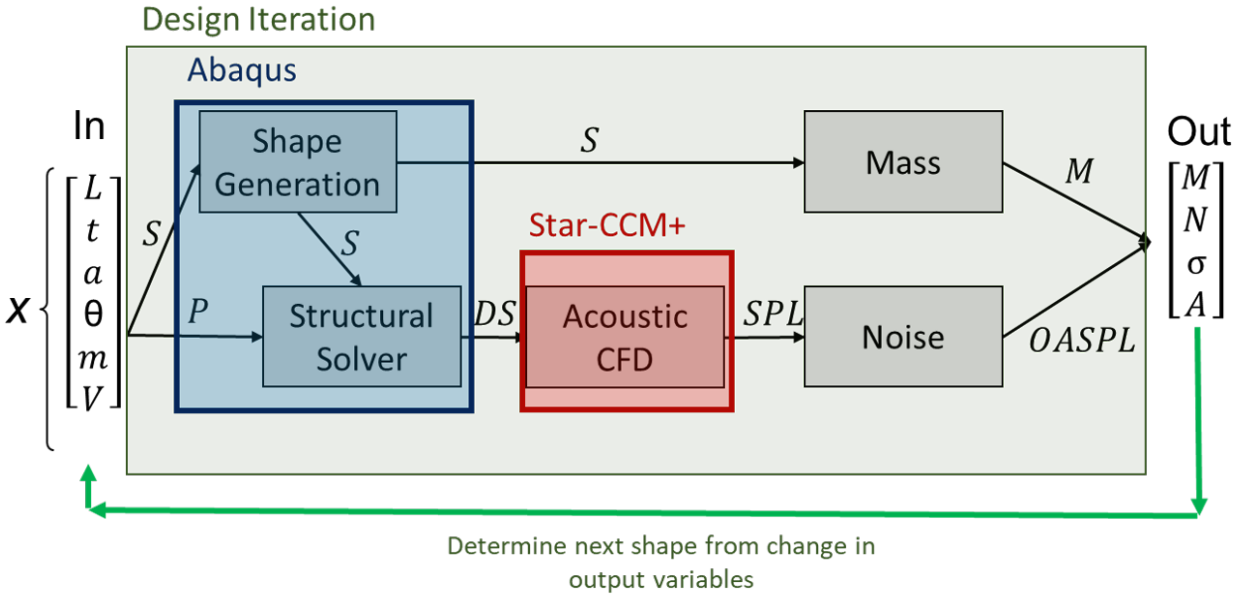

Figure 7.5: Block diagram of a design iteration.

7.3.1 Design of Experiment

A DOE study was executed to discern the bounds of the design space and the effect of certain variables. To achieve this, a 10 individual latin hypercube sample (LHC) of the design space was taken, and each design was simulated with the objective function. The results of this study are shown in Fig. 7.6. (In reality, many DOE runs were attempted, over which the design variable bounds were adjusted to their final values, which are shown in Eq. 7.6 and used in the presented LHC study). This scatterplot demonstrates that the design space can be used to find a variety of solutions in the objective space, and it reveals an initial estimate of the Pareto frontier that is the goal of the multi-objective optimization. Also, this plot demonstrates that the constraints can become active and will affect the final solution.

$$\begin{bmatrix} l \\ t \\ a \\ \theta \\ m \\ v \end{bmatrix} = \begin{bmatrix} 70.0 - 74.0 \text{ mm} \\ 0.05 - 0.10 \text{ mm} \\ 0 - 5 \\ 0.0 - 8.0 \text{ deg} \\ 0 - 2 \\ 15.0 - 25.0 \text{ m/s} \end{bmatrix} \tag{7.6}$$

7.3.2 Single Objective Optimization

7.3.2.1 Simplex Algorithm

Two single objective optimizations were executed to investigate the properties of this optimization problem. First, a Constrained Optimization BY Linear Approximation (COBYLA) algorithm was implemented using the Scipy.optimize Python library [41]. This algorithm was chosen because it allows for implementation of bounds and constraints, and because it does not require calculation of the gradient at each iteration, which would be too computationally expensive given the long objective function runtime. Instead, it uses a constrained simplex method to find the next solution. This optimization was run to minimize the single objective of mass of the SGF for 20

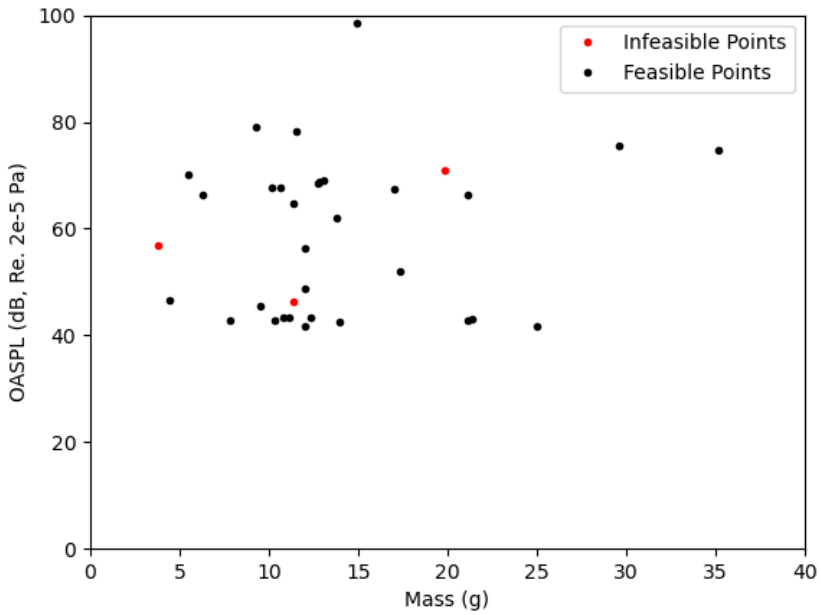

Figure 7.6: Results of LHC experimental design study plotted in objective space.

iterations. This algorithm was run for a relatively few number of iterations because the physics model complexity results in a very long runtime per objective function calculation. While minimization of mass can be calculated by hand, this algorithm considers the attachment and yielding constraints that cannot be calculated easily for this complex system. Additionally, the sensitivity of each continuous variable with respect to the mass objective can be calculated, resulting in the chart shown in Fig. 7.7. Unfortunately, this chart does not provide much information because it appears that Abaqus run failed or violated constraints for the angle and velocity perturbation runs in the calculation of the finite difference of the objective. However, the chart does demonstrate that the objective is about twice as sensitive to small changes in length compared to small changes in thickness, and that changing either length or thickness by a small amount has an acceptable affect on the objective value.

The second derivatives were calculated along the diagonal of the Hessian matrix to evaluate the need for scaling, and all derivatives were evaluated to a value near 10^3, demonstrating the need for scaling to be applied to the problem. The scaling method is discussed in the Multi-

Objective Optimization section. Also, the change in the objective function with respect to the density parameter was calculated and resulted in a normalized 1.5% change, which is of a similar magnitude to the change caused by perturbations in the thickness and length design variables. This emphasizes that density is an important parameter and, therefore, material selection is an important design variable, even though sensitivity analysis was not preformed for the discrete material selection variable.

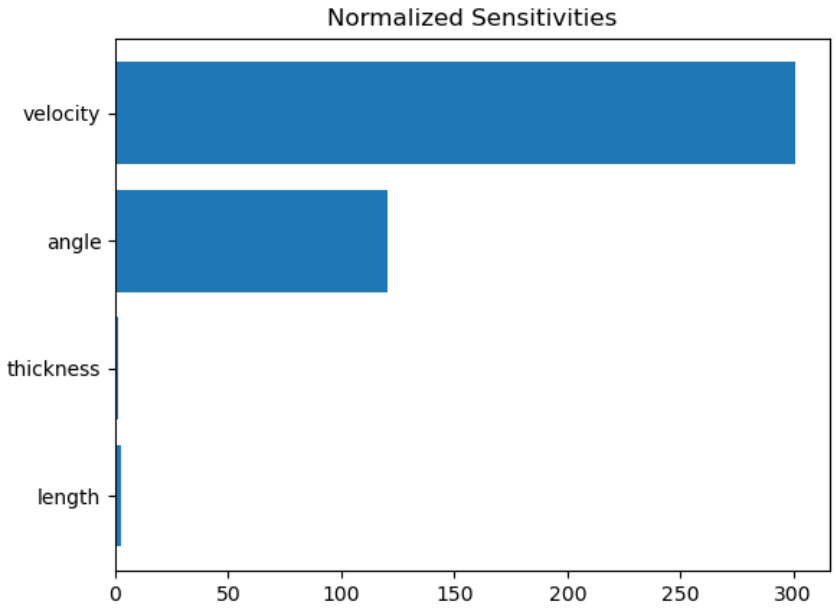

Figure 7.7: Tornado chart depicting the normalized effect of changing each variable a small amount on the objective.

The results of the COBYLA algorithm are shown in Table 7.3. These results show that the algorithm had not converged after 20 iterations, and that the constraints were not satisfied by a small amount. Note that the attachment location and material design variables were rounded to the nearest integer.

Objective Variables		Design Variables					
Mass (g)	**OASPL (dB)**	**Length (mm)**	**Thickness (mm)**	**Attachment Location**	**Attachment Angle (\deg)**	**Material**	**Velocity (m/s)**
6.8494	NA	72.0269	0.0499	4	6.0039	Al 6061	15.0000

Table 7.3: COBYLA algorithm objective and design vector results.

7.3.2.2 Genetic Algorithm

While a simplex-based algorithm is useful for comparisons, this optimization problem is better suited to a heuristic algorithm for a number of reasons. First, heuristic algorithms can be used to implement discrete variables, like the material and attachment location, without needing to map these variables to rounded numeric values. Secondly, the objective space is very nonlinear and can even be discontinuous in some areas due to the complexity issues in the structural simulation. For this problem, a genetic algorithm (GA) was chosen to serve as the heuristic algorithm because this type of algorithm is robust and can be used effectively with discrete variables. The GA was implemented using the Pymoo python library [42]. The population size of the GA was 10 individuals, and it was run for 5 iterations. Random sampling was used to generate the population, and the simulated binary method was used for crossover of population members. The simulated binary method allows the algorithm to act as if the design variables were mapped to binary values without needing to perform this mapping manually, resulting in a more effective and efficient algorithm [43]. The crossover probability was set to 0.9, and the η value used for the distribution of the simulated binary function was 15.0. The mutation function implemented in this GA uses the same probability function as in the binary crossover, but an η value of 9.0 was used for mutation, resulting in fewer mutations compared to variable crossovers. The results of the GA are shown in Table 7.4. The GA was run to optimize the noise objective instead of the mass objective, so it cannot be directly compared to the COBYLA algorithm. However, the evolution of the GA, as shown by the decreasing objective in Fig. 7.8 suggests that this class of algorithm performs well for this design problem.

Objective Variables		Design Variables					
Mass (g)	OASPL (dB)	Length (mm)	Thickness (mm)	Attachment Location	Attachment Angle (\deg)	Material	Velocity (m/s)
NA	41.8730	73.5801	0.0622	3	5.3771	Ti-6Al-4v	15.0320

Table 7.4: Genetic algorithm design vector results.

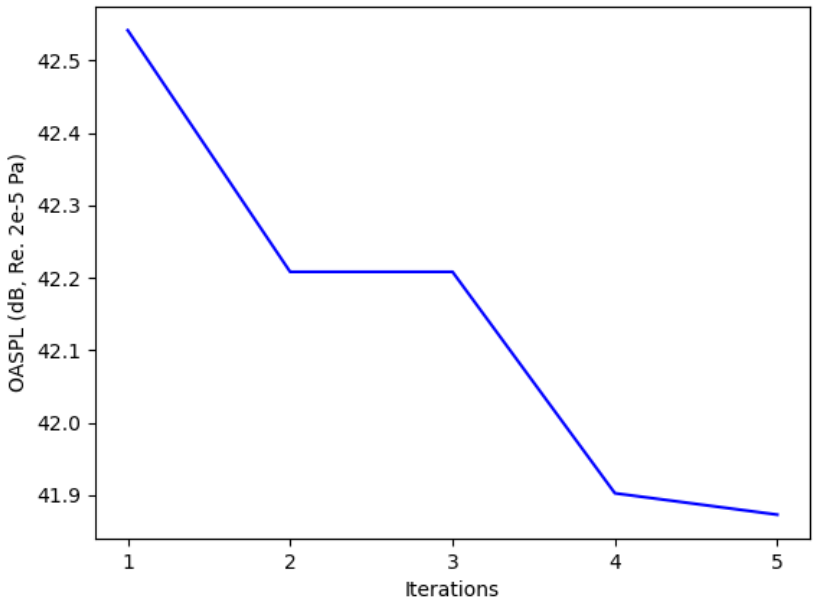

Figure 7.8: Genetic algorithm objective versus iteration plot to demonstrate design evolution.

7.3.3 Multi-Objective Optimization

A heuristic algorithm was selected for the multi-objective optimization due to the nonlinearity of the problem and the presence of discrete design variables, as discussed in the Genetic Algorithm section. For similar reasons, another type of genetic algorithm was selected for the multi-objective optimization algorithm in the NSGA-II algorithm. This algorithm, as implemented in Pymoo, uses a modified mating and selection algorithm compared to the single-objective GA to ensure the Pareto frontier is non-dominated. Also, this algorithm uses a tournament mating selection procedure instead of the random selection used in the GA [42]. Since the GA performed well, the coefficients and function selections for sampling, crossover, and mutation were set to the same val-

ues as in the GA. This algorithm used a population of 20 individuals and was run for 20 iterations.

To achieve reasonable convergence characteristics in the NSGA-II algorithm, the design variables, constraints, and objectives are scaled to be of similar magnitudes. For these reasons, the length design variable was reduced by a factor of 10, and the thickness design variable was increased by a factor of 100 in the view of the algorithm. Also, the mass and noise objectives were scaled to the size of the experimental model using the span value of 1.2192 meters. (The scaling procedure for noise is discussed above and in [29]). These changes made the mass in grams and the loudness in dB the same order of magnitude as the yield stress constraint, given in MPa. Also, the binary equality constraint of attachment to the slat was mapped to an inequality constraint and given values of similar magnitude to the other constraint and objectives. The independent minimum values of each objective are plotted against the number of iterations in Fig. 7.9 to demonstrate the evolution of the algorithm towards a steady state solution. The flatlining of the objective variables after about 10 iterations suggests that the algorithm has found a Pareto set of minimum values.

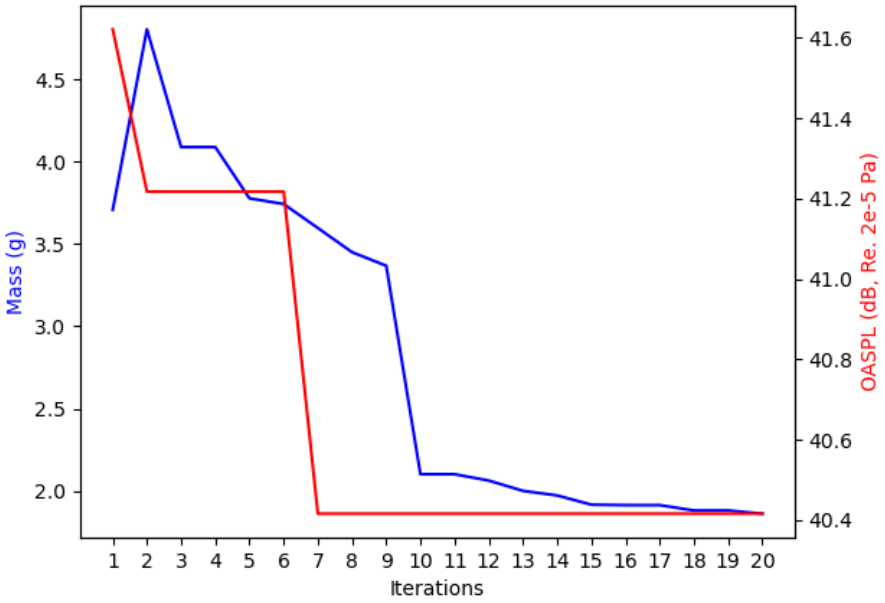

Figure 7.9: Minimum objective values at each iteration versus number of iterations.

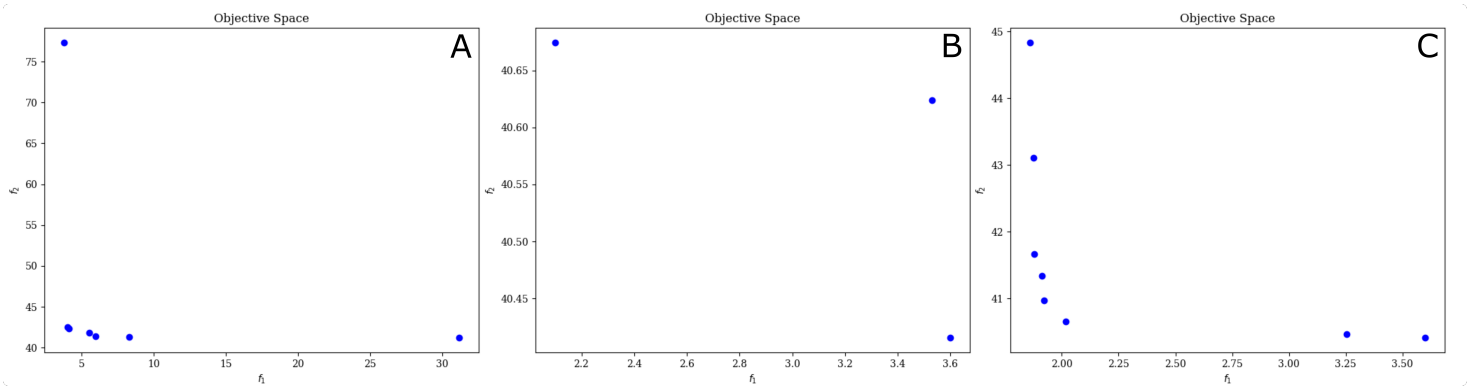

Figure 7.10: Resulting Pareto frontier of multi-objective optimization after 5 iterations (A), 10 iterations (B), and 20 iterations (C) where f_1 is mass and f_2 is OASPL.

7.4 Results

The listing of design variables for the Pareto points after 20 iterations in Table 7.5 shows that the algorithm is moving the design vector towards a few bounds. First, the velocity is being minimized. This result probably occurs because noise generally increases with velocity and it means that the algorithm found no benefit to the additional deformation caused by higher pressures. This result could change however if a more precise method is used for pressure load parameterization. Secondly, the results of this optimization suggest that a SMA is not necessary to achieve deformations required for a SGF. This result is important, but it also highlights the drawbacks of simulating a SGF with out-of-plane symmetry conditions. Real aircraft wings have sweep and variable chord, and these unsimulated characteristics could cause increased strains that require a SMA. Additionally, it is possible that, since simulating a superelastic SMA is more complex than a standard material, simulations of some design vectors containing the SMA material failed in the structural simulation phase. If this behavior happened, the objective values would have been set to their failsafe values, and the algorithm might move away from designs with the SMA material selected. Thirdly, while all attachment angles in the set of optimum points are small, there is no clear result as to the best angle, suggesting that the ideal angle depends on other factors like length and thickness. Finally, the attachment location has evolved to be the closest position to the slat

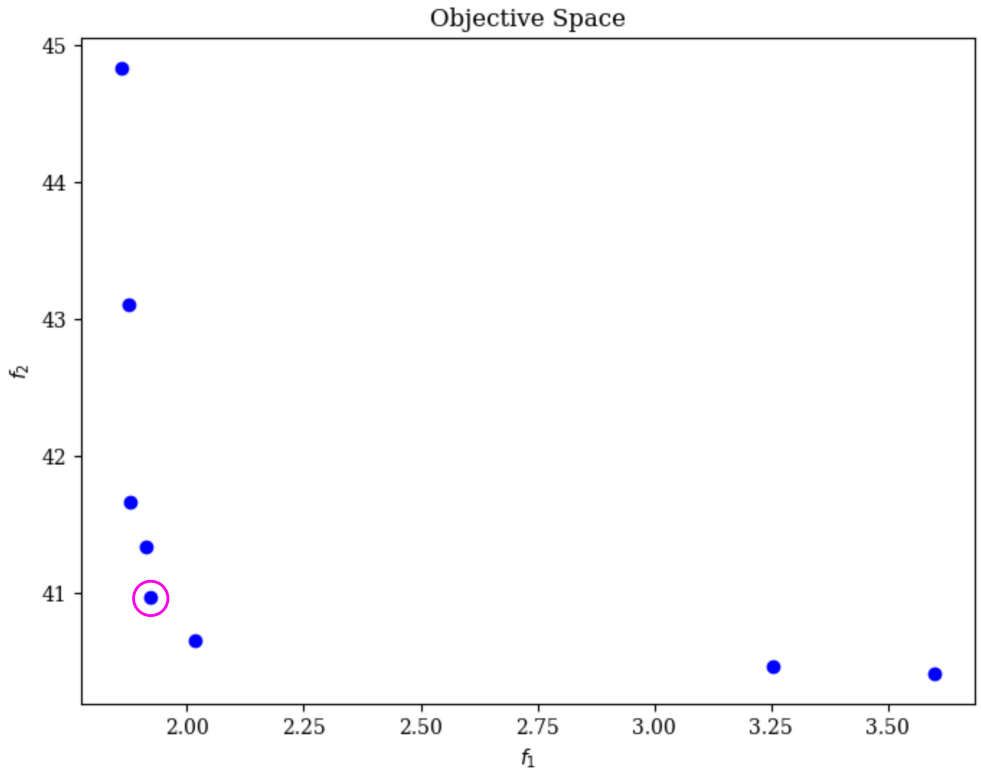

Figure 7.11: Resulting Pareto frontier of multi-objective optimization after 20 iterations where f_1 is mass and f_2 is OASPL. Simulation results are shown in other figures for the highlighted point.

and the length approaches its lower bound for all optimum points. This results in the shortest SGF and therefore the lowest mass. Despite this apparent simplicity, this is one of the most important optimization results because it suggests that the noise reduction properties of this type of SGF are not inhibited by its length or its vertical position relative to the slat.

The Pareto frontier of the optimization after 5 iterations, 10 iterations, and 20 iterations is shown in Fig. 7.10. The number of points on the Pareto frontier decreases initially but then increases as the algorithm attempts to find more points on the frontier. The final Pareto frontier, shown in Fig. 7.11, suggests that there are important tradeoffs between the mass of the SGF and the noise produced by the SGF, as the lowest mass points do not correspond to the lowest noise points. Another tradeoff emphasized by the final Pareto frontier is shown by the gap in points along

Objective Variables		Design Variables					
Mass (g)	OASPL (dB)	Length (mm)	Thickness (mm)	Attachment Location	Attachment Angle (\deg)	Material	Velocity (m/s)
3.5983	40.4155	70.7191	0.0565	5	3.9646	Ti-6Al-4v	16.5090
3.2522	40.4699	70.0023	0.0537	5	1.2212	Ti-6Al-4v	16.4995
1.9232	40.9687	70.2178	0.0509	5	0.4866	Al 6061	16.5764
1.8803	41.6630	70.1307	0.0502	5	0.4218	Al 6061	18.0846
2.0172	40.6522	70.7096	0.0514	5	1.0029	Al 6061	16.5336
1.9127	41.3426	70.2549	0.0505	5	0.4215	Al 6061	15.7621
1.8608	44.8330	70.1390	0.0503	5	3.2036	Al 6061	18.1196
1.8751	43.1069	70.0601	0.0503	5	0.1010	Al 6061	17.2348

Table 7.5: Optimal points plotted in final Pareto frontier.

the mass objective axis. This gap corresponds to a switch from the lowest density aluminium material to the higher density titanium material, and it suggests that there are deformed structures beneficial to noise reduction that require a stiffer material like titanium.

The existence of concave points on the frontier suggests that the choice of a heuristic multi-objective optimizer was necessary, otherwise the non-convex point may not have been found. The results of the Abaqus and Star-CCM+ simulations for the highlighted point on the Pareto frontier are shown in Fig. 7.12.

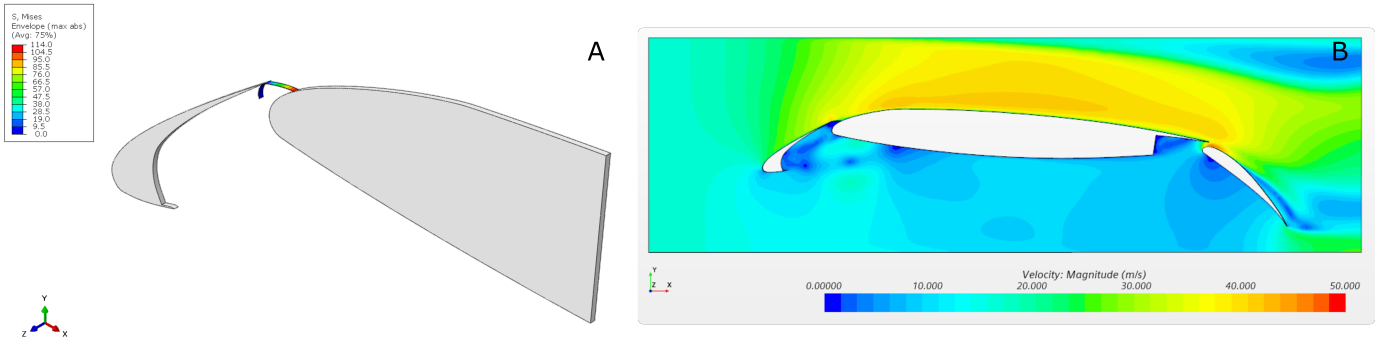

Figure 7.12: Abaqus FEA results (A) and Star-CCM+ CFD results (B) of the highlighted point on the optimized Pareto frontier.

7.5 Discussion

The optimization was successful in that it obtained a set of designs that are physically feasible in the targeted experimental setting. Also, the multi-objective optimization succeeded in finding

several non-dominated points and forming a Pareto frontier, and the results of the optimization procedure suggest that the algorithm converged to optimum points. The use of a heuristic algorithm with a relatively large population size and number of iterations provides confidence that the optimal points are close to the global optimum points. The optimization resulted in a set of design vectors with clear characteristics that can be applied to production of an experimental SGF including the preferred material, thickness, and attachment location.

However, the optimization procedure also revealed that future improvements to the optimization framework like including the effects of wing sweep, increasing the size of the CFD fluid domain, and improving the robustness of the structural solver could push the optimization result toward solutions that are more applicable to full-scale test cases. These improvements could reveal the benefits of the SMA material that were not apparent in this optimization framework. Despite these shortcomings, the optimization procedure successfully minimized the mass of the SGF and minimized noise coming from the wing with the SGF applied without violating any constraints or design bounds, providing useful information for future SGF designs and experimental testing.

8. Experimental Analysis of Non-Morphing Slat Gap Filler Noise Reduction Concepts*

In a previous experimental work by Mu et. al., multiple non-morphing slat gap filler concepts were investigated by conducting aeroacoustic and aerodynamic experiments on a scaled high-lift wing model [11]. These concepts were compared to an untreated wing to identify the noise reduction potential of the SGF concept.

8.1 Experimental Test Setup

8.1.1 The Wing

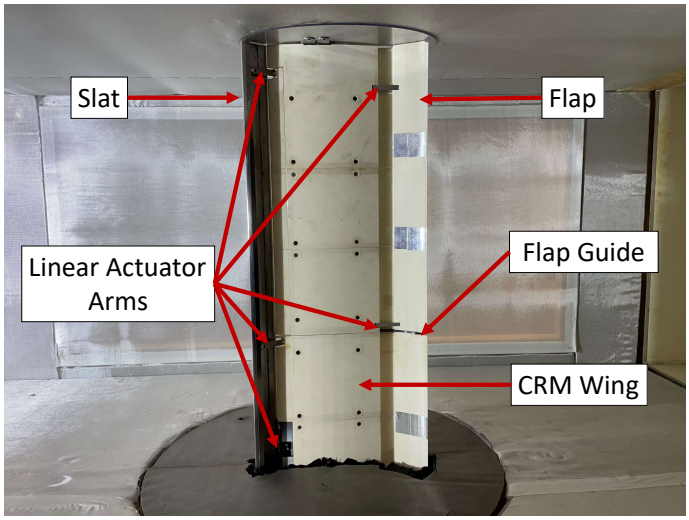

Figure 8.1: 1/16th scale HL-CRM wing

A spanwise uniform wing model at 1/16th scale was developed from a freestream parallel cross section at the midspan of the HL-CRM, as seen in Fig. 8.1. The wing model is shown mounted

*Parts of this appendix were from "Aerodynamic and Aeroacoustic Experimentation of a Slat-Gap Filler for Airframe Noise Reduction" by Mu, M., Schrass, J., Lieb, K., and Hartl, D.; reprinted by permission of the American Institute of Aeronautics and Astronautics, Inc.

vertically in the 4 ft. by 3 ft. wind tunnel at Texas A&M University. Two SGF concepts were applied to close the gap between the slat and the main wing. The concepts were fabricated for the 100% deployed configuration for the slat. For all tests, the high-lift devices were deployed symmetrically with the assistance of guides at each end of the wing.

Tests were conducted with and without the SGF treatments to the wing model while measuring aerodynamic and aeroacoustic performance. A slat and flap deployment level of 100% was chosen for acoustic and aerodynamic testing at freestream velocities of 15 m/s and 25 m/s and angles of attack between -4° to 20° to simulate flight conditions during approach and landing.

8.1.2 Slat Gap Filler Concepts

Two SGF concepts were fabricated to be tested. The Aluminum Shape Set SGF, 3D printed ABS SGF, and the slat configuration with no addition will be referred to as the "Stepped SGF", "Conformal SGF", and "untreated" slat respectively in this the appendix. Fig. 8.2a depicts the Stepped SGF in which the pressure-side of the leading edge of the wing is connected to the trailing edge of the slat. The Stepped SGF was fabricated by forming a 0.010 in. (0.0254 cm.) aluminum shim with a custom mold tool and was attached to the wing with polyester pressure-sensitive adhesive.

Fig. 8.2b depicts the Conformal SGF which connects the suction-side of the leading edge of the wing to the trailing edge of the slat. The Conformal SGF was fabricated using 3D printed ABS plastic and attached to the wing with polyester pressure-sensitive adhesive. This concept represents a continuous transition between the slat trailing edge and main wing on the suction side of the wing and was inspired by previous concepts [9]. Preliminary tests conducted with adhesive-backed rolled aluminum sheet also demonstrated the potential effectiveness of this SGF shape. Early wind tunnel tests suggested that this SGF concept decreased overall wing noise and minimally affected wing aerodynamics compared to the untreated wing. A more rigid method using 3D printed ABS was chosen to minimize deflection under aerodynamic load and application variability. These concepts represent different airframe implementations and was intended to explore the sensitivity of the aerodynamic and aeroacoustic performance to the shape presented by the SGF to the flow.

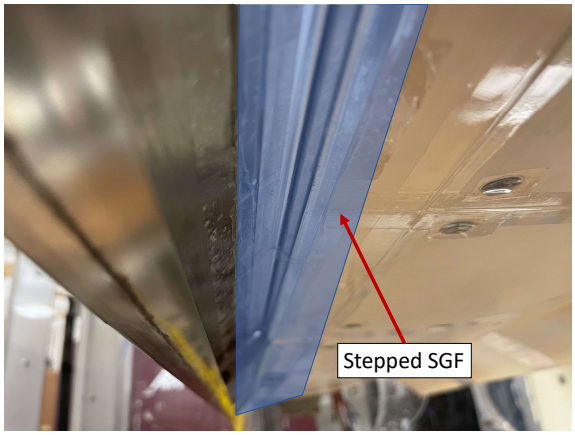

(a) Stepped SGF installed on 1/16th scale HL-CRM wing

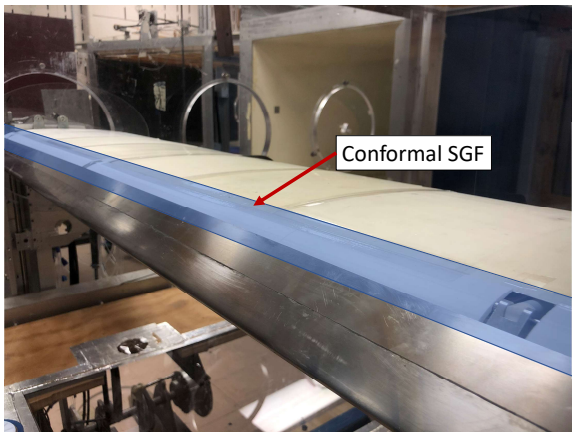

(b) Conformal SGF installed on 1/16th scale HL-CRM wing

Figure 8.2: SGF concepts

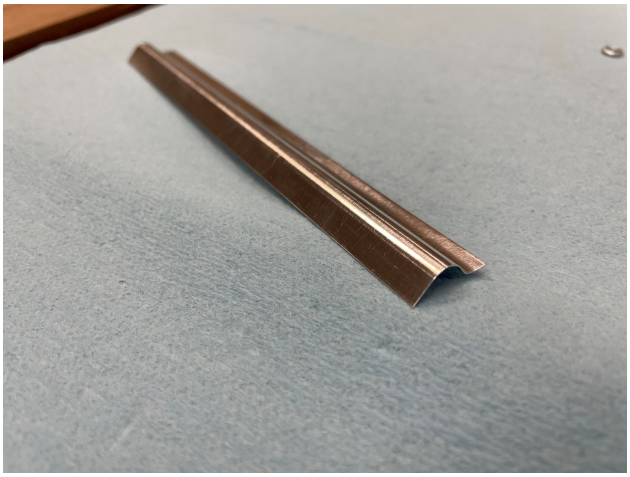

(a) Stepped model

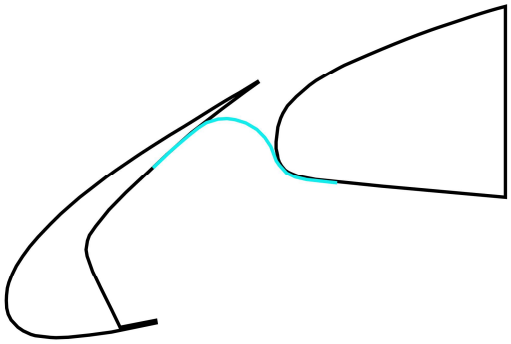

(b) Stepped schematic

Figure 8.3: Individual SGF concepts

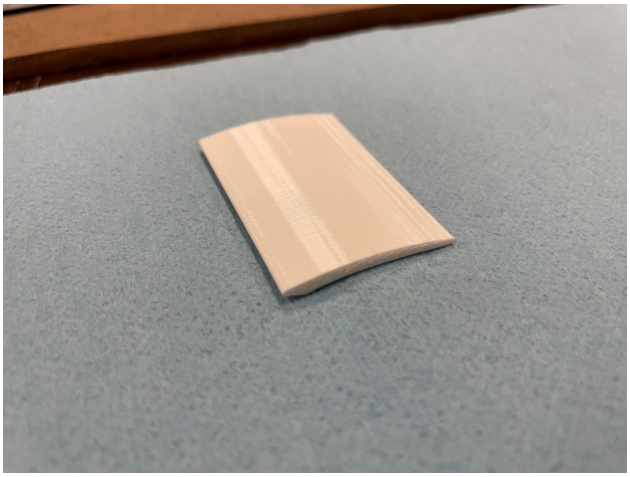

(c) Conformal model

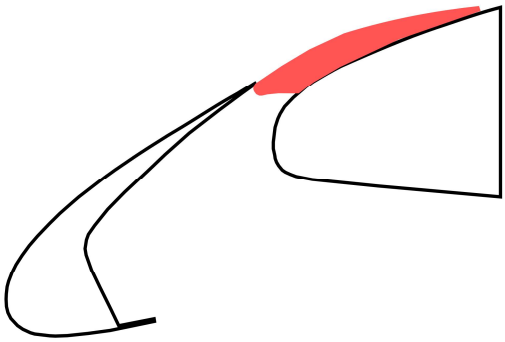

(d) Conformal schematic

Figure 8.3: Individual SGF concepts

8.1.2.1 High Strength Adhesive SGF

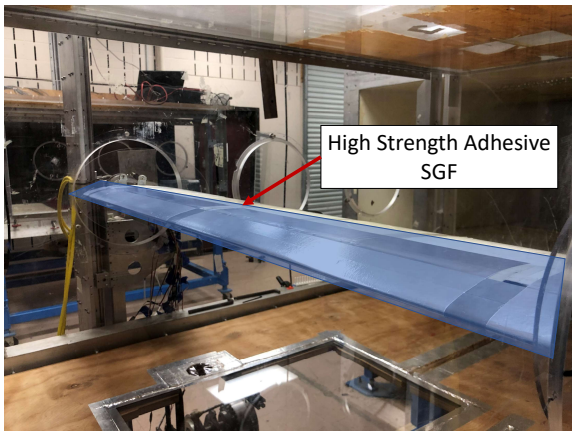

(a) High strength adhesive SGF installed on 1/16th scale CRM wing

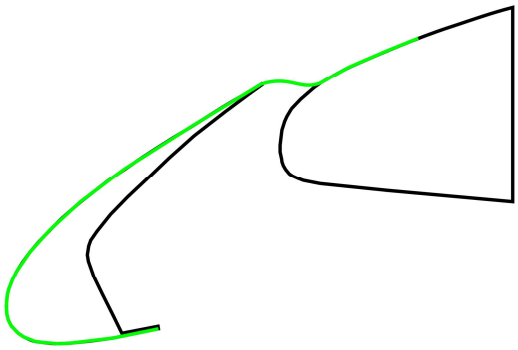

(b) High strength adhesive SGF graphic

Figure 8.4: Preliminary SGF concept utilizing high strength adhesive

The SGF utilizing high strength adhesive was used for preliminary wind tunnel tests. This was done to better understand of the effects the SGF has on a wing prior to implementing the other concepts concepts.

8.1.3 Wind Tunnel Configuration

Aeroacoustic tests were conducted in the acoustically treated test section shown in Fig. 8.5a. A schematic of the acoustic test section in planform view is shown in Fig. 8.5b. Aerodynamic tests were performed with the wing model oriented horizontally in the aerodynamic test section, as shown in Fig. 8.6. Wind tunnel freestream velocity was controlled with a variable-RPM motor.

8.1.4 Aeroacoustic Test Section Wind Tunnel Configuration

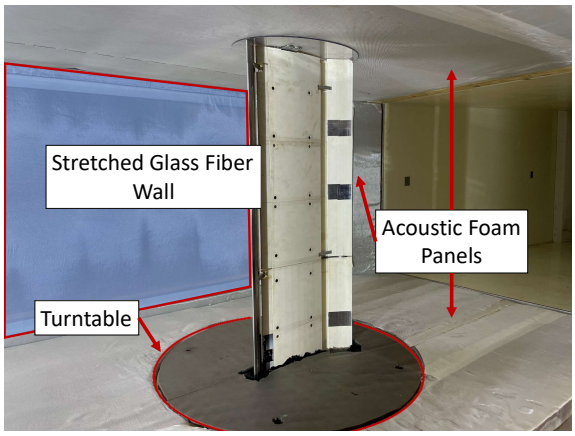

(a) 1/16th scale HL-CRM wing in acoustic test section

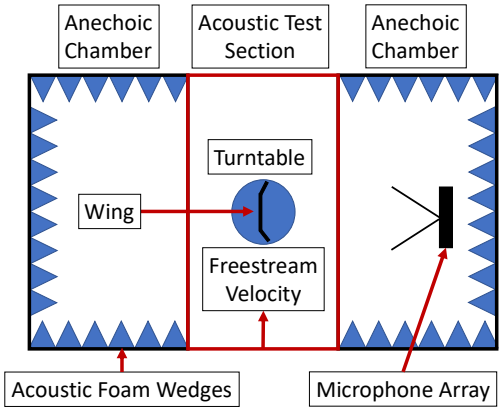

(b) Diagram of acoustic test section

Figure 8.5: Acoustic wind tunnel section

Aeroacoustic testing was conducted using the wind tunnel acoustic test section (Fig. 8.5a) enclosed by two anechoic chambers as seen in Fig. 8.5b. The acoustic test section is fitted with stretched glass fiber meshing to contain the flow and both anechoic chambers are treated with acoustic foam panels to reduce external acoustic influence and internal reflection. A Signal Interface Group ACAM 120 microphone array installed within one of the anechoic chambers was used to measure acoustic perturbations emanating from the HL-CRM wing. The arrangement of microphones on the array allows for spatial characterization of acoustic sources with beamforming [8]. Angle of attack was controlled with a rotational motor, connected to the wing from the bottom of the acoustic test section. The OptiNav Inc. BeamFormX program was used to collect and process the noise data from the microphone array [44]. Noise data at varying angles of attack and at freestream velocities of 15 m/s and 25 m/s was collected and processed to produce spectral sound pressure level (SPL) plots, overall sound pressure level (OASPL) plots, and images depicting noise sources at their respective frequencies.

8.1.5 Aerodynamic Test Section Wind Tunnel Configuration

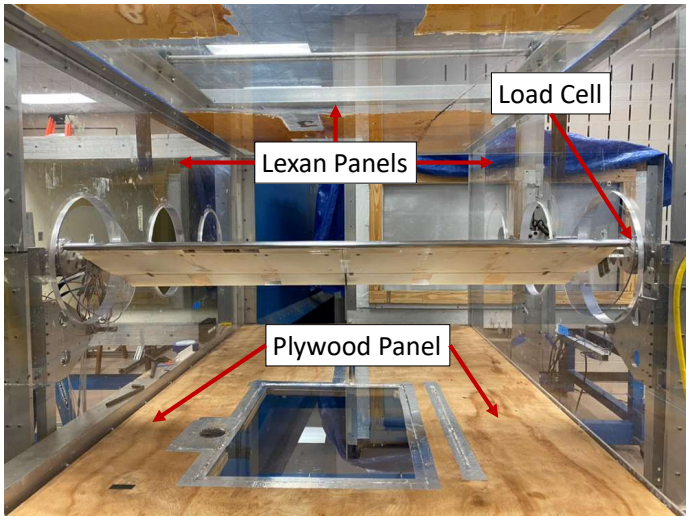

Figure 8.6: 1/16th scale HL-CRM wing in aerodynamic test section

The wind tunnel aerodynamic section was used to collect force and moment data (Fig. 8.6). Data was collected by load-cells installed at the both ends of the HL-CRM wing. Angle of attack was controlled with a rotational motor and recorded with a rotary encoder, attached to the starboard edge of the wing. Force and moment data were collected at various angles of attack and freestream velocities of 15 m/s and 25 m/s. These data were processed to produce coefficient of lift and coefficient of drag results.

8.2 Experimental Results

8.2.1 Aeroacoustic Results

Aeroacoustic testing was conducted to compare noise signatures between the untreated wing, the wing treated with the Stepped SGF, and the wing treated with the Conformal SGF. Utilizing the data collected from the microphone array, spectra plots of SPL and plots of OASPL were generated.

Fig. 8.7a displays the SPL spectral plot at 15 m/s for the three wing configurations (the untreated wing, the wing treated with the Stepped SGF, and the wing treated with the Conformal SGF) at 6° angle of attack. At 15 m/s, all three configurations emitted similar sound pressure levels from 0 kHz - 7.5 kHz. From 7.5 kHz - 20 kHz, the untreated wing emitted a higher noise level compared to the wing treated with either the Stepped or Conformal method, with the exceptions of peaks at 10 kHz and 15 kHz. The wing treated with either the Stepped SGF or the Conformal SGF was measured to emit similar noise levels over the observed frequency range.

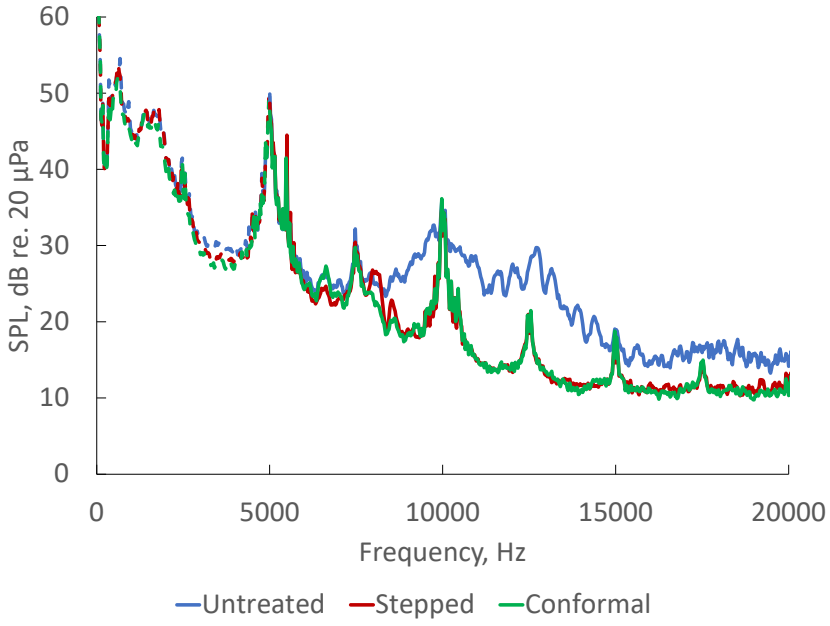

(a) Spectra SPL at 6° angle of attack

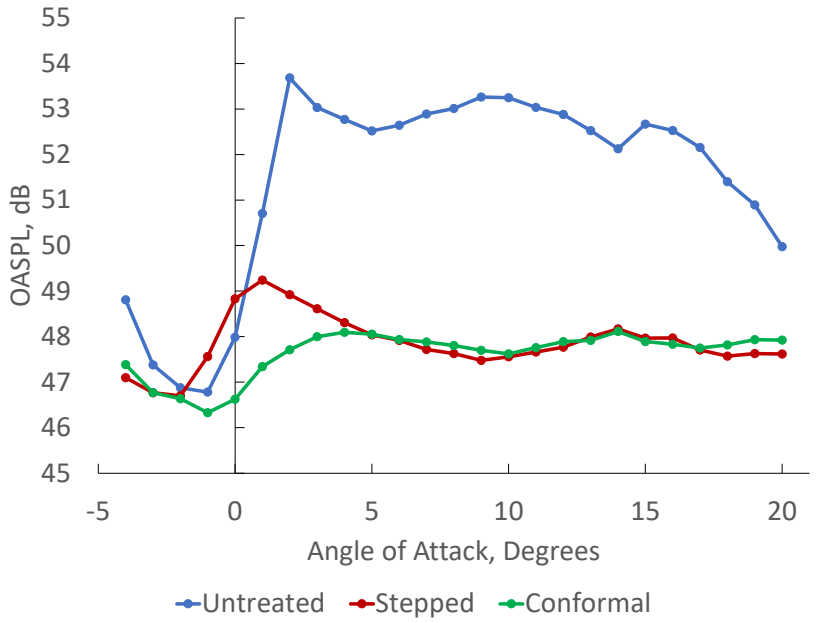

(b) OASPL at varying angles of attack from 6 kHz to 20 kHz

Figure 8.7: Acoustic data at various angles of attack in freestream velocity of 15 m/s

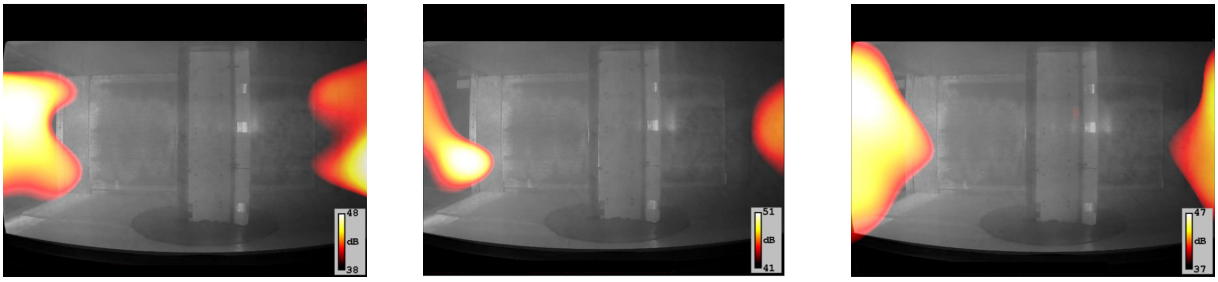

(a) Untreated wing (b) Stepped SGF Treatment (c) Conformal SGF Treatment

Figure 8.8: BeamFormX outputs showing background wind tunnel noise at 6° angle of attack in freestream velocity of 15 m/s at 5 kHz

The SPL peaks at 5 kHz were identified to be the Variable Frequency Drive (VFD) carrier frequency of the wind tunnel (Fig. 8.8). For clarity in making comparisons, data lower than 5 kHz is depicted with a dashed line. OASPL was calculated using the root sum square of SPL over a given frequency range. For these results, OASPL was processed using the frequencies of 6 kHz - 20 kHz to remove the effects of the wind tunnel. In doing so, the data better depicts the effects the SGF treatments have on the slat and omits wind tunnel noise interference.

To compare the noise emission of each wing configuration at various flight conditions, OASPL was plotted against angle of attack, as depicted in Fig. 8.7b. It was observed that both SGF treated wings emitted a lower OASPL compared to the untreated wing in the freestream velocity of 15 m/s. When the Stepped SGF was applied, the wing was observed to emit a higher OASPL than the untreated wing at angles of attack between -1° - 0°. The wing modified with the Stepped SGF emitted a lower OASPL than the untreated configuration, but higher than the wing modified with the Conformal SGF over angles of attack of 1° - 4°. The wing with the Conformal SGF applied emitted a lower OASPL than the untreated wing configuration for all tested angles of attack.

Noise sources for the untreated wing, the wing treated with the Stepped SGF, and the wing treated with the Conformal SGF are depicted in Fig. 8.9. With BeamformX, it was visually identified that a major source of noise at 12 kHz was the slat gap area of the wing. Treating the wing

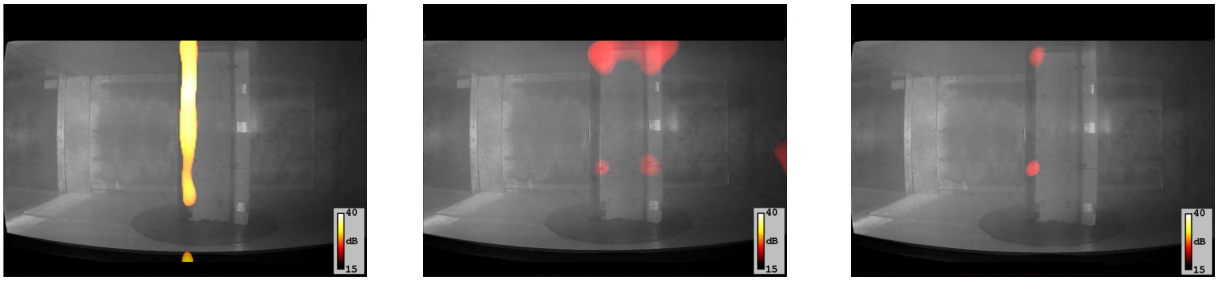

(a) Untreated wing (b) Stepped SGF treated wing (c) Conformal SGF treated wing

Figure 8.9: BeamFormX sound pressure outputs at 6° angle of attack in freestream velocity of 15 m/s at 12 kHz for the three tested wing configurations

with both the Stepped and the Conformal SGFs reduced noise emission compared to the untreated wing configuration.

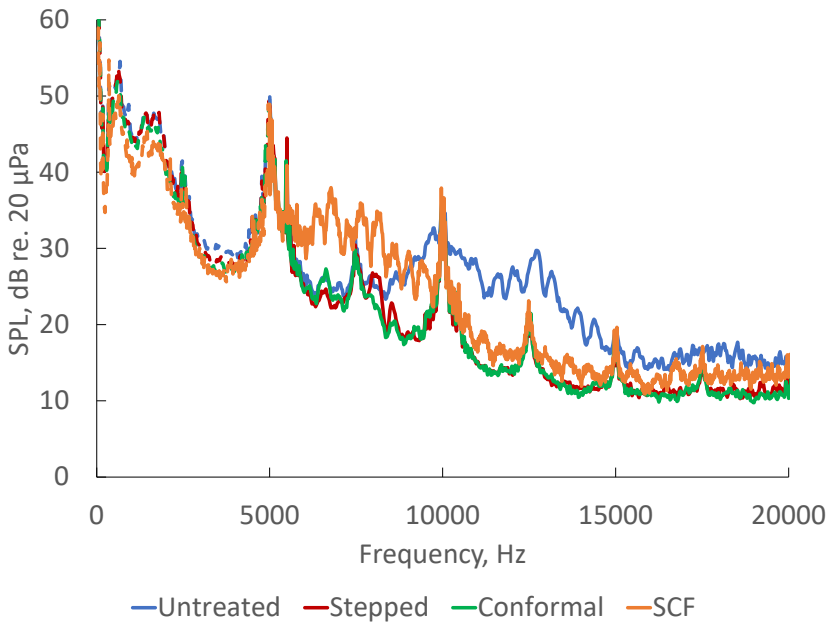

Figure 8.10: Comparison of SPL between the untreated wing, the Stepped SGF treated wing, the Conformal SGF treated wing, and the wing treated with the SCF [25]

Experimental methods similar to the slat-cove filler (SCF) study in [25] were followed in order to compare the SGF's effectiveness to the SCF. The SCF concept aimed to reduce noise by following flow streamlines and preventing circulation behind the leading-edge slat [6]. Sound pressure level (SPL) spectra results of the SCF from [8] were added to compare to the SPL from the SGFs tested herein, as shown in Fig. 8.10. The SGF treated wing appears to emit slightly lower SPLs than the SCF treated wing, especially at higher frequencies.

8.2.2 Aerodynamic Results

Data from load-cells attached to the wing in the aerodynamic test section was recorded and processed to calculate lift and drag coefficients (C_L and C_D, respectively) for various freestream velocities and angles of attack. Wing C_L and C_D is plotted against angle of attack in Fig. 8.11a, and C_L is plotted against C_D in Fig. 8.11b. It was noted that application of the Conformal SGF prevented the wing from reaching a negative angle of attack without oscillating violently. To protect the wing's structural integrity, wind tunnel tests were started at 2° for this SGF concept.

Referring to Fig. 8.11a, at angles of attack between 2° and 13°, the three wing configurations are comparable. From 13° to 20°, the SGF treated wings were observed to become unstable while exhibiting preliminary stall characteristics. Accordingly, the untreated wing configuration continues to show a positive slope at high angles of attack while both wings treated with a SGF begin to show decrease in slope. This decrease in slope is a result of the wing is beginning to stall, confirming the visual observations. The coefficient of drag for all concepts was comparable over the entire range of angles of attack.

Both figures suggest that stall angle was lower for the wing treated with the SGF concepts compared to the untreated wing. Closure of the gap between the trailing edge of the slat and the main wing is likely causing flow separation at a lower angle and an earlier onset of stall.

Referring to Fig. 8.11b, the three concepts performed similarly and generated a similar coefficient of drag at a given coefficient of lift over most of the drag polar. However, the wings treated with a SGF generated a lower maximum lift compared to the untreated wing. This lower maximum lift represents a decrease in treated wing performance as the wing begins to stall.

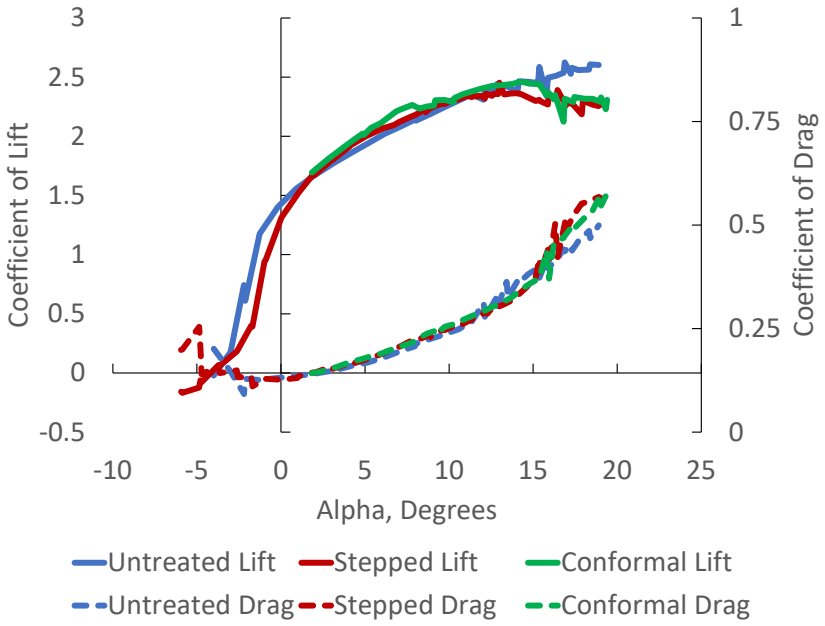

(a) Coefficient of lift and coefficient of drag at varying angles of attack

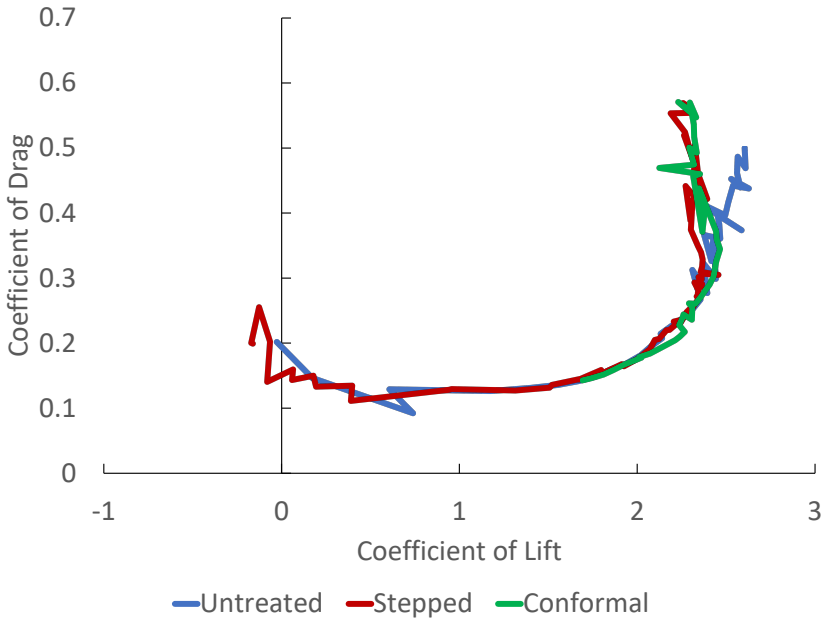

(b) Drag polar generated by varying angles of attack

Figure 8.11: Aerodynamic data of CRM wing in freestream velocity of 15 m/s

8.3 Discussion

Both SGF concepts generate reduced noise over a range of flight conditions at 15m/s freestream velocity. The Conformal SGF geometry may allow for smoother airflow over the wing at lower angles of attack, resulting in a quieter wing. More research should be conducted to identify what effects the geometric differences of the Stepped and Conformal SGF have on noise production. The promising aeroacoustic trends from both concepts also appeared in tests conducted at higher freestream velocities. However, the high lift devices appeared to warp under the increased load, so future model improvements are necessary to verify the aeroacoustic effects. Aerodynamically, the lift curve slope is similar for the Stepped SGF treated wing, the Conformal SGF treated wing, and the untreated wing between 2° and 13° angle of attack. However, application of both the Stepped and Conformal SGFs caused the wing to stall at a lower angle of attack compared to the untreated wing, highlighting the need for implementation in a flight vehicle to include provisions for opening the gap in emergency high angle of attack maneuvers. Similar to the aeroacoustic tests, in the aerodynamic tests the wing became too unstable at high angles of attack and high freestream velocities to make meaningful measurements. Therefore, further development of a more rigid wing system needs to be explored to test the concepts and configurations closer to realistic Reynolds numbers. Overall, the slat gap fillers tested decreased the overall sound emitted while minimally altering wing aerodynamic characteristics, making these concepts useful as baseline concepts.